We thank both reviewers for their comments and suggestions.

Reviewer #1

Zhang et al uses an analytical inverse method to estimate methane emissions from the GOSAT data from 2010 to 2018. The study contains a lot of information that is poorly structured and explained so I found it difficult to extract any new or notable scientific insights. I recommend a major revision that takes into the recommendations I have made below to help draw out the key points of the paper. Given the eminence of the coauthors I feel slightly aggrieved I have needed to make some of these points.

Thanks for your suggestions. We have worked through the manuscript to make the improvements.

Minor Comment

I think the language is a bit odd in places. Easily fixed but needs an overhaul.

We tried our best to improve the language throughout the text.

Major Clarifications

Cleanly separating wetland and non-wetland emissions, including rice paddies, etc is a bold claim. The authors' motivation, based on WetCHARTs, is that wetlands have relatively coherent spatial behaviours. From what I understand the authors' state vector is at grid-point resolution for non-wetland sources and their trend, but the wetland emissions are described on much larger spatial regions. I remain unclear whether using a combination of small and large geographical regions will decrease or increase posterior correlations between wetlands and anthropogenic emissions. An argument could be made for both sides. Certainly, more discussion/description is needed.

We now add a new figure (Figure 6), which shows the posterior error correlations between regional wetland and anthropogenic emissions. The error correlations are moderate (r: averages -0.3; range -0.1 to -0.5), suggesting that the inversion has some ability to separate the two at the regional scale.

We also test the impact of unresolved subregional wetland distribution on both wetland and anthropogenic estimates with an additional sensitivity inversion. We perturb prior wetland distribution in Africa following Lunt et al. (2019) (which reported that WetCHARTS underestimate over the Sudd region but overestimate over the Congo Basin). This results in some changes in estimates for both wetland and anthropogenic

emissions in the region, but the main conclusion still holds. The sensitivity inversion is presented in Figure S1 (prior wetland emission), Figure S4 (anthropogenic emissions), and Figure S5 (wetland emissions). The resulting impact on the inference of anthropogenic emissions in eastern Africa is also presented in Figure 8.

We also make changes in Section 2.2 (state vector) to better explain our reasoning on separate optimization of wetland and anthropogenic emissions.

These two statements are apparently contradictory: Line 155: "Our prior estimate assumes no 2010-2018 trends in non-wetland emissions. . .." Line 160: "We specify an absolute error standard deviations of 5%/a for linear trends of non-wetland emissions. . ."
They are not contradictory. The first statement describes the prior estimate for non-wetland trends, and the second describes the error statistics for this prior estimate. We now revise the two sentences to improve clarification.

Line 161: Given the diversity of emission estimates from the ensemble members of WetCHARTs and the resulting uncertainty covariance structure, I am left wondering how sensitive the authors' posterior solution is to this information.
We have tested the inversion without the error covariance structure (only diagonal terms) from the WetCHARTS ensemble. We find the resulting changes in the posterior solution are small. In addition, as described above, we perform a sensitivity inversion to test the impact of errors in subregional wetland distribution unresolved by our inversion.

Line 221: Given your reliance on the residual error method I think it would be useful to explain this a bit more.
We now explain the method in the text.

Line 224: Please clarify whether you use the brute force method to calculate the Jacobian matrix or take advantage of the tagged CH4 simulation, as described in section 2.4.
To construct the Jacobian matrix, we explicitly perturbed each individual element of the state vector in independent GEOS-Chem simulations and calculate the sensitivity of XCH_4 to that perturbation. We did not use any tagged simulation in this work. This is described Section 2.6.

Line 255: Comparison with NOAA is an important first step to determine whether your posterior solution is consistent with the observed atmospheric growth rate. Unfortunately, Figure 3 and the accompanying text is not sufficiently clear for this reviewer to make that judgement. For the lower right panel of Figure 3 it would be better to use a smaller y axis range given the small differences. At least then a reader can eyeball the comparison. I recommend "better fit" is substituted with some quantitative statistics, e.g. bias, correlations, etc.

We now add the panel with smaller y axis in the Figure S6. We still keep the original panel in the main text (which has the same y axis as the left panel), as it is easy for a reader to compare prior and posterior simulations. We now report root-mean-square errors to quantitatively describe the fit to observations.

Comment on arrangement of paper: showing your ability to independently estimate wetland and non-wetland emissions on the spatial scale you are using (Figure 14) would be useful up front before the more detailed discussions begin. See my comments below.

We now add more discussion on the posterior error correlation before we start presenting inversion results in Section 3 (previously Section 2.7). We have moved previous Figure 14 (Now Figure 5) and relevant discussion to this section. As mentioned in above responses, we also add a new figure (Figure 6) with more detailed discussion on error correlations between wetland and anthropogenic emissions at a regional scale.

A broad comment relevant to more than one figure, e.g. Figure 3: the period 2010 to 2018 covers a wide range of climate variations (e.g. both phases of ENSO) so that taking the mean or differences over this period hides a lot of useful information about how methane has changed.

The bottom panels of Figure 3 already show the monthly time series for the period. The posterior errors (Fig. 3d) are stable throughout the period with reduced seasonal error compared to the prior results. In particular, they show no coherence with ENSO phases. We now modify the relevant text to improve clarity. We also add Fig. S3 in the Supplementary Material, which shows the time series of errors compared to independent ground-based observations. Fig. S3 also shows that the posterior errors have no coherence with ENSO phases.

Line 289: averaging kernel sensitivities? The matrix of averaging kernels already describes sensitivity. Do the authors mean the sensitivities described by this matrix?

We introduced averaging kernel sensitivities (in Section 4.1) as diagonal terms of the averaging kernel matrix corresponding to a specific state vector element, which represent the sensitivity of a state vector element to its true value. The spatial/temporal distribution of this quantity visualizes locations where/when the inversion has strong/weak observational constraints. To better introduce this concept, we now formally define averaging kernel sensitivities in Method section (Section 2.6). We also add more explanations to the captions of relevant figures.

Line 292: from what I understand the state vector has a length of 1000s but the DOFs is limited to 179. What implications does that have for being able to resolve the state vector?

We now add more relevant discussion following the statement. Basically, this indicates that the inversion cannot fully resolve the 1009 state vector element. The constraints from the observations vary spatially, as shown in the figure of averaging kernel sensitivities (Fig. 7 right) mentioned above.

Line 291: "By applying the posterior/prior correction factors to the prior distribution of each anthropogenic emission sector, we obtain improved estimates for anthropogenic emissions for that sector." This statement does not make sense. Improved how? Better fit to measurements? Smaller uncertainties? Applying correction factors does not improve estimates for anthropogenic emissions. Which sector?

The sentence is removed.

Comments on reporting results: some posterior estimates are accompanied by their uncertainties and some are not. The authors need to be consistent. They should certainly report them on Figure 6.

We now report throughout the text the errors derived from posterior error covariance matrix. The error bar is not plotted in Figure 6 and Figure 7 (left panel) because they are often too small compared to the absolute magnitude. We now note this in the figure captions.

Line 315: I am really interested to hear more about how their results point towards an underestimate in livestock emissions. This whole paragraph contains so much hand waving I thought I was at a pre-pandemic music festival. I urge the authors to justify their result in light of it being inconsistent with Maasakkers et al and other published studies that attribute most of these changes to wetlands. I acknowledge they take a second swing at this point on page 15 but I was unsure which they used for their prior (for Figure 8) and more importantly how confidently they could separate wetland and livestock emissions.

Both paragraphs are rewritten to better present the results.

We first would like to clarify that the first paragraph is for mean anthropogenic emissions, and the second paragraph is for emission trends. So, they are separate discussions and are placed in different sections of the paper. We now make changes in both paragraphs to increase clarity.

Our results are consistent with Maasakkers et al. in that both inversions found prior emissions underestimate over these regions. We differ, however, in the attribution. Maasakkers et al. mainly attributed the underestimation to wetland, based on fractions of each sector in prior information. Maasakkers et al. did not exploit the significant seasonal and spatial structure of wetland emissions, which our approach makes use of to separate wetland and non-wetland emissions (with different spatial and temporal resolution). We now add discussion about the error correlations between anthropogenic and wetland emissions (Figure 6). We also present the results of the sensitivity inversion mentioned above, which shows the results presented are robust against the perturbation.

Fig. 10 (previously Fig. 8) discusses the regional emission trends attributed to the livestock sector. We use trends in these inventories to support that increasing livestock emissions over these regions are also plausible from the bottom-up perspective. They are not prior information in our inversion, as we assumed zero prior emission trends in the inversion (described in Section 2.3 and repeated also in the figure's caption). We have modified the text for Fig. 8 to remove any ambiguity.

Line 358: why are the constraints strongest over India and China?

The averaging kernel sensitivities are a function of multiple factors including

observation number, transport, and emissions, and are often large over regions with large emissions. This constraint stems mainly from the fact that these strong emissions, if exist, can create large methane gradients, that are easy to detect by satellite observations. We now briefly explain it in the text.

Line 539: That's a very long lifetime for methane against OH oxidation. This reviewer is left wondering whether the authors' inverse problem remains ill-posed given their state vector. The joint PDF clearly shows strong correlations between different parts of the (global mean) state vector. Given the authors reporting of regional methane missions, it would be useful to show the regional joint PDFs for which I suspect the correlations between anthropogenic and wetland emissions can be much higher. Their conclusion on page 24 doesn't fill me with confidence.

The lifetime we derived is within but at the high end of that derived from the methylchloroform proxy. We now also add text here to remind the readers of the strong error aliasing between global OH and global wetland emissions in this inversion (Figure 5).

As mentioned above, we add Fig. 6 which show that the error correlations between anthropogenic and wetland emissions are moderate at regional level (r: averages -0.3; range -0.1 to -0.5).

Reviewer #2

This article analyses the role of wetland and livestock on the global CH4 growth rates in the period 2010-2018. The authors have also carefully assesed the role of OH on the CH4 growth rate. The article is generally well written, and has built upon their earlier analysis. I have doubt on the simplicity of the emission optimisation for only two major sectors, while CH4 has so many other natural and anthropogenic emission sectors those vary very differently at interannual and longer timescales. Detailed comments below. The manuscript may be considered for publication after addressing some of these comments.

Specific comments: lines 38-39 : need references?

A reference is added.

lines 76ff: I find later that the CTM configuration and other details are discussed later. May be remove this paragraph

We remove the paragraph.

lines 90ff: I think this is not an ideal choice because the values of CH_4 depends on assumed CO_2 concentrations. We know that our understanding of CO_2 fluxes over many data void regions are poor. How do you estimate regional bias, say over South Asia, Southeast Asia, Amazon/Brazil, Africa etc.

The CO_2 proxy retrieval has been systematically evaluated against ground-based measurements with its uncertainty characterized (Parker et al., 2020) and has been extensively used in other methane inversion studies. In particular, validation has also been performed for the uncertainties induced by the model XCO2 (Parker et al., 2015). An evaluation was also performed over Amazon against aircraft profile observations (Webb et al., 2016). We now add information about these validation studies in the manuscript.

line: that's the lower bound, what about the oceans?

We do not know what this comment is referred to.

line 137: Did you apply any scaling to termite emissions?

We did not apply any scaling to Fung et al. (1991) in the prior emissions. We do optimize termite emissions together with other non-wetland emissions. We now report the total termite emissions in the text in case readers are interested in the magnitude.

lines 170ff: 1-year spin-up is too short by any standards for long-lived species. What about the stabilisation of vertical gradients? You cannot get that right by the unbiasing method you describe. For future studies please make a spin-up for 10 years or so. Its worth the computing cost, given the large amount of follow work and analysis is done for any publication.

The previous description was inaccurate. The 1-year spin-up simulation was initialized from a CH_4 field generated from a long-term simulation (Turner et al., 2015), in which stabilization of global-scale methane gradients is already achieved. The additional 1-year simulation using 2009 meteorology was to establish reasonable synoptic-scale

gradient on the starting date (Jan 1 2010). We now modify our description to avoid this confusion.

Figure 2 and associated text: Does these correction factors extend till the poles? The problem is that the stratosphere is dynamic as well. Are such seasonal bias correction factor good for getting the profiles right.

We fully agree with you that the stratosphere is dynamic. We do find that the correction factors are better predicted by equivalent latitude rather than ordinary latitude. Equivalent latitude is a function of potential vorticity, which partly reflects the dynamics of stratosphere, in particular polar vortex. We now emphasize this point in the text. It is not necessary to extend the correction to the poles, because we do not have any GOSAT data over very high latitudes to begin with.

My worry here is also that if the stratosphere is not spun-up well these bias correction factors will not be time invariant. So the trends in anthropogenic or natural emissions you derive later may not be free of these correction factors.

See above responses on initial conditions for "not well spun-up stratosphere". In addition, we now also compute the correction factors by individual years, and find no significant shift in the correction factors (Figure S2).

Figure 5 and associated text: Very tough to accept the results for the a posteriori patterns, e.g., there is a strip of increased emissions along the Himalayan region! Is this arising from not properly accounting for the orography in the coarse resolution model? Or this may be an artifact of the proxy retrievals by miscalulating CO_2 over northern part of the Indian subcontinent.

The absolute changes along the Himalayan region are very small (because prior emissions there are very small). We now add Figure S7, which shows the absolute changes between prior and posterior estimates to help readers interpret the results. We still retain the posterior/prior ratio plot, as the ratios are useful for interpreting results for regions with large emissions.

Figure 6 and associated text: I like this analysis but it is not clear at all, if the results are independent of the priors! For example, if you if you started with the priors from the UNFCCC will you get the same a posteriori emissions? The question is also same for

the trends in derived emissions. Some sensitivity tests are need for clarifying robustness of the a posteriori emissions. See for example Patra et al., JMSJ, 2016. That paper is also relevant for other discussion in the paper where you discuss trends of emissions over China, and from Animals etc.

We now report the reduced averaging kernel sensitivities in the figure, which characterizes the dependence of the results on observations vs. prior. We now also cite Patra et al., 2016 and include it for discussion where relevant.

lines 340-344: How confidently we can talk about the oil and gas emission trends - given that the cited references are so small scale compared to the gridcell you optimize here. For example, can you gather the cited references by model gridcells and check the validity of the inversion and vice versa?

Though in coarse resolution, the upward correction patterns over Mid- and South U.S. in Fig. 7 correspond to major U.S. oil and gas production regions, where underestimation of emissions is reported by work of these cited references repeatedly. We now add a discussion on Maasakkers et al. (2020) who performed a high-resolution inverse analysis over the U.S. using the 2010-2015 GOSAT data, and allocated the correction more specifically to these oil/gas regions.

lines 366-377: I am a bit confused why/how all the anthropogenic emissions are linked with the livestock population? Is this because your a priori emissions only accounts for the livestocks? For example how is the trends in waste management in these developing nations?

We now modify the text to avoid any confusion that the attribution is made based on livestock population. We attribute these trends to emission sectors based on their fractions in prior information over a grid cell. We then support this attribution with bottom-up information (both livestock population data and bottom-up livestock inventories).

Page 18-20: I do not know but I have a feeling that the inversion is set in such a way that all the regions are having somewhat similar increase in emissions, either from the animals or from wetlands. The authors are in the best position to judge and find the reasons behind such outcomes from their inversion system.

Fig. 9 shows the spatial patterns of anthropogenic emission trends derived from our

inversion. Fig. 12 shows the trends of wetland emissions in 14 subcontinental regions. Both show that varied magnitudes of trends are inferred for different regions by our inversion.

If you can explain the global CH4 growth rates using emissions from only two emission sectors then we have an oversimplifications of CH4 sources. I cannot prove anything in favour or against the proposed mechanisms here but many of the hypothesis are based on apparently single line of evidence, i.e., the GOSAT proxy XCH4 retrievals. Aren't Maasakkers et al., Lunt et al., Pandey et al., Parker et al. using the same XCH4 data sources?

We did not intend to state that wetland and livestock are the only two sectors contributing to accelerating methane growth. We now make several changes in the text to avoid this misimpression. In particular, when discussing wetland contributions, we are now more explicit about the years (2016-2018) that we infer large wetland emissions, rather than presenting them as a trend (which is misleading because they are just large inter-annual variability occurring in the latter part of the study period). We also discussed contributions from other sectors (Fig. 13 and relevant text).

Indeed, evidence are mostly from GOSAT XCH4 data for now, because of the lack of other measurements in these remote regions. Our findings suggest that more attention should be paid to these regions.

In addition to the trends analysis, it would have been useful to discuss how and why are the large interannual variability in some regions as shown in Fig. 10. Are there irregular data gaps or a particular climate anomaly affecting CH4 emissions regionally?

Thanks for the suggestions. We have a paper in preparation that uses the satellite-constrained wetland emissions to examine the drivers of their variability in different regions.

line 470: The NH/SH OH ratio of 1.02 is an interesting result from this exercise. Could you please comment here how are the NH/SH ratio of CH4 emission changed from a priori to a posteriori cases? I suspect the derived NH/SH OH ratio depends on how well freely the inversion system is allowed to adjust emissions vs that for OH.

Our setup is based on the reasoning that emissions can be informed by

regional/subcontinental gradients of CH_4 while OH mainly is informed by global/hemispheric gradients of CH_4. With this setting, both emissions and OH have some freedom to adjust. The figure below shows the NH/SH ratio of emissions in prior and posterior estimates, which demonstrates that hemispheric emission ratios are indeed being adjusted by the inversion (though emissions are resolved at much finer resolution). We decide not to include the figure in the manuscript to better focus on the OH ratio results.

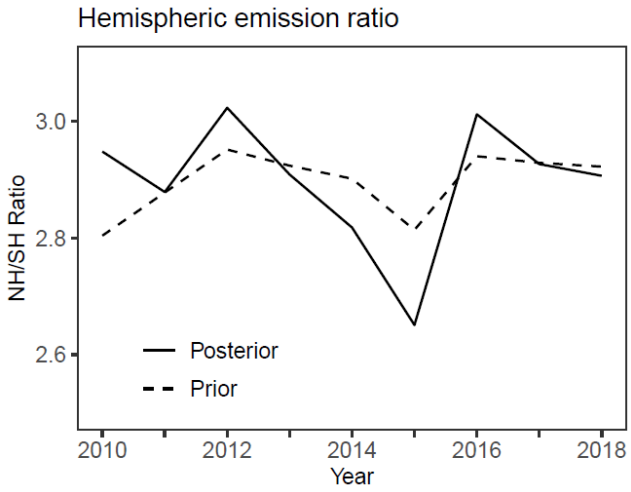

page 23: How can we get assured that the OH and CH4 emissions can be optimised in one inversion system. Is there a dipole effect? For example, if you do more or less number of iterations, will the global total emission and global mean OH will be different? I see that this issue is addressed later using Fig. 14, but still not convinced that the inversion system is separating the wetland vs livestock emissions well.

We solve the inversion analytically. So, we do not iterate to find the solution. In our previous work (Zhang et al., 2018), we tested separate optimization of OH and CH4 emissions in an Observation System Simulation Experiment, which demonstrated some ability to separate changes in OH and CH4 emissions in an inversion similar to the setting here. Zhang et al. (2018) identified that the major source of uncertainty to the method is the prescribed distribution of spatial-temporal OH fields (about 3% systematic uncertainty). We now add text to remind readers that with current observations we have only limited ability to separate OH and emissions.

As described in the above responses, we now add more discussion to support the separability of wetland and anthropogenic emissions on regional scales. Briefly, we add

a new figure (Figure 6) to show the posterior error correlations between regional wetland and anthropogenic emissions. We also perform a sensitivity inversion to test the impact of unresolved subregional wetland distribution on posterior wetland and anthropogenic estimates. In this sensitivity simulation, prior wetland distribution in Sudd and the Congo Basin of Africa (which are near livestock hotspots) is perturbed (Figure S1). Results are shown in Figure S4, Figure 8 (anthropogenic emissions), and Figure S5 (wetland emissions).

Figure 13: You attributed emissions from livestock increase to the animal population, but what appears here is that the increase in emissions from tropical and extratropical wetland are the greatest. Could you propose a mechanistic viewpoint?

We have briefly included some discussion on the driver based on literature. As mentioned above, we will explore from this perspective in a paper in preparation.

Attribution of the accelerating increase in atmospheric methane during 2010–2018 by inverse analysis of GOSAT observations

Yuzhong Zhang[1,2,3], Daniel J. Jacob[3], Xiao Lu[3], Joannes D. Maasakkers[4], Tia R. Scarpelli[3], Jian-Xiong Sheng[5], Lu Shen[3], Zhen Qu[3], Melissa P. Sulprizio[3], Jinfeng Chang[6], A. Anthony Bloom[7], Shuang Ma[7], John Worden[7], Robert J. Parker[8,9], Hartmut Boesch[8,9]

[1]~~School~~[1]Key Laboratory of Coastal Environment and Resources Research of Zhejiang Province, School of Engineering, Westlake University, Hangzhou, Zhejiang, China
[2]Institute of Advanced Technology, Westlake Institute for Advanced Study, Hangzhou, Zhejiang, China
[3]School of Engineering and Applied Science, Harvard University, MA, USA
[4]SRON Netherlands Institute for Space Research, Utrecht, the Netherlands~~.~~
[5]Center for Global Change Science, Massachusetts Institute of Technology, Cambridge, MA, USA
[6]Zhejiang University, Hangzhou, Zhejiang, China
[7]Jet Propulsion Laboratory, California Institute of Technology, Pasadena, CA, USA
[8]National Centre for Earth Observation, University of Leicester, UK
[9]Earth Observation Science, School of Physics and Astronomy, University of Leicester, UK

Correspondence to: Yuzhong Zhang (zhangyuzhong@westlake.edu.cn)

Abstract. We conduct a global inverse analysis of 2010–2018 GOSAT satellite observations to better understand the factors controlling atmospheric methane and its accelerating increase over the 2010–2018 period. The inversion optimizes ~~2010–2018~~ anthropogenic methane emissions and their 2010–2018 trends on a 4°×5° grid, monthly regional wetland emissions, and annual hemispheric concentrations of tropospheric OH (the main sink of methane~~) also for individual years.~~). We use an analytical solution to the Bayesian optimization problem that provides closed-form estimates of error covariances and information content for the solution. ~~Our~~We verify our inversion ~~successfully reduces the errors against the~~results with independent methane observations from the TCCON ~~network and~~and NOAA networks. Our inversion successfully reproduces the interannual variability of the methane growth rate inferred from NOAA background sites. We find that prior estimates of fuel-related emissions reported by individual countries to the United Nations are too high for China (coal) and Russia (oil/gas), and too low for Venezuela (oil/gas) and the U.S. (oil/gas). We show ~~that the~~large 2010–2018 ~~increase~~increases in ~~global~~ anthropogenic methane emissions ~~is mainly driven by tropical wetlands (Amazon and tropical Africa), boreal wetlands (Eurasia), and tropical livestock (~~over South Asia, tropical Africa, and Brazil~~),~~, coincident with ~~no significant trend in oil/gas emissions. While the rise in tropical livestock emissions is consistent with bottom-up estimates of~~ rapidly growing ~~cattle~~livestock populations~~, the rise in wetland emissions needs to be better understood. The sustained acceleration of growth rates in 2016–2018 relative to 2010–2013 is mostly from wetlands, while the~~ in these regions. We do not find a significant trend in anthropogenic emissions over regions with large production or use of fossil methane, including the U.S., Russia, and Europe. Our results indicate that the peak methane growth rates in 2014–2015 are ~~also contributed~~driven by low OH

concentrations (2014) and high fire emissions (2015~~),~~), while strong emissions from tropical (Amazon and tropical Africa) and boreal (Eurasia) wetlands combined with increasing anthropogenic emissions drive high growth rates in 2016–2018. Our best estimate is that OH did not contribute significantly to the 2010–2018 methane trend other than the 2014 spike, though error correlation with global anthropogenic emissions limits confidence in this result.

1 Introduction

Methane is the second most important anthropogenic greenhouse gas after CO_2, with an emission-based radiative forcing of 0.97 W m^{-2} since pre-industrial times (Myhre et al., 2013). Methane is emitted to the atmosphere from a range of anthropogenic activities including fuel exploitation, agriculture, waste and wastewater treatment, and biomass burning. The main natural source is from wetlands, with minor contributions from geological seeps, forest fires, and termites. Atmospheric methane has a lifetime of 11.2 ±1.3 years against tropospheric oxidation by the hydroxyl radical (OH) (Prather et al., 2012). Minor sinks include stratospheric loss, oxidation by Cl atoms, and absorption by soils~~.~~ (Kirschke et al., 2013).

Unlike the steady rise in atmospheric CO_2, the rise of methane has taken place in fits and starts. Observations from the NOAA network (Dlugokencky, 2020) (https://www.esrl.noaa.gov/gmd/ccgg/trends_ch4/, last access: 22 June 2020) show a period of stabilization in the early 2000s, followed by a renewed growth after 2007 that has accelerated since 2014. Annual growth rates averaged 0.50% a^{-1} for 2014–2018, compared to 0.32% a^{-1} for 2007–2013. The growth of atmospheric methane concentrations, if continued at current rates in coming decades, may significantly negate the climate benefit of CO_2 emission reduction (Nisbet et al., 2019).

However, our understanding of the drivers behind the methane growth rate is still limited, preventing reliable projections for future changes. Explanations have differed for the renewed growth of atmospheric methane since 2007. A concurrent increase in atmospheric ethane has been interpreted as evidence of an increase in oil and gas emissions (Hausmann et al., 2016;Franco et al., 2016). However, the assumption that the ethane/methane emission ratio should be stable is questionable (Lan et al., 2019). Meanwhile, a concurrent shift towards isotopically lighter methane has been attributed to an increase in microbial sources either from livestock or wetlands (Schaefer et al., 2016;Nisbet et al., 2016). Worden et al. (2017) pointed out that the trend towards isotopically lighter methane could be explained by decreases in fire emissions that are isotopically heavy. Based on methyl chloroform observations, Turner et al. (2017) and Rigby et al. (2017) suggested that a decrease in the OH sink may be the cause of the methane regrowth.

To better interpret the methane budget and its recent trends, we present here an inverse analysis of global 2010–2018 methane observations from the GOSAT satellite instrument. GOSAT provides a long record (starting in 2009) of global high-quality observations of column methane mixing ratios (Kuze et al., 2016;Buchwitz et al., 2015). A number of inverse analyses

previously used GOSAT observations to constrain methane emission estimates (Fraser et al., 2013;Monteil et al., 2013;Cressot et al., 2014;Alexe et al., 2015;Turner et al., 2015;Pandey et al., 2016;Pandey et al., 2017a;Miller et al., 2019;F. Wang et al., 2019a;Lunt et al., 2019;Maasakkers et al., 2019;Janardanan et al., 2020;Tunnicliffe et al., 2020;Yin et al., 2020). Maasakkers et al. (2019) used 2010–2015 GOSAT observations to optimize gridded methane emissions, global OH concentrations, and their 2010–2015 trends. They concluded that increasing methane emissions were driven mainly by India, China, and tropical wetlands. Our analysis is based on that of Maasakkers et al. (2019) but extends it to 2018 in order to interpret the post-2014 acceleration. ~~It implements~~We implement for that purpose a number of major improvements to the Maasakkers et al. (2019) methodology including in particular (1) separate optimization of subcontinental wetland emissions to resolve their seasonal and interannual variability; (2) correction of stratospheric methane forward model biases based on ACE-FTS solar occultation satellite data (Waymark et al., 2014); (3) prior estimates of global fuel exploitation emissions using national reports submitted to the United Nations Framework Convention on Climate Change (UNFCCC) (Scarpelli et al., 2020), and (4) optimization of annual hemispheric OH concentrations.

2 Methods

~~We perform a global inversion to optimize the sources and sinks of atmospheric methane, and their 2010–2018 trends, by drawing information from GOSAT data and prior knowledge following the Bayes' rule.~~

~~We assemble the 2010–2018 GOSAT methane column observations in an observation vector $\boldsymbol{y}$ (Section 2.1), and optimize a state vector $\boldsymbol{x}$ including methane sources and sinks and their trends (Section 2.2). Prior estimates $\boldsymbol{x}_a$, which regularize the Bayesian solution, are compiled from bottom-up estimates for specific methane sources and sinks (Section 2.3). We use the GEOS-Chem chemical transport model (CTM) version 11.02 as the forward model to relate atmospheric methane to its sources and sinks (Section 2.4), and correct model biases in the stratosphere using independent satellite observations from the ACE-FTS instrument (Section 2.5). We solve the Bayesian optimization problem analytically to obtain both the posterior solution $\hat{\boldsymbol{x}}$ and its error covariance matrix $\hat{\boldsymbol{S}}$, thus achieving a closed-form quantification of information content as part of the solution (Section 2.6). The inversion is evaluated by measuring its fit to observations (Section 2.7), lending confidence in the results before we analyze them in Section 3.~~

2.1 GOSAT observations

The observation vector for the inversion ($\boldsymbol{y}$) consists of column averaged dry-air methane mole fractions during 2010–2018 observed by the TANSO-FTS instrument on board the Greenhouse Gases Observing Satellite (GOSAT) (Kuze et al., 2009). The satellite is in polar sun-synchronous low-Earth orbit and observes methane by nadir solar backscatter in the 1.65 μm shortwave infrared absorption band. Observations are made at around 13:00 local solar time. We use the University of Leicester

version 9 CO_2 proxy retrieval (Parker et al., 2020a). ~~The~~The retrieval has been extensively validated against ground-based column observations from the Total Carbon Column Observing Network (Wunch et al., 2011). Validation has also been performed for the model XCO_2 used in the CO_2 proxy retrieval (Parker et al., 2015), and for a specific region (i.e., Amazon) against aircraft profile observations (Webb et al., 2016). Overall, the retrieval has a single-observation precision of 13.7 ppb and a regional bias of 4 ppbv (Parker et al., 2020a), sufficient for a successful methane inversion (Buchwitz et al., 2015). The inversion ingests a total of 1.5 million successful GOSAT retrievals. Previous inversions of GOSAT data often excluded high-latitude ~~GOSAT~~ observations because of seasonal bias, large retrieval errors at low solar elevations, and ~~uncertainty in the role of~~forward model errors for the stratosphere (Bergamaschi et al., 2013; Turner et al., 2015;Z. Wang et al., 2017;Maasakkers et al., 2019). The exclusion of high-latitude observations limited the capability of the inversions to resolve emissions at high latitudes such as from boreal wetlands and oil/gas ~~emissions~~activity in Russia (Maasakkers et al., 2019). Here we use an improved model bias correction scheme (Section 2.5) and include these high-latitude observations in the inversion.

2.2 State vector

The state vector ($\boldsymbol{x}$) is the ensemble of variables that we seek to optimize in the inversion. In this work, the state vector includes (1) mean 2010–2018 methane emissions from non-wetland sources (all anthropogenic and natural emissions excluding wetlands) on a global 4º×5º grid (1009 elements); (2) linear trends of non-wetland emissions on that same grid (1009 elements); (3) ~~monthly~~ wetland emissions from 14 subcontinental regions for individual months (1512 elements) (Figure 1); and (4) annual-mean tropospheric OH concentrations in the northern and southern hemispheres (18 elements). The reason to treat wetland and non-wetland emissions separately is that wetland emissions have large seasonal and interannual uncertainties ~~but relatively coherent spatial behaviors (Bloom et al., 2017). Therefore, we can use the inversion to characterize seasonal and interannual variability in wetland emissions, instead of imposing them as part of the prior estimate as was done by Maasakkers et al. (2019). The latter approach introduced substantial seasonal biases in the forward model simulation that then had to be empirically filtered out before conducting the inversion (Maasakkers et al., 2019).~~(as compared to anthropogenic emissions); coarsening the spatial resolution when optimizing wetland emissions allows us to estimate monthly values for individual years (Bloom et al., 2017). This is a significant improvement over the inverse analysis of Maasakkers et al. (2019), where interannual and seasonal errors in prior wetland emissions were not addressed by the inversion.

Another improvement in the state vector definition relative to Maasakkers et al. (2019) is to optimize annual mean OH concentrations in each hemisphere rather than just globally. Y. Zhang et al. (2018) previously found with an observing system simulation experiment that it should be possible to constrain annual mean hemispheric OH concentrations from satellite methane observations. Patra et al. (2014) suggested that global CTMs are often biased in their interhemispheric OH gradient relative to methyl chloroform observations, and such bias, if not corrected, would propagate to the solution for methane emissions.

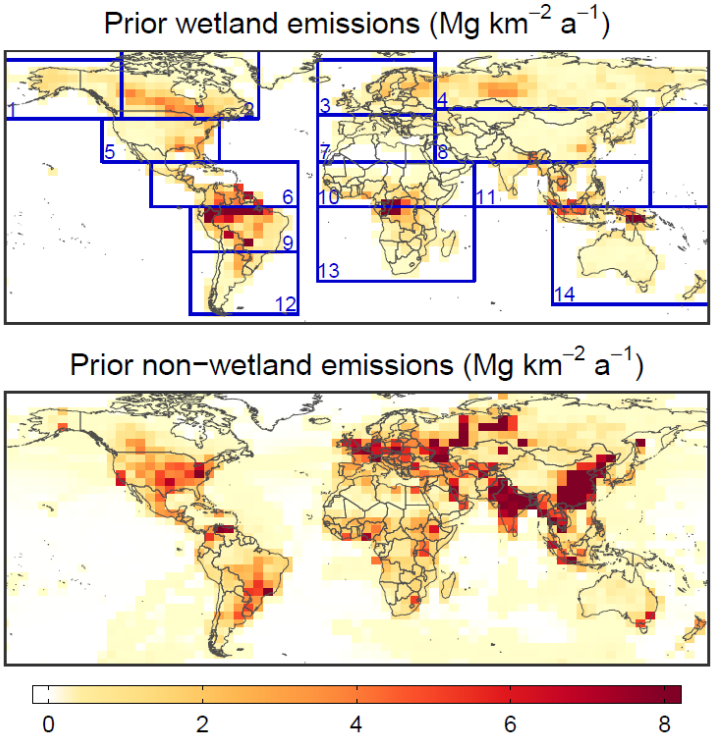

Figure 1. Spatial distribution of mean 2010–2018 methane emissions used as prior estimates in the inversion of GOSAT data. Top panel shows wetland emissions, and bottom panel shows non-wetland emissions. Blue boxes indicate the 14 subcontinental regions for which ~~monthly~~ wetland emissions are optimized for individual months (Section 2.2): (1) Alaska+West Canada, (2) East Canada, (3) ~~West~~Northern Europe, (4) ~~Russia~~Siberia, (5) ~~USA~~Temperate North America, (6) Latin America, (7) ~~North Africa~~Mediterranean, (8) East Asia, (9) Amazon, (10) Sub-Sahara Africa, (11) Tropical South Asia, (12) Argentina, (13) Southern Africa, and (14) Indonesia+Australia.

2.3 Prior estimates

Prior estimates for methane sources and sinks ($\boldsymbol{x}_a$) are compiled from an ensemble of bottom-up studies. Figure 1 shows the spatial distribution of prior emission estimates. For gridded 4º×5 º anthropogenic emissions, we use as default the EDGAR v4.3.2 global emission inventory for 2012 (https://edgar.jrc.ec.europa.eu/, last access: 1 December 2017) (Janssens-Maenhout et al., 2017). We supersede it for the ~~US~~U.S. with the gridded version of the Environmental Protection Agency greenhouse gas emission inventory for 2012 (Maasakkers et al., 2016). We further supersede it globally for fuel (oil, gas, and coal) exploitation with the inventory of Scarpelli et al. (2020) for 2012, which disaggregates spatially the national emissions reported to the United Nations Framework Convention on Climate Change (UNFCCC) (di.unfccc.int). All anthropogenic emissions are assumed to be aseasonal, except manure management for which we apply local temperature-dependent corrections (Maasakkers et al., 2016), and rice cultivation for which we apply gridded seasonal scaling factors from B. Zhang et al. (2016).

~~Monthly~~

For the prior estimates of natural emissions, we take monthly wetland emissions ~~from~~during 2010~~ to~~ –2018~~ are~~ from the WetCHARTS v1.0 extended ensemble mean (Bloom et al., 2017~~).~~) for each subcontinental domain of Figure 1. To test the impact of wetland spatial distribution within the subcontinental domains on inversion results, we performed a sensitivity inversion in which prior WetCHARTS emissions in Africa (regions 10 and 13 in Figure 1) are increased by a factor of 3 in the Sudd wetland of South Sudan and decreased by a factors 2.5 in the Congo Basin, following Lunt et al. (2019) and as shown in Figure S1. Daily global emissions from open fires are taken from GFEDv4s (van der Werf et al., 2017), which accounts for high methane emissions from peatland fires (Liu et al., 2020). For geological sources, we scale the spatial distribution from Etiope et al. (2019) to a global total of 2 Tg a^{-1} inferred from preindustrial-era ice core $^{14}CH_4$ data (Hmiel et al., 2020). Termite emissions are from Fung et al. (1991~~).~~) totalling 12 Tg a^{-1}.

The prior estimates for 2010–2018 trends in non-wetland emissions are specified as zero on the 4°×5 ° grid, except for interannual variability in fire emissions given by GFEDv4s. In this manner, all information on the posterior estimate of anthropogenic emission trends is from the GOSAT observations.

The prior estimates for the hemispheric tropospheric OH concentrations are based on a GEOS-Chem full chemistry simulation (Wecht et al., 2014). The monthly 3-D OH concentration fields from this full chemistry simulation are also used in the forward model. We optimize hemispheric OH concentrations as the methane loss frequency [s^{-1}] due to oxidation by tropospheric OH (k^i) in the northern and southern hemispheres (i = north or south):

$$k^i = \frac{\int_{\text{troposphere},i} k'(T)[\text{OH}]n_{CH_4}\,dv}{\int_{\text{atmosphere}} n_{CH_4}\,dv} \quad (1)$$

where n_{CH_4} is methane number density [molecules cm^{-3}~~],~~, v is volume, and $k'(T)$=2.45×10^{-12} $e^{-1775/T}$ cm^3 $molec^{-1}$ s^{-1} is the temperature-dependent oxidation rate constant (Burkholder et al., 2015). In this definition, the denominator of Eq. 1 integrates over the entire atmosphere and the numerator integrates over the hemispheric troposphere. Hence, global methane loss frequency (or inverse lifetime; k) due to oxidation by tropospheric OH can be expressed as the sum of hemispheric values ($k = 1/\tau = k^{\text{north}} + k^{\text{south}}$ where τ is the global lifetime due to oxidation by tropospheric OH). Our prior estimates from Wecht et al. (2014) are 0.050 a^{-1} for k^{north} and 0.043 a^{-1} for k^{south}, which translates to a τ of 10.7 years and a north to south inter-hemispheric OH ratio of 1.16. In comparison, the methyl chloroform proxy infers τ of 11.2±1.3 years (Prather et al., 2012) and an inter-hemispheric ratio in the range 0.85–0.98 (Montzka et al., 2000;Prinn et al., 2001;Krol and Lelieveld, 2003;Bousquet et al., 2005;Patra et al., 2014), while the ACCMIP model ensemble yields a τ of 9.7±1.5 years and an inter-hemispheric ratio of 1.28±0.10 (Naik et al., 2013).

~~Our prior estimate assumes no 2010–2018 trends in non-wetland emissions on the 4º×5º grid except for interannual variability in fires (GFED4s). In this manner, all information on anthropogenic emission trends is from the GOSAT observations.~~

The Bayesian inversion requires error statistics for the prior estimates. The prior error covariance matrix ($\mathbf{S}_a$) is constructed as follows. For mean non-wetland emissions, we assume 50% error standard deviation for individual grid cells and 20% for each source category when aggregated globally. ~~We~~For linear trends in non-wetland emissions, we specify an absolute error standard deviation of 5% a^{-1} for ~~linear trends of non-wetland emissions~~individual grid cells. For wetland emissions, we take the full error covariance structure (including spatial and temporal error covariance) derived from the WetCHARTs ensemble members for the 14 subcontinental regions (Bloom et al., 2017). For annual hemispheric OH concentrations, we assign 5% independent errors for individual years on top of a 10% ~~systematic~~ error for the ~~multi-year~~2010-2018 mean.

2.4 Forward model

We use the GEOS-Chem CTM v11.02 as forward model (***F***) for the inversion (Wecht et al., 2014;Turner et al., 2015;Maasakkers et al., 2019) that relates atmospheric methane observations (***y***) to the state vector to be optimized (***x***) as ***y***=***F***(***x***). The simulation is conducted at 4º×5º horizontal resolution with 47 vertical layers (~ 30 layers in the troposphere) and is driven by 2009–2018 MERRA-2 meteorological fields (Gelaro et al., 2017) from the NASA Global Modeling and Assimilation Office (GMAO). The prior simulation is conducted from 2010 to 2018. The initial conditions are from Turner et al. (2015) with ~~a~~an additional one-year spin-up starting from January 2009 to establish methane gradients driven by synoptic-scale transport (Turner et al., 2015). We further set the initial conditions on January 1, 2010 to be unbiased by removing the zonal mean biases relative to GOSAT observations. Thus we attribute any model departures from observations over the 2010–2018 period in the inversion to errors in sources and sinks over that period.

We use archived 3-D monthly fields of OH ~~concentration~~concentrations from a GEOS-Chem full chemistry simulation (Wecht et al., 2014) to compute the removal of methane from oxidation by tropospheric OH. Other minor loss terms include stratospheric oxidation computed with archived monthly loss frequencies from the NASA Global Modeling Initiative model (Murray et al., 2012), tropospheric oxidation by Cl atoms computed with archived Cl concentration fields from X. Wang et al. (2019b), and monthly soil uptake fields from Murguia-Flores et al. (2018). The inversion does not optimize these minor sinks. The loss from oxidation by Cl is 5.5 Tg a^{-1}, accounting for ~ 1% of methane loss. ~~This estimate by X. Wang et al. (2019b)~~It is lower than the previous estimate of 9 Tg a^{-1} (Sherwen et al., 2016) used by Maasakkers et al. (2019) ~~and~~but is consistent with a recent analysis of methane and CO isotopic signatures (Gromov et al., 2018). Use of monthly soil uptake fields from the Murguia-Flores et al. (2018) climatology of 2000-2009 data is another update relative to Maasakkers et al. (2019) and yields a global soil sink of 34 Tg a^{-1}.

2.5 Forward model bias correction

The GEOS-Chem simulated methane columns have a latitude-dependent background bias relative to the GOSAT data (Turner et al., 2015). This is thought to result from excessive meridional transport in the stratosphere, a common problem in global models (Patra et al., 2011). In particular, coarse-resolution global models have difficulty resolving polar vortex dynamics that control the distribution of stratospheric methane in the winter-spring hemisphere (Stanevich et al., ~~2019~~2020). GEOS-Chem model evaluation with stratospheric sub-columns derived from ground-based TCCON ~~column~~ measurements shows that the stratospheric bias varies seasonally (Saad et al., 2016). Previous GEOS-Chem based inversions of GOSAT data (Turner et al., 2015;Maasakkers et al., 2019) developed correction schemes by fitting differences between the prior model simulation and background GOSAT observations as a second-order polynomial function of latitude. However, these correction schemes did not consider the seasonal variation of the stratospheric biases. Moreover, they could falsely attribute high-latitude model-GOSAT differences to stratospheric model bias rather than to errors in prior emissions. Therefore, they had to exclude these high-latitude observations in their analysis (Turner et al., 2015;Maasakkers et al., 2019).

Here we improve the stratospheric bias correction by using satellite observations from ACE-FTS v3.6 (Waymark et al., 2014;Koo et al., 2017). ACE-FTS is a solar occultation instrument launched in 2003 ~~and~~that measures vertical profiles of stratospheric methane (Bernath et al., 2005). We compute correction factors to GEOS-Chem stratospheric methane sub-columns as a function of season and equivalent latitude, based on the ratios of stratospheric methane sub-columns between ACE-FTS and GEOS-Chem prior ~~simulations~~simulation for 2010-2015 (Figure 2). A global scaling factor (1.06) is applied to these correction factors to enforce mass conservation for methane in the stratosphere, so that the correction does not introduce a spurious stratospheric source/sink in the model simulation. We use equivalent latitude, computed on the 450 K isentropic surface from MERRA-2 reanalysis fields, as one of the predictors for parameterization. The equivalent latitude is a potential vorticity (PV) based coordinate that maps PV to latitude, based on areas enclosed by PV isopleths (Butchart and Remsberg, 1986), and is often used to represent the influence of high-altitude dynamics (e.g., polar vortex) on chemical tracers (~~e.g.,~~ Engel et al., 2006;Hegglin et al., 2006;Strahan et al., 2007). We use the same stratospheric bias correction for all years because the correction does not vary significantly for individual years (Figure S2). Figure 2 shows that GEOS-Chem model biases ~~tend~~are largely confined to ~~be large at~~ high latitudes of the winter-spring hemisphere~~.~~. By having our correction factors be dependent on equivalent latitude and ~~are small in the tropics and in the summer-fall hemisphere. Based on information provided by ACE-FTS observations, the model bias correction scheme is able to capture these seasonal and latitudinal variations, which are not resolved by a second-order polynomial function used in Turner et al. (2015) and Maasakkers et al. (2019). Furthermore~~season, we ~~can attribute the stratospheric bias as~~ specifically ~~due to~~account for the too weak polar vortex dynamical barrier ~~being too weak~~ in the model~~.~~ as the cause of the stratospheric bias (Stanevich et al., 2020).

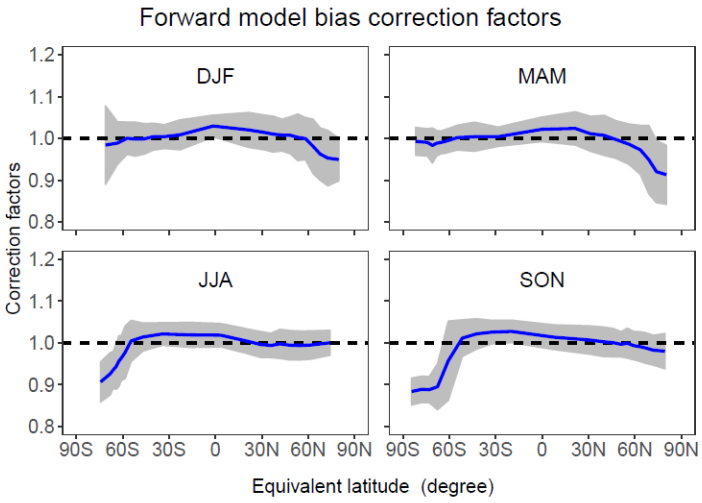

Figure 2. GEOS-Chem stratospheric bias correction based on ACE-FTS observations. ~~Correction factors for~~ The Figure shows the ACE-FTS to GEOS-Chem ratio of stratospheric methane subcolumns ~~are shown in blue lines~~ as a function of ~~season and~~ equivalent latitude~~.~~ and season, averaged over the 2010-2015 period. Grey shading represents the fitting unceratinty. ~~The correction factor is signficant poleward of 60 degrees in winter-spring, consistent with model error in accounting for polar vortex dynamics.~~

2.6 Inversion procedure

We perform the inversion by minimizing the Bayesian cost function (Brasseur and Jacob, 2017):

$$J(\boldsymbol{x}) = (\boldsymbol{x} - \boldsymbol{x}_\mathrm{a})^\mathrm{T}\mathbf{S}_\mathrm{a}^{-1}(\boldsymbol{x} - \boldsymbol{x}_\mathrm{a}) + \gamma(\boldsymbol{y} - \mathbf{K}\boldsymbol{x})^\mathrm{T}\mathbf{S}_\mathrm{O}^{-1}(\boldsymbol{y} - \mathbf{K}\boldsymbol{x}) \quad (2)$$

~~Here~~Here the Jacobian matrix $\mathbf{K}$ ($= \frac{\partial \boldsymbol{y}}{\partial \boldsymbol{x}}$) is a linearized description of the forward model ($\boldsymbol{F}$)that relates $\boldsymbol{y}$ (observations) to $\boldsymbol{x}$ (state vector). We explicitly compute the Jacobian matrix by perturbing each individual element of $\boldsymbol{x}$ independently in GEOS-Chem simulations and calculating the sensitivity of $\boldsymbol{y}$ to that perturbation. $\boldsymbol{x}_\mathrm{a}$ is the prior estimate for $\boldsymbol{x}$ and $\mathbf{S}_\mathrm{a}$ is the prior error covariance matrix (Section 2.3). $\mathbf{S}_\mathrm{O}$ is the observation error covariance matrix including contributions from the instrument error and the forward model error. We take $\mathbf{S}_\mathrm{O}$ ~~is taken~~ to be diagonal and compute the variance terms ~~are computed with~~from the statistics of the residual error ~~method of~~ ($\boldsymbol{\varepsilon}_O = \boldsymbol{y} - \boldsymbol{F}(\boldsymbol{x}_a) - \overline{\boldsymbol{y} - \boldsymbol{F}(\boldsymbol{x}_a)}$ where the overbar denotes annual averages in a 4°× 5° grid cell) that represents the random component of model-observation differences (Heald et al.~~ (.,~~2004~~) as~~). This method of constructing $\mathbf{S}_\mathrm{O}$ has been previously applied to GOSAT observations by Turner et al. (2015) and Maasakkers et al. (2019). The observational error standard deviation ~~averages 13 ppbv. The Jacobian matrix $\mathbf{K} = \frac{\partial \boldsymbol{y}}{\partial \boldsymbol{x}}$ that relates $\boldsymbol{y}$ (observations) to $\boldsymbol{x}$ (state vector) is a linearized description of the forward model. We explicitly compute the Jacobian matrix by perturbing each individual element of $\boldsymbol{x}$ independently in GEOS-Chem and calculating the sensitivity of $\boldsymbol{y}$ to that perturbation. $\boldsymbol{x}_\mathrm{a}$ is the prior estimate for $\boldsymbol{x}$ and $\mathbf{S}_\mathrm{a}^{-}$ is the prior error covariance matrix (Section 2.3).~~ derived in this manner averages 13 ppbv. γ is the

regularization parameter taken to be 0.05 following Y. Zhang (2018) and Maasakkers et al. (2019) to account for missing error covariance structure in $\mathbf{S}_O$.

Minimizing $J(\boldsymbol{x})$ (Eq. 2) by solving $dJ/d\boldsymbol{x}=0$ analytically (Rodgers, 2000; Brasseur and Jacob, 2017) yields a best posterior estimate of the state vector ($\hat{\boldsymbol{x}}$) and the associated posterior error covariance matrix ($\hat{\mathbf{S}}$) characterizing the error statistics of $\hat{\boldsymbol{x}}$:

$$\hat{\boldsymbol{x}} = \boldsymbol{x}_a + (\gamma \mathbf{K}^T \mathbf{S}_O^{-1} \mathbf{K} + \mathbf{S}_a^{-1})^{-1} \gamma \mathbf{K}^T \mathbf{S}_O^{-1} (\boldsymbol{y} - \mathbf{K}\boldsymbol{x}_a), \quad (3)$$

$$\hat{\mathbf{S}} = (\gamma \mathbf{K}^T \mathbf{S}_O^{-1} \mathbf{K} + \mathbf{S}_a^{-1})^{-1}, \quad (4)$$

From there we derive the averaging kernel matrix $\mathbf{A} = \partial\hat{\boldsymbol{x}}/\partial\boldsymbol{x}$ describing the sensitivity of the solution to the true state

$$\mathbf{A} = \mathbf{I} - \hat{\mathbf{S}}\mathbf{S}_a^{-1}. \quad (5)$$

The trace of the averaging kernel matrix is referred to as the degrees of freedom for signal (DOFS) (Rodgers, 2000) and represents the number of independent pieces of information on the state vector that are constrained by the inversion. We refer to the diagonal terms of **A** as averaging kernel sensitivities, which measure the ability of the observations to quantify the individual elements of the state vector (Sheng et al.,2018c;Maasakkers et al., 2019).

The posterior solution is often presented in reduced dimensionality. For example, spatially resolved emission and trend estimates on the 4°×5° grid can be aggregated to countries or regions, or to global/regional emissions from individual source sectors (~~e.g.,~~ oil/gas, livestock, etc.). Let **W** be a matrix that represents the linear transformation from the full state vector to a reduced state vector. The posterior estimation of the reduced state vector ($\hat{\boldsymbol{x}}_{red}$) is computed as

~~$\hat{\boldsymbol{x}}_{red} = \mathbf{W}\hat{\boldsymbol{x}}.$ (6)~~

$$\hat{\boldsymbol{x}}_{red} = \mathbf{W}\hat{\boldsymbol{x}}, \quad (6)$$

with posterior error covariance matrix

~~$\hat{\mathbf{S}}_{red} = \mathbf{W}\hat{\mathbf{S}}\mathbf{W}^T$ (7)~~

$$\hat{\mathbf{S}}_{red} = \mathbf{W}\hat{\mathbf{S}}\mathbf{W}^T, \quad (7)$$

and averaging kernel matrix

~~$\mathbf{A}_{red} = \mathbf{W}\mathbf{A}\mathbf{W}^*$ (8)~~

$$\mathbf{A}_{red} = \mathbf{W}\mathbf{A}\mathbf{W}^*, \quad (8)$$

where $\mathbf{W}^* = \mathbf{W}^T(\mathbf{W}\,\mathbf{W}^T)^{-1}$ is the pseudo-inverse of **W**. ~~The advantage of this approach is that the derived~~The regional/global budget terms and their error covariance structures obtained by this approach are consistent with the full inversion. In the case of aggregation by sectors, we construct **W** on the basis of the relative contribution of the sector to the prior emissions in each 4°×5° grid cell. This does not assume that the prior distribution of sectoral emissions is correct, only that the relative allocation within a given 4°×5° grid cell is correct.

~~2.7~~3 Evaluation of ~~posterior simulation~~the inversion results

We conduct a posterior simulation driven by the optimized (posterior) distributions of methane emissions, emission trends, and OH concentrations to evaluate the inversion. The posterior simulation results are compared with the training data (GOSAT) as well as independent evaluation data including TCCON total column measurements (tccondata.org) (Wunch et al., 2011) and NOAA surface measurements (www.esrl.noaa.gov/gmd/ccgg/flask.php) (Dlugokencky et al., 2020). Figure 3 shows the GEOS-Chem comparison to the GOSAT data. As expected for a successful inversion, the posterior simulation achieves a better fit to GOSAT observations than the prior simulation, both spatially and temporally~~.~~, with root-mean-square errors reduced by 69% (prior: 45 ppbv; posterior: 14 ppbv). The prior simulation ~~has~~shows a negative bias that grows with time and ~~is particularly large in the extratropical northern hemisphere and tropics. The prior biases have~~has a large seasonal structure presumably associated with errors in wetland emissions. The prior biases also have prominent spatial patterns particularly in the extratropical northern hemisphere and tropics. All these error features largely vanish in the posterior simulation through the optimized adjustment of the state vector~~.~~ (Figure 3).

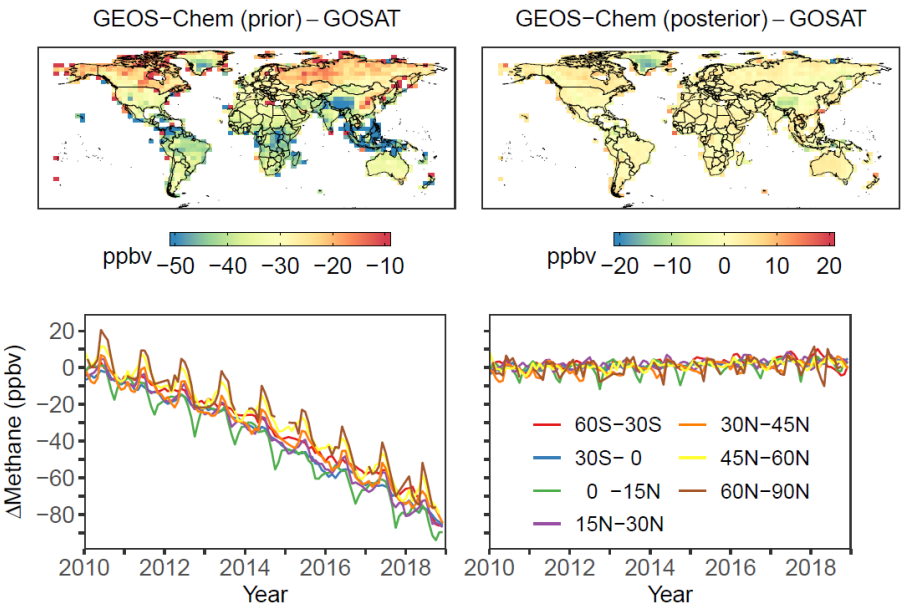

Figure 3. Difference of methane columns between GEOS-Chem simulations and GOSAT observations. Results are shown for GEOS-Chem using prior (left) and posterior (right) state vector estimates, and for spatial distribution averaged during 2010–2018 (top) and monthly time series of zonal means in different latitude bands (bottom). Note different color scales in the top panels. Tick marks of *x* axes in bottom panels represent January of each year. Figure S6 plots the right bottom panel in an expanded ordinate scale.

Figure 4 presents evaluations against independent 2010–2018 observations from TCCON and NOAA sites, arranged by latitude. Values are shown as the root mean square error (RMSE) for individual sites. Figure 4 shows that the inversion substantially improves the agreement between simulations and observations for all TCCON sites and almost all NOAA surface sites. Average root-mean-square errors are reduced by 60% for TCCON sites (prior: 38 ppbv; posterior: 15 ppbv) and by 33% for NOAA surface sites (prior: 42 ppbv; posterior: 28 ppbv). The seasonal component of the errors (root-mean-square errors computed from monthly mean model-observation differences after annual mean biases are removed, not shown in figure) are reduced on average by 44% for TCCON sites (prior: 6.6 ppbv; posterior: 3.7 ppbv) and 27% for surface sites (prior: 11 ppbv; posterior: 8 ppbv), primarily owing to optimized seasonal variations in wetland emissions. In addition, we do not find large interannual variability of posterior biases that could be associated with climate oscillations such as ENSO (Figure S3).

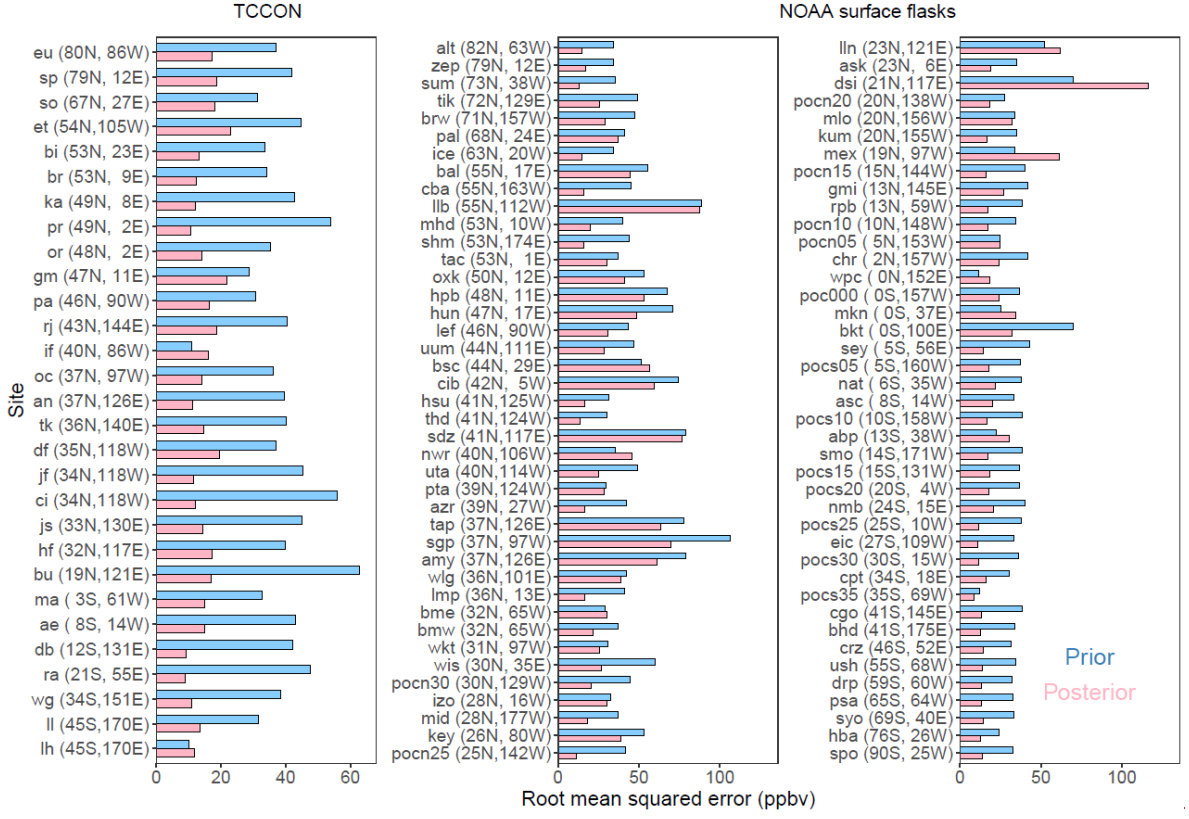

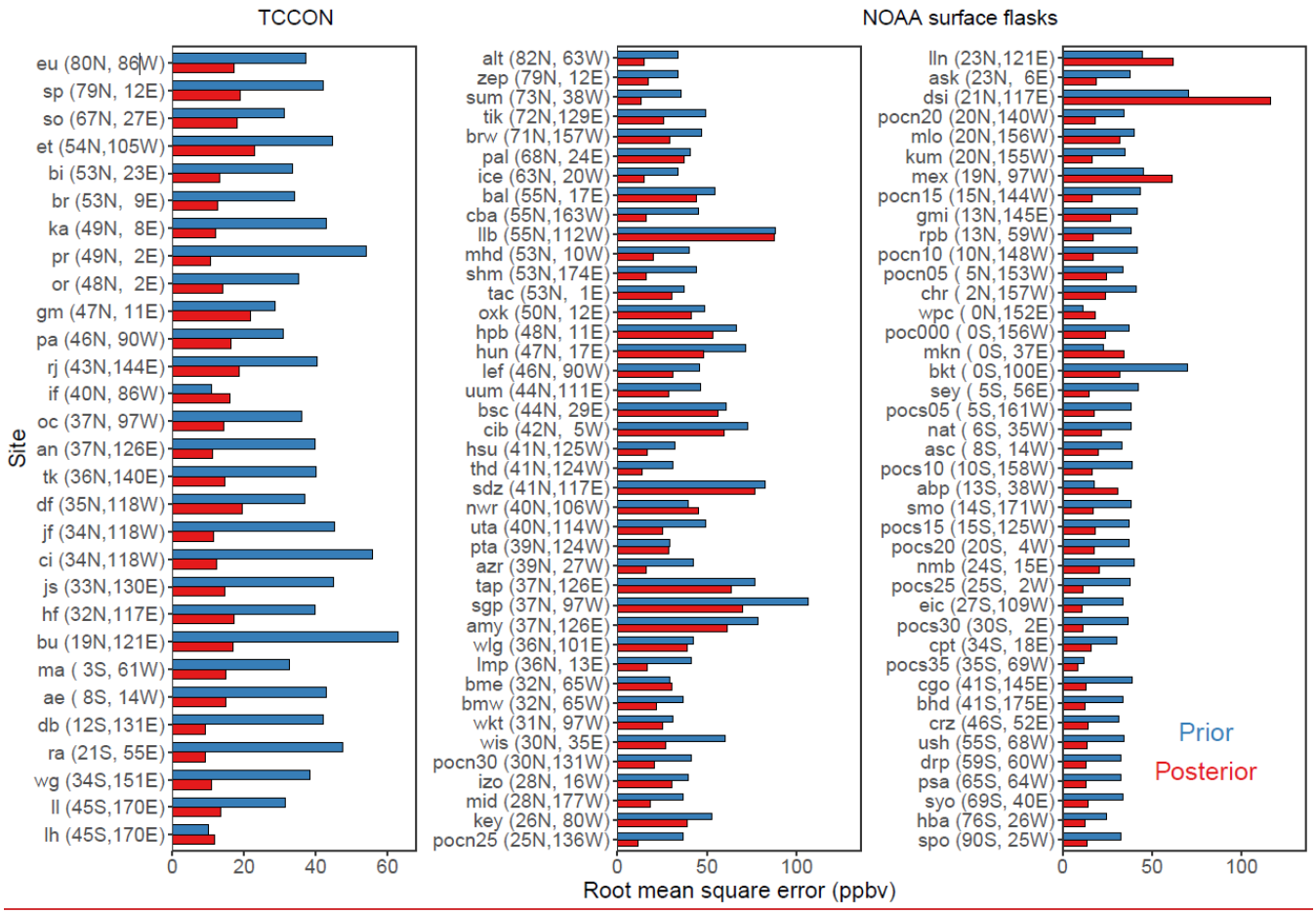

Figure 4. Root mean square errors of prior and posterior GEOS-Chem simulations relative to TCCON observations of dry column methane mixing ratios (left) and NOAA observations of surface air mixing ratios (middle and right). Observation sites are arranged by latitude. Data are for 2010–2018. Site names are shown along with their latitude and longitude (more information about these sites can be found at tccon-wiki.caltech.edu/Sites and www.esrl.noaa.gov/gmd/dv/site/index.php?program=ccgg). A mountain-top TCCON site located at Zugspitze, Germany (zs; ~ 3000 m.a.s.l.) is excluded because the terrain effect on the total column is not resolved by the coarse resolution model.

The posterior error covariance matrix $\hat{\mathbf{S}}$ resulting from analytically solving the Bayesian problem allows us to analyse the error structure of posterior estimates. Figure 5 plots the posterior joint probability density functions (PDFs) for pairs of global budget terms and their trends (computed following Eq. 6-7). A strong negative error correlation in the inversion results is found between global anthropogenic emissions and methane lifetime (r=-0.8), reflecting limited ability of the inversion to separate the two. In contrast, error correlations between wetland emissions and methane lifetime (r=-0.4), and between wetland and anthropogenic emissions (r=-0.2) are much smaller. We find moderate error correlations between the OH trend and either wetland or anthropogenic emission trends (r=-0.6). Improved separation of global budget terms and their trends may be

achieved by including additional information from surface observations (Lu et al., 2020) and from thermal infrared satellite observations (Y. Zhang et al., 2018).

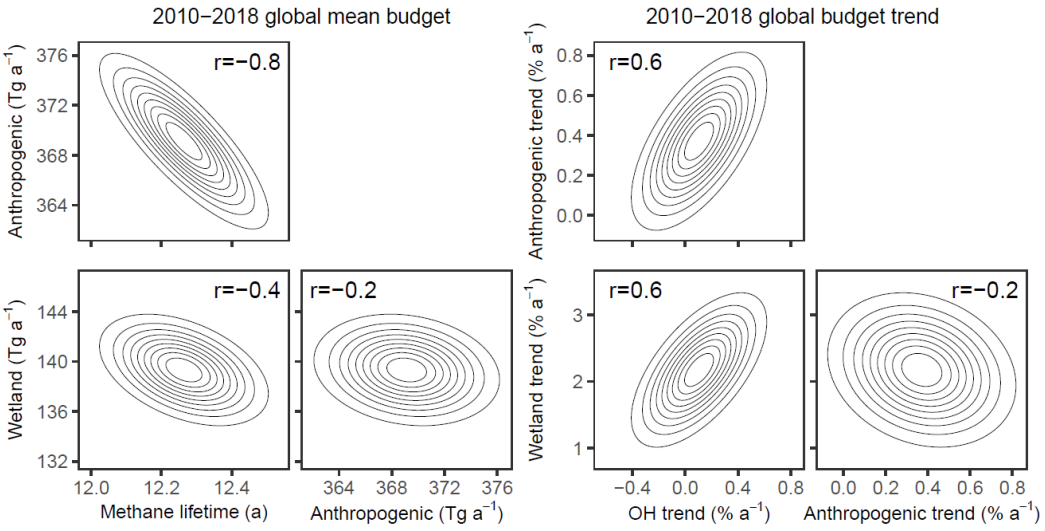

Figure 5. Error correlations between global anthropogenic emissions, wetland emissions, and tropospheric OH concentrations (methane lifetime against oxidation by tropospheric OH; τ) in the inverse solution. Results are shown both for 2010–2018 mean values and for 2010–2018 trends. The error correlations are presented as joint probability density functions for pairs of reduced global state vector elements. Confidence ellipses represent probability of 0.1 (innermost) to 0.9 (outermost) at intervals of 0.1. The error correlation coefficients are shown inset.

~~3~~Figure 6 further examines the error aliasing of estimates for anthropogenic and wetland emissions within or between regions. For this analysis, anthropogenic emissions optimized on the 4º×5 º grid are aggregated to 14 subcontinental regions used for estimating wetland emissions. We find only moderate negative error correlations (r=-0.1– -0.5) between estimates for anthropogenic and wetland emissions within the same region (diagonal of top left quadrant), suggesting that the inversion is able to separate the two. Cross-region error correlations are generally small for anthropogenic emissions (bottom left quadrant of Figure 6), but have a complex structure for wetland emissions (top right quadrant of Figure 6). For example, errors are positively correlated between Sub-Sahara Africa and southern Africa wetlands (r=0.6), but are negatively correlated between East Canada and northern Europe wetlands (r=-0.4).

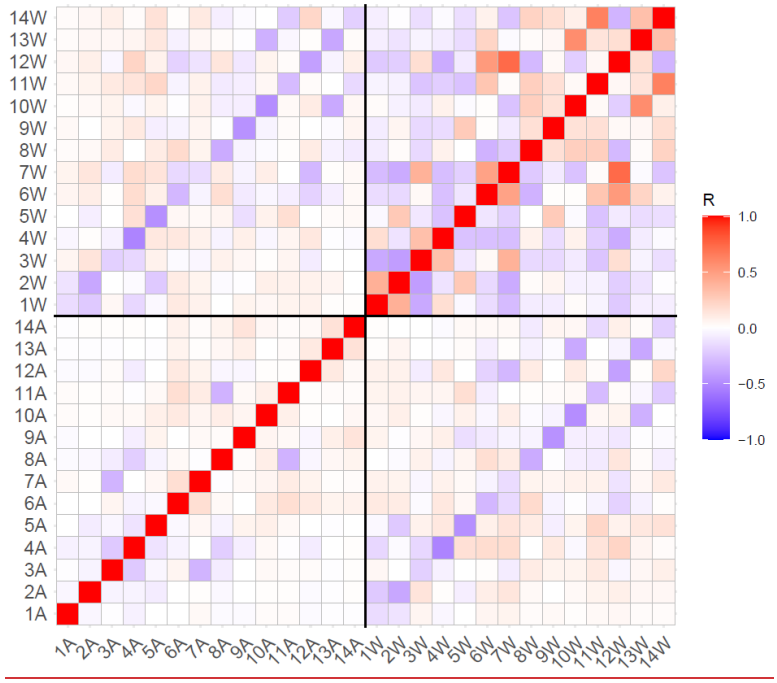

Figure 6. Posterior error correlations between regional anthropogenic and wetland emissions. To examine error aliasing at regional scale, anthropogenic emissions resolved on the 4º×5 º grid are aggregated to the 14 subcontinental regions of Figure 1 used for optimizing wetland emissions. Numbers (1-14) are region index as Figure 1. "A" or "W" stands for anthropogenic or wetland emissions, respectively. For example, 5A stands for anthropogenic emissions from Temprate North America.

4 Results and discussion

~~3~~4.1 Anthropogenic emissions

Figure ~~5~~7 shows the correction factors from the inversion to 2010–2018 mean non-wetland emissions (posterior/prior ratios) along with the associated averaging kernel sensitivities (corresponding diagonal terms of the averaging kernel matrix). ~~The averaging kernel sensitivities largely follow the pattern of prior emissions and are highest in major anthropogenic source regions.~~ We achieve 179 independent pieces of information (DOFS) for constraining the emissions on the 4º×~~5 º~~5º grid. ~~By applying the posterior/prior correction factors to the prior~~The spatial distribution of ~~each anthropogenic emission sector, we obtain improved estimates for anthropogenic emissions for~~averaging kernel sensitivities largely follows the pattern of prior emissions (right panel of Figure 5). The inversion provides strong constraints in major anthropogenic source regions such as East Asia, South Asia, and South America. The constraints are generally weaker over North America, Europe, and Africa, indicating that ~~sector.~~the inversion provides more diffuse spatial information in these regions.

We find that the prior emission inventory significantly overestimates anthropogenic emissions in eastern China (Figure ~~5~~7). The posterior estimate of Chinese anthropogenic emissions (48±1 Tg a^{-1}) is 30% lower than the prior estimate (67 Tg a^{-1}), and is also lower than the latest national report from China to the UNFCCC of 55 Tg a^{-1} for 2014 (Figure ~~6~~8). Based on the relative contribution of each sector in the prior inventory, we attribute ~ 60% of this downward correction to coal mining. The overestimation of anthropogenic emissions from China has been reported by previous global and regional GOSAT inversion studies using different EDGAR inventory versions as prior estimates (Monteil et al., 2013;Thompson et al., 2015;Turner et al., 2015;Maasakkers et al., 2019;Miller et al., 2019).

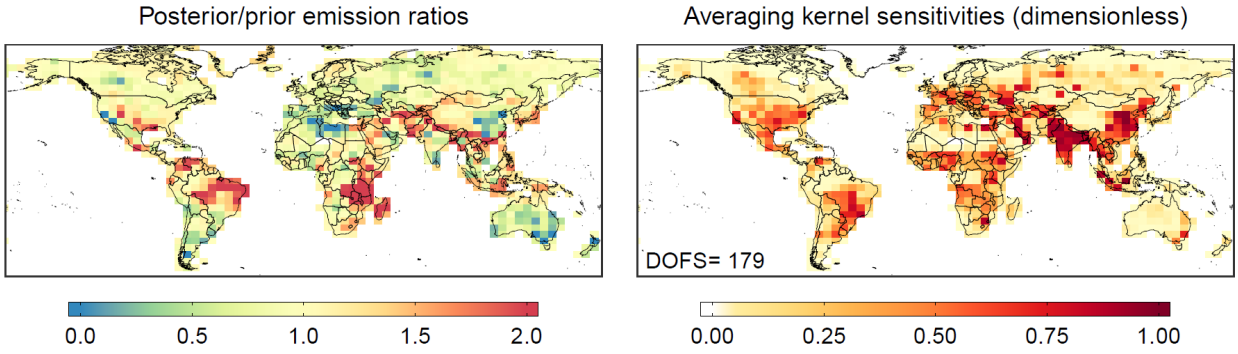

Figure 7. Corrections to prior estimates of 2010–2018 mean non-wetland methane emissions. (Left) posterior/prior emission ratios. Figure S7 shows the same corrections as posterior – prior emission differences. (Right) averaging kernel sensitivities (diagonal elements of the averaging kernel matrix). The averaging kernel sensitivities measure the ability of the observations to constrain the posterior solution (0 = not at all, 1 = fully). The sum of averaging kernel sensitivities defines the degrees of freedom for signal (DOFS), shown inset.

Another major downward correction is for the oil/gas producing regions in Russia. We estimate Russia's anthropogenic emissions to be ~~21~~19±1 Tg a^{-1}, as opposed to the prior estimate of 36 Tg a^{-1} (Figure ~~6~~8), and the difference is mainly attributable to the oil/gas sector (posterior: 15 Tg a^{-1}; prior: 27 Tg a^{-1}). This finding is consistent with Maasakkers et al. (2019) though they used a different oil/gas emission inventory. Russia has been revising downwards its national emission estimates submitted to the UNFCCC, and our posterior estimate of total anthropogenic emissions is closer to the country's latest submission to UNFCCC for 2010–2018 (16 Tg a^{-1}; Figure ~~6~~8). The new submission revises oil/gas methane emissions downward by a factor of 3 relative to the previous submission used as prior estimate in our inversion (Scarpelli et al., 2020).

We find large upward corrections to the prior inventory over ~~eastern~~East Africa (Mozambique, Zambia, Tanzania, Ethiopia, Uganda, Kenya, and Madagascar) and over South America (Brazil). A previous inversion suggested that corrections for these regions may be due to an underestimation of prior wetland emissions (Maasakkers et al., 2019). Our inversion, which optimizes wetland and anthropogenic emissions separately, ~~more specifically attributes the underestimation to livestock emissions. The upward correction pattern in Brazil is located near the country's "agricultural frontier" where forest is converted to agricultural lands for livestock and crops (Nepstad et al., 2019). Herrero et al. (2013) identified eastern Africa as the region of the highest~~

~~livestock emission intensity (emission/kg protein) because of low feed efficiency, suggesting that emission factors in this region may be underestimated in bottom-up calculation given a general lack of region-specific information for developing countries.~~attributes the underestimation to anthropogenic emissions (also see Section 4.3 for wetland results), though there is some error aliasing between them (r=-0.5 for Sub-Sahara Africa, -0.4 for Southern Africa; Figure 6). We find that the upward correction over East Africa generally remains robust in a sensitivity inversion where prior wetland emissions in a neighbouring region (Sudd in South Sudan) are increased by a factor of 3 (Figure S4 and Figure 8). Based on prior sectoral information, these underestimations are most likely due to livestock emissions, whose bottom-up estimates have large uncertainties in these developing regions (Herrero et al., 2013).

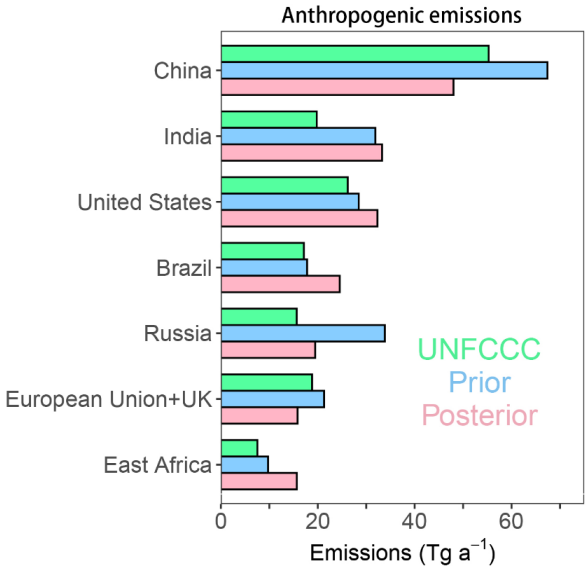

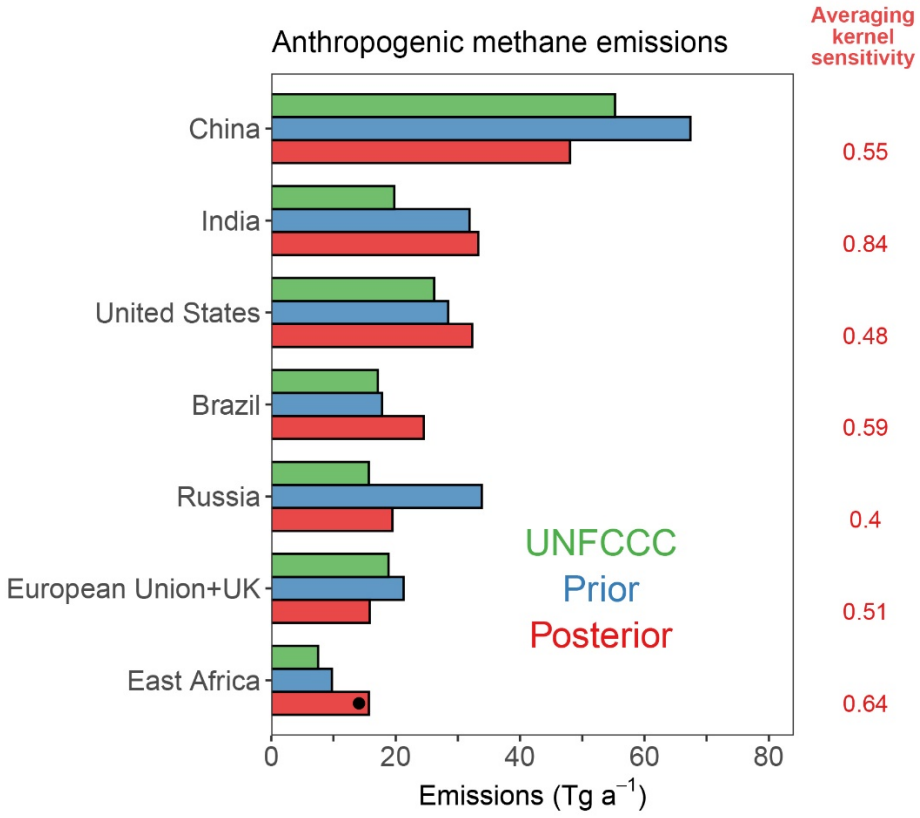

Figure 8. National and regional estimates of 2010–2018 mean methane emissions from anthropogenic sources. Included are the top 5 individual countries in our posterior estimates, the European Union (including the United Kingdom), and East Africa (including Mozambique, Zambia, Tanzania, Ethiopia, Uganda, Kenya, and Madagascar). The UNFCCC record is from di.unfccc.int (accessed on July 10, 2020). Non-Annex I countries do not report yearly emissions to the UNFCCC and for those we use the latest UNFCCC submissions (Brazil, 2015; China, 2014; Ethiopia, 2013; India, Madagascar, Kenya, 2010; Uganda, Zambia, 2000; Mozambique, Tanzania, 1994). Inset are the averaging kernel sensitivities for these national and regional aggregated results, which measure the ability of the observations to constrain the posterior solution (0 = not at all, 1 = fully). The dot for East Africa represents the estimate inferred from a sensitivity inversion with prior spatial distribution of African wetlands perturbed.

Another upward correction pattern in South America is located near Venezuela, a major oil producing country in the region. The large ~~discrepancy~~correction in Venezuela likely reflects underestimation of fossil fuel emissions by the national estimates for 2010 reported to UNFCCC. Upward corrections are also seen in central Asia (Iran, Turkmenistan), where the regional posterior estimates (11.7±0.9 Tg a^{-1}) are 43% higher than the prior (8.2~~±1.4~~ Tg a^{-1}), with adjustments mainly attributed to the oil/gas sector. This region has previously been identified by satellite observations as a methane emission hotspot (Buchwitz et al., 2017; Varon et al., 2019; Schneising et al., 2020).

The inversion finds small upward corrections over the ~~US~~U.S. (prior: 28 Tg a^{-1}; posterior: 32±1 Tg a^{-1}) (Figure ~~6~~8), resulting mainly from underestimation of emissions from the oil/gas sector in the western and ~~southwestern US~~ south-central U.S. (Figure ~~5~~7). This result is ~~broadly~~ consistent with a high-resolution inversion over the U.S. using the 2010–2015 GOSAT data, which spatially allocates the correction more specifically to oil/gas basins (Maasakkers et al., 2020). A number of ~~basin-level~~previous studies ~~based on aircraft and satellite measurements~~have found that emissions from oil/gas production are underestimated in the national US inventory (e.g., Kort et al., 2014;~~Karion et al., 2015;~~ Smith et al., 2017;~~Schwietzke et al., 2017;~~ Peischl et al., 2018;~~Cui~~ Alvarez et al., ~~2019~~2018;Y. Zhang~~,~~ et al., 2020;Gorchov Negron et al.,~~ 2020; Schneising et al., 2020) and national assessments of methane emissions from oil/gas production (Alvarez et al., 2018;Maasakkers,~~ 2020).

Small downward corrections with a diffuse pattern are found over Europe. The posterior estimate of anthropogenic emissions for the European Union (including the UK) is 16±0.7 Tg a^{-1}, slightly lower than the prior estimate (21 Tg a^{-1}) and the UNFCCC national reports (19 Tg a^{-1} for 2014) (Figure ~~6~~8). Source sector attribution is difficult in this case because of spatial overlap between emission sectors. The inversion finds only small adjustments to prior emissions for India (prior: 32 Tg a^{-1}; posterior: 33±0.6 Tg a^{-1}) even though the information content is relatively large, confirming the prior inventory used in the inversion. Our estimate, however, is much higher than a previous inversion study for India (Ganesan et al., 2017) (22 Tg a^{-1}), which found their result in agreement with India's UNFCCC report (20 Tg a^{-1} for 2010) (Figure ~~6~~8). ~~The~~Our inversion attributes the discrepancy ~~is~~with the UNFCCC submission mainly ~~in~~to the livestock sector~~, which we find to be greatly underestimated in the UNFCCC submission. Livestock emission trends in India are discussed further below.~~.

~~3~~4.2 Anthropogenic emission trends

Figure ~~7~~9 shows the spatial distribution of 2010–2018 trends for anthropogenic emissions inferred from GOSAT observations, along with the associated averaging kernel matrix sensitivities. The GOSAT observations provide 42 pieces of information to constrain the spatial distribution of anthropogenic emission trends~~. The~~, suggesting that, compared to mean emissions, the inversion is only able to constrain more diffuse spatial patterns for emission trends. These constraints are strongest in China and India, but there is also fairly strong information aggregated over other continental regions. The prior estimate assumed ~~no~~zero anthropogenic trends anywhere, therefore the posterior trends are driven solely by the GOSAT information. ~~The corresponding diagonal elements of the posterior error covariance matrix allow us to quantify error standard deviations on the results.~~

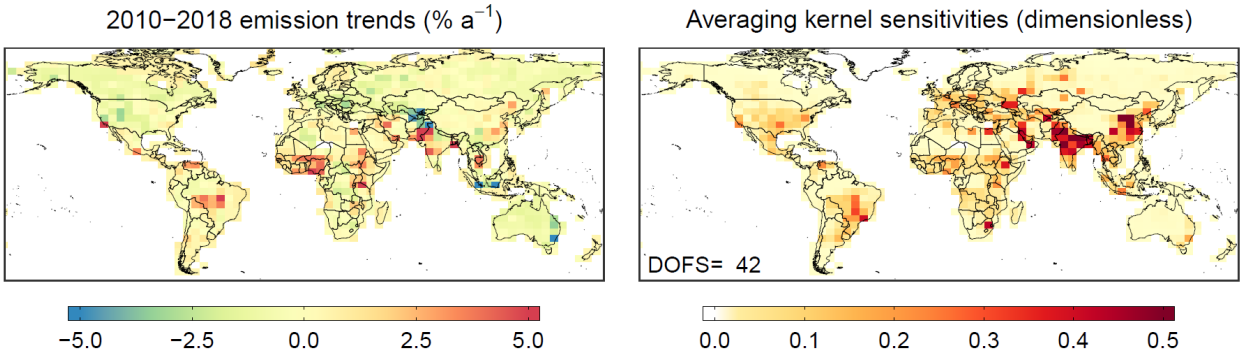

Figure 9. Anthropogenic methane emission trends for 2010–2018, as informed by GOSAT observations. (Left) Relative emission trends on the 4°×5° grid. Absolute emission trends are shown in Figure S8. (Right) Averaging kernel sensitivities~~.~~ that measure the ability of the observations to constrain the posterior solution (0 = not at all, 1 = fully). Degrees of freedom for signal (DOFS) is inset.

Significant positive trends of anthropogenic emissions are found in South Asia (0.57±0.16 Tg a^{-1} a^{-1} or 1.3±0.4% a^{-1}; Pakistan and India), East Africa (0.21±0.10 Tg a^{-1} a^{-1} or 1.4±0.6 % a^{-1}; Ethiopia, Tanzania, Uganda, Kenya, and Sudan), West Africa (0.32±0.10 Tg a^{-1} a^{-1} or 4.6±1.4% a^{-1}; Nigeria, Niger, Ghana, Cote d'Ivoire, Mali, Benin, Burkina Faso), and Brazil (0.17±0.15 Tg a^{-1} a^{-1} or 0.7±0.6% a^{-1}). ~~All these regions are seeing rapid increases in livestock populations. According~~Based on prior sectoral fractions in each 4°×5° grid cell, we attribute these positive trends mostly to the livestock sector (0.40 Tg a^{-1} a^{-1} in South Asia, 0.13 Tg a^{-1} a^{-1} in East Africa, 0.15 Tg a^{-1} a^{-1} in West Africa, and 0.11 Tg a^{-1} a^{-1} in Brazil). Indeed, according to the United Nations Food and Agriculture Office (UNFAO) statistics~~, the~~ (http://www.fao.org/faostat), all these regions have had rapid increases in livestock population. The fastest growing cattle populations in the world reported by the UNFAO over the 2010–2016 period were Pakistan (1.4×10^6 heads a^{-1}), Ethiopia (1.2×10^6 heads a^{-1}), Tanzania (1.1×10^6 heads a^{-1}), and Brazil (0.9×10^6 heads a^{-1}). ~~Indeed, our sectoral attribution of the trends in Figure 7 attributes them mostly to livestock (0.40 Tg a^{-1} a^{-1} in South Asia, 0.13 Tg a^{-1} a^{-1} in East Africa, 0.15 Tg a^{-1} a^{-1} in West Africa, and 0.11 Tg a^{-1} a^{-1} in Brazil). Our~~Moreover, our inversion results for these regional trends in livestock emissions are generally consistent in magnitude with the trends from bottom-up livestock emission inventories (FAOSTAT, IPCC tier I method; EDGAR v4.3.2 and v5, hybrid tier I method; Chang et al. (2019), IPCC tier II method~~), as shown in~~) (Figure ~~8~~10~~. Anthropogenic~~). Because our inversion assumes zero prior trends in anthropogenic emissions, the inferred trends are solely informed by satellite observations and independent of bottom-up trends in Figure 10. Taking together, anthropogenic methane emission trends in South Asia, Africa, and Brazil add up to 1.3 Tg a^{-1} a^{-1}, which as we will show below amounts to the global anthropogenic emission trend~~.~~ (with trends over other regions and sectors almost cancelling out).

A positive trend in anthropogenic emissions (0.27±0.20 Tg a^{-1} a^{-1} or 0.6±0.4% a^{-1}) is found over China driven by coal mining (northern China) and rice (southern China), but the magnitude of the trend is much smaller than previous inverse analyses of

satellite and surface observations for time horizons before 2015 (Bergamaschi et al., 2013;Thompson et al., 2015;Patra et al., 2016;Saunois et al., 2017;Miller et al., 2019;Maasakkers et al., 2019). We infer a much stronger trend (0.72±0.39 Tg a^{-1} a^{-1} or 1.6±0.9% a^{-1}) for China if we restrict the GOSAT record to 2010–2016. Our results thus suggest that anthropogenic emission trends in China peaked midway within the 2010–2018 record. Indeed, coal production in China peaked in 2013 (Sheng et al., 2019).

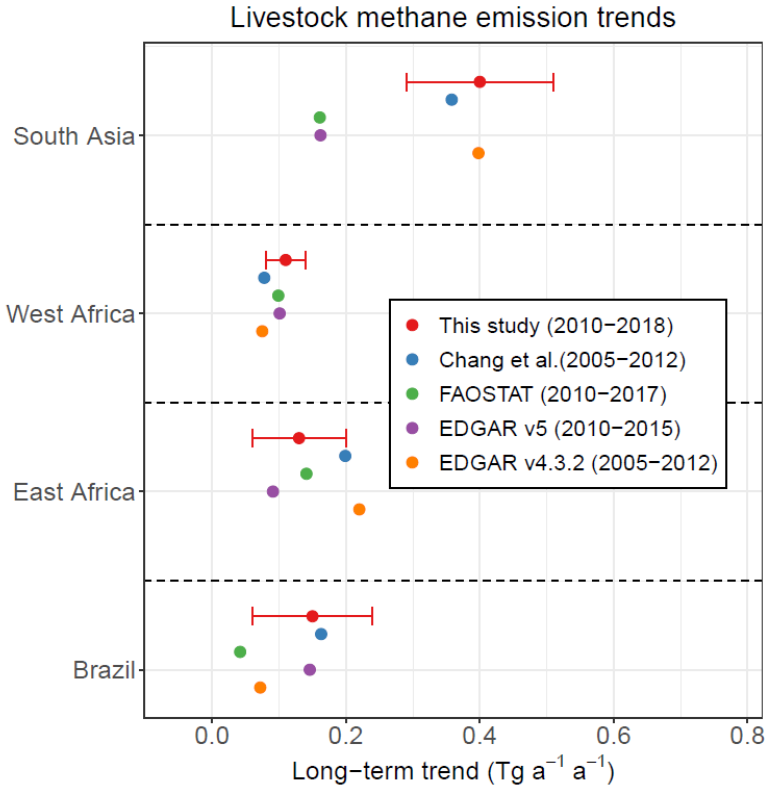

Figure 10. Regional trends in anthropogenic methane emissions from livestock. Our GOSAT inversion results for 2010-2018 (with error standard deviations) are compared to estimates from different bottom-up inventories over the 2005-2017 period: Chang et al. (2019), FAOSTAT (2020), EDGAR v5 (Crippa et al., 2019), and EDGAR v4.3.2 (Janssens-Maenhout et al., 2017). Results are shown for South Asia (India and Pakistan), West Africa (Nigeria, Côte d'Ivoire, Mali, Niger, Burkina Faso, Cameroon, Ghana, and Benin), East Africa (Ethiopia, Kenya, Uganda, and Tanzania), and Brazil. ~~Our inversion assumes no~~By assuming zero prior ~~trend~~trends in anthropogenic emissions, ~~thus~~our inversion does not use trend information in any of these bottom-up inventories; the trends inferred ~~trends~~by the inversion are solely from the GOSAT observations.

The inversion does not find significant 2010–2018 trends in anthropogenic emissions over the ~~US~~U.S. (-0.12±0.21 Tg a^{-1} a^{-1}, -0.4% a^{-1}). This is generally consistent with the lack of trend of ~~US~~U.S. emissions over 2000–2014 in inversions collected by the Global Carbon Project (Bruhwiler et al., 2017) and over 2010–2015 in a North America regional inversion using GOSAT data (Maasakkers et al., 2020). It contradicts the 2-3% a^{-1} positive trend inferred from direct analysis of GOSAT enhancements

(Turner et al., 2016; Sheng et al., 2018a) and the inference of large positive trends based on increasing concentrations of ethane and propane (Franco et al., 2016;Hausmann et al., 2016;Helmig et al., 2016). Bruhwiler et al. (2017) pointed out that the inference of methane emission trends from simple analysis of GOSAT data could be subject to various biases including variability in background and seasonal sampling, which would be accounted for in an inversion. Increasing ethane/methane and propane/methane emission ratios may confound inference of methane emission trends from ethane and propane records (Lan et al., 2019).

Small negative trends are found in Central Asia (Uzbekistan, Kazakhstan, Turkmenistan, Afghanistan; -0.20±0.16 Tg a^{-1} a^{-1}), Europe (-0.15±0.15 Tg a^{-1} a^{-1}), Australia (-0.12±0.07 Tg a^{-1} a^{-1}). The decrease in Central Asia is attributed mainly to oil/gas, and the decrease in Australia to coal mining and livestock. Trends over Europe and Russia are too diffuse to be separated by sectors. No significant trend is found in Russia (-0.08±0.25 Tg a^{-1} a^{-1}).

~~3~~4.3 Wetland emissions

We infer from the inversion ~~monthly~~ wetland emissions for 14 subcontinental regions (Figure 1) and for individual ~~years~~months from 2010 to 2018, thus allowing for seasonal and interannual variability to be optimized. This achieves 167 independent pieces of information (DOFS) for wetland emissions. The results are presented as mean seasonal cycles (Figure ~~9~~11) and time series of annual means (Figure ~~10~~12~~). We~~). Recent studies found that the mean WetCHARTs inventory used here as prior estimate is too high in the Congo Basin and too low in the Sudd region (Lunt et al., 2019; Parker et al., 2020b; Pandey et al., 2020). Our inversion is unable to resolve this subregional spatial correction pattern, because of coarse resolution in the wetland state vector (Figure 1). We therefore perform a sensitivity inversion with modified prior estimates following Lunt et al (2019) (Figure S1), which finds a 20% (3 Tg a^{-1}) increase in estimates of the 2010–2018 average for Sub-Sahara Africa and a 7% (0.6 Tg a^{-1}) increase for southern Africa, relative to the base inversion (Figure S5). Interannual trends and seasonal cycles are almost unchanged between two inversions (Figure S5).

As shown in Figure 11 and Figure 12, our results find lower wetland emissions than the mean of the WetCHARTs ensemble (prior estimate) over the Amazon, Temperate North America (the ~~US,~~U.S.), and East Canada. The previous inversion of GOSAT data by Maasakkers et al. (2019) also found overestimation of emissions by WetCHARTs in the coastal ~~US~~U.S. and Canada wetlands, but did not have significant corrections over the Amazon. The overestimation of wetland emissions in the ~~US~~U.S. and eastern Canada is also reported in analyses of aircraft measurements in the southeast ~~US~~U.S. (Sheng et al., 2018b) and surface observations in Canada (Baray et al., 2019), both of which used WetCHARTs v1.0 as prior information. The ~~downregulation~~downward correction of North American emissions is consistent with recent WetCHARTs updates (v1.2.1) ~~represent~~that substantially ~~reduced~~reduces methane emissions across regions categorized as partial wetland complexes (Lehner & Döll, 2004; Bloom et al., ~~2017). Recent studies found that WetCHARTs overestimates wetland emissions in the Congo~~

~~Basin but underestimates in the Sudd region (Lunt et al., 2019; Parker et al., 2020b; Pandey et al., 2020). Our inversion is unable to resolve this spatial correction pattern, because of coarse resolution in the wetland state vector (both regions are in Sub-Sahara Africa, i.e., wetland region 10 in Figure 1~~2017).

The seasonal cycles inferred from the inversion are in general consistent with prior information (Figure ~~9~~11), although averaging kernel sensitivities indicate that we only have limited constraints on the seasonality, particularly for high latitude regions in northern hemisphere winter. This was generally expected, given the limited GOSAT observational coverage at high latitudes during winter months. The inversion infers a sharp and late (May-June) onset of methane emissions across boreal wetlands, in contrast to an early and gradual increase starting from March predicted by the prior inventory. This feature in posterior estimates appears to be consistent with aircraft and surface observations over Canada's Hudson Bay Lowlands (Pickett-Heaps et al., 2011) and eddy flux measurements over Alaskan Arctic tundra (Zona et al., 2015), while the gradual onset in the prior inventory agrees with aircraft observations over Alaska by Miller et al. (2016). The negative fluxes right before the onset may reflect strong soil sinks during spring thaw over these high-latitude regions (Jørgensen et al., 2015~~);~~ ~~alternatively, given the low averaging kernel sensitivities throughout the winter season, the negative fluxes could be attributable to spatial or temporal compensating inversion errors. The inversion also suggests~~). The inversion also indicates stronger seasonal cycles than the prior inventory in Sub-Saharan Africa and tropical South Asia, which ~~indicates~~suggests that ~~the prior inventory~~WetCHARTs may ~~have underestimated~~underestimate the sensitivity of wetland emissions to precipitation but overestimate ~~the~~their sensitivity to temperature.

Our posterior estimates of 2010–2018 trends in wetland emissions vary greatly by region, and are generally larger than the prior estimates from WetCHARTs~~, indicating that they are mostly driven by the GOSAT data. They vary greatly by region~~ (Figure ~~10~~12). Large positive trends are found in the tropics (Amazon: +0.9 Tg a^{-1} a^{-1}; Sub-Sahara Africa: +0.6 Tg a^{-1} a^{-1}; southern Africa: +0.4 Tg a^{-1} a^{-1}) and high latitudes (~~Russia~~Siberia: +0.6 Tg a^{-1} a^{-1}; ~~West~~northern Europe: +0.4 Tg a^{-1} a^{-1}). Increasing Amazonian wetland emissions may have been driven by intensification of flooding (Barichivich et al., 2018) or increasing temperature (Tunnicliffe et al., 2020) in the region over the past ~~three~~ decades ~~(Barichivich et al., 2018).~~ Our result of increasing tropical Africa wetland emissions is consistent with a previous regional analysis of GOSAT data, which found a positive trend of 1.5–2.1 Tg a^{-1} a^{-1} in the region for 2010–2016 attributed mainly to wetlands particularly the Sudd in South Sudan (Lunt et al., 2019). Compared to steady and linear increases in the tropics, boreal ~~Russia~~Siberia and ~~West~~northern Europe show abrupt increases in ~~2017~~2016–2018, for reasons unclear (Figure ~~10~~12). Decreasing but weaker trends are found in tropical Southeast Asia (-0.3 Tg a^{-1} a^{-1}) and Australia (-0.2 Tg a^{-1} a^{-1}). ~~These trends are in general not captured by prior information, suggesting that our results can be useful inputs to improvement of process based wetland emission modeling. Furthermore, posterior inter annual variability is overall larger than prior variability across all regions, suggesting that the integrated climate sensitivity of prior emissions may be underestimated.~~

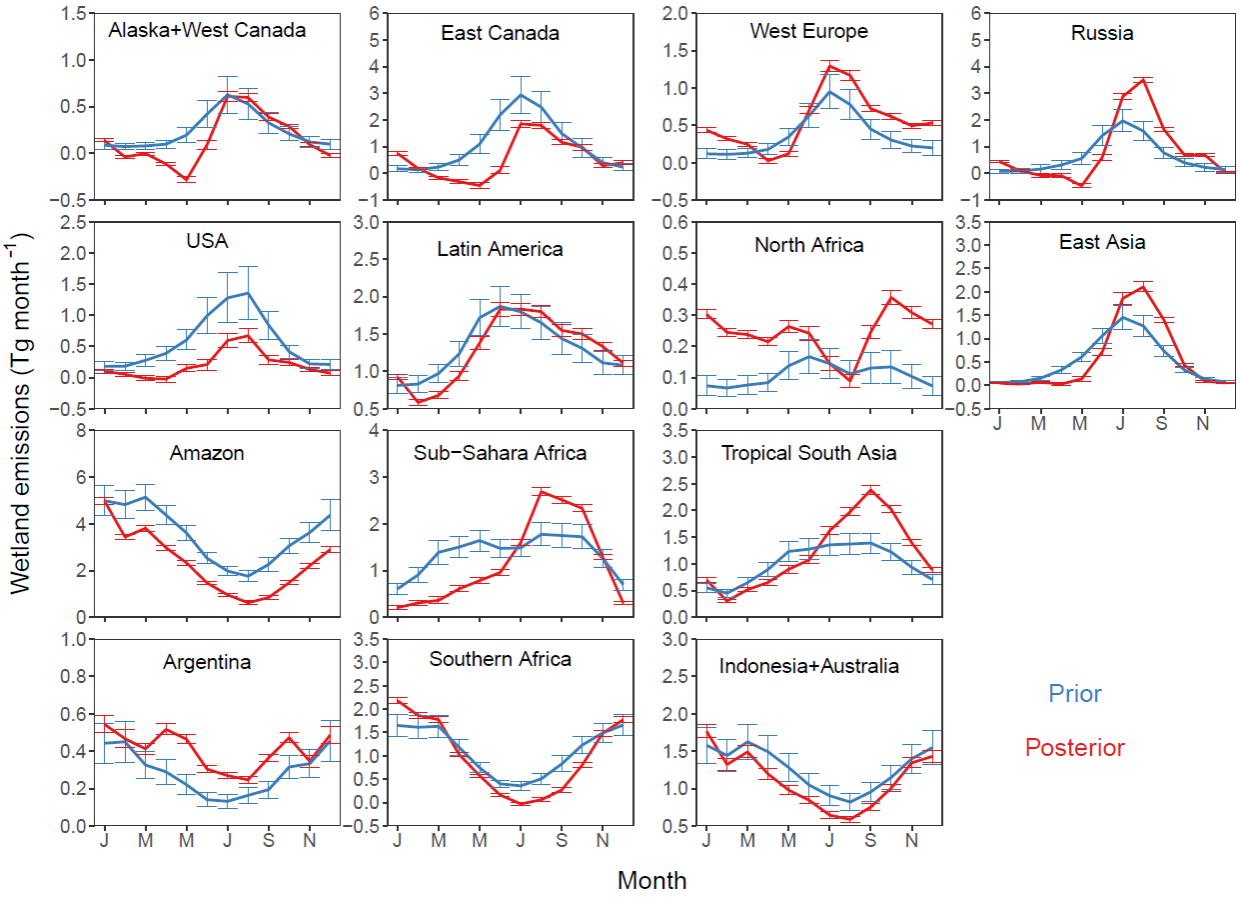
Alaska+West Canada
East Canada
West Europe
Russia
USA
Latin America
North Africa
East Asia
Amazon
Sub−Sahara Africa
Tropical South Asia
Argentina
Southern Africa
Indonesia+Australia
Wetland emissions (Tg month-1)
J M M J S N
Month
Prior
Posterior

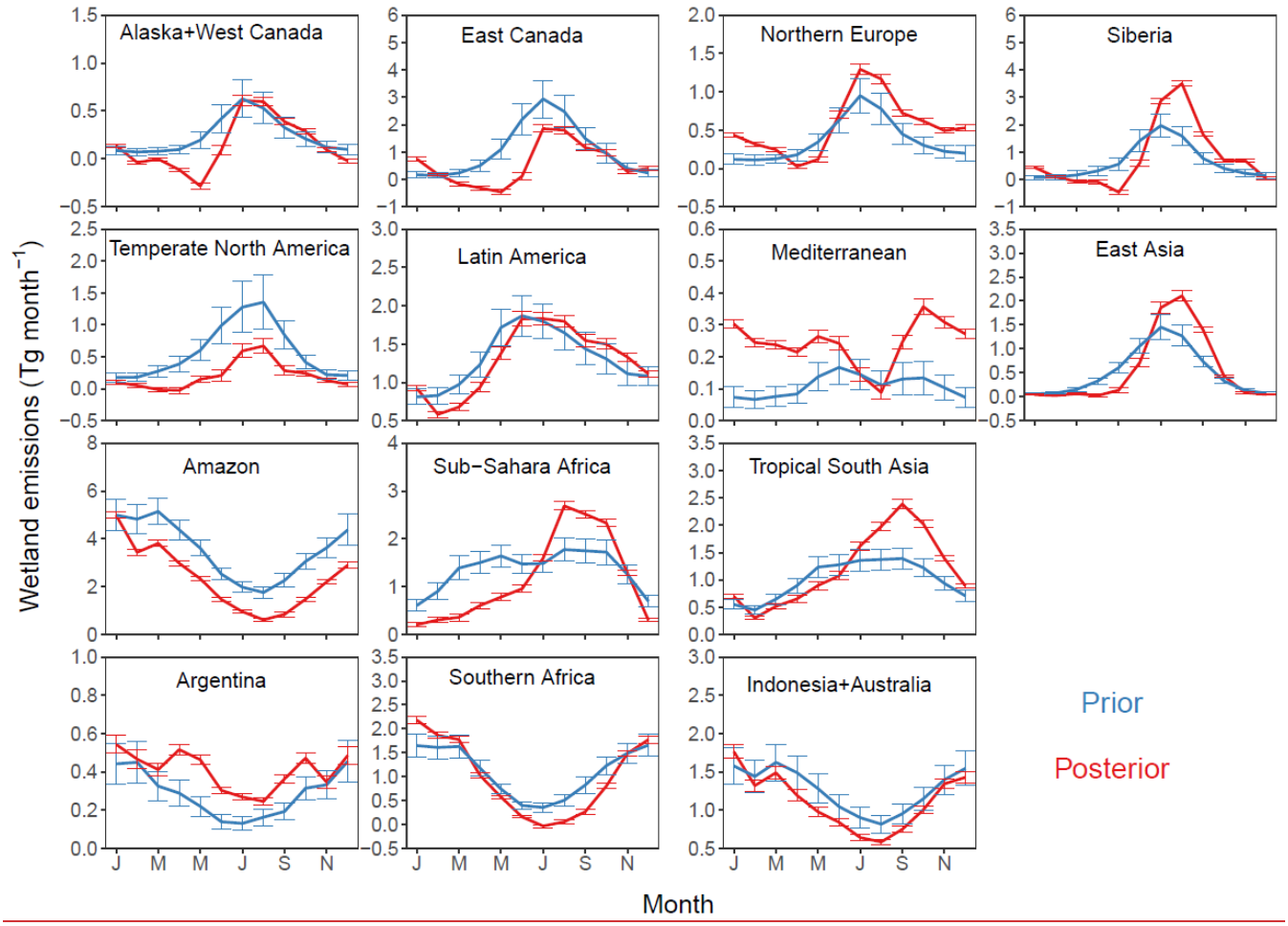

Figure 11. Seasonal variation of wetland emissions for 14 subcontinental regions (Figure 1). Values are means for 2010–2018. The prior estimate is the mean of the WetCHARTs inventory ensemble (Bloom et al., 2017). The posterior estimate is from our inversion of GOSAT data. Vertical bars are error standard deviations. The reduction of error in the posterior estimate measures the information content provided by the GOSAT data. Scales are different between panels.

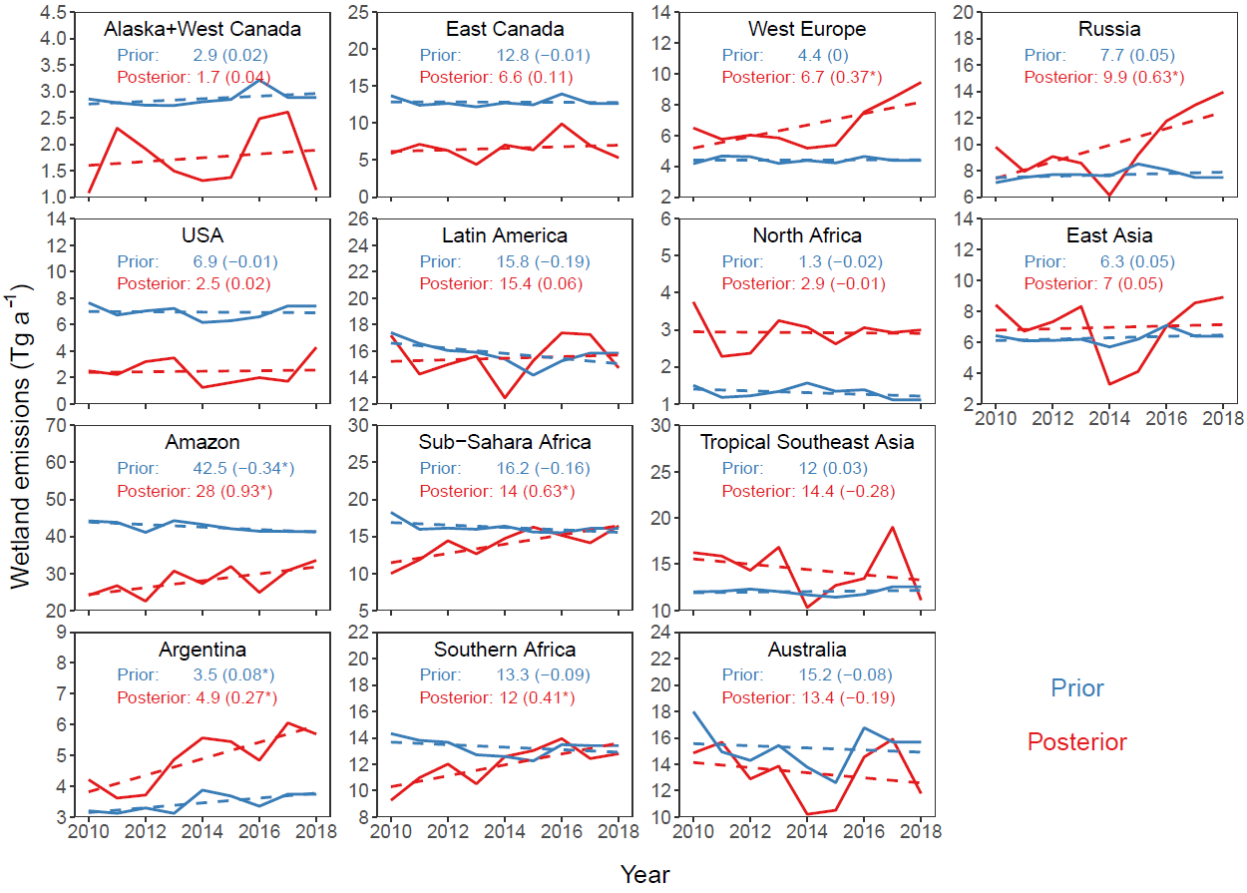
Alaska+West Canada
Prior: 2.9 (0.02)
Posterior: 1.7 (0.04)
East Canada
Prior: 12.8 (−0.01)
Posterior: 6.6 (0.11)
West Europe
Prior: 4.4 (0)
Posterior: 6.7 (0.37*)
Russia
Prior: 7.7 (0.05)
Posterior: 9.9 (0.63*)
USA
Prior: 6.9 (−0.01)
Posterior: 2.5 (0.02)
Latin America
Prior: 15.8 (−0.19)
Posterior: 15.4 (0.06)
North Africa
Prior: 1.3 (−0.02)
Posterior: 2.9 (−0.01)
East Asia
Prior: 6.3 (0.05)
Posterior: 7 (0.05)
Amazon
Prior: 42.5 (−0.34*)
Posterior: 28 (0.93*)
Sub−Sahara Africa
Prior: 16.2 (−0.16)
Posterior: 14 (0.63*)
Tropical Southeast Asia
Prior: 12 (0.03)
Posterior: 14.4 (−0.28)
Argentina
Prior: 3.5 (0.08*)
Posterior: 4.9 (0.27*)
Southern Africa
Prior: 13.3 (−0.09)
Posterior: 12 (0.41*)
Australia
Prior: 15.2 (−0.08)
Posterior: 13.4 (−0.19)
Wetland emissions (Tg a^{-1})
Year
Prior
Posterior

575

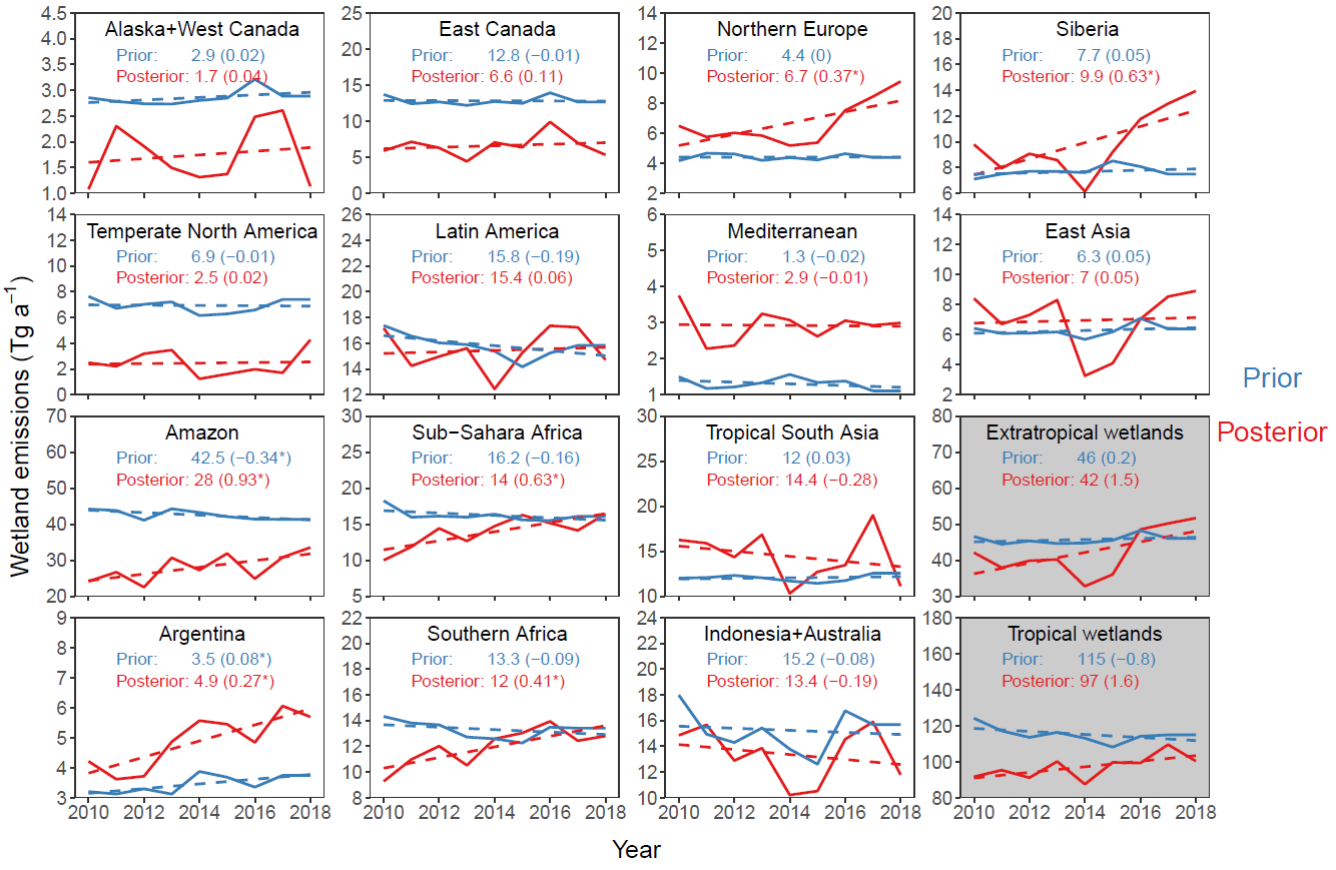

Figure 12. Wetland emission trends, 2010–2018. The figure shows annual mean emissions for the prior estimate (mean of WetCHARTs inventory ensemble) and the posterior estimate after inversion of GOSAT data. Values are for the 14 subcontinental regions of Figure 1~~.~~ (panels in white background), and also aggregated for extratropics and tropics (panels in grey background). The trends are from ~~ordinarly~~ordinary linear regression. Inset are prior and posterior 2010–2018 average annual emissions in Tg a^{-1} with 2010–2018 trends in Tg a^{-1} a^{-1} in parentheses. Significant trends at the 95% confidence level are denoted with "*". Note differences in scales between panels.

~~3~~4.4 OH concentration

Our inversion infers a global methane lifetime against oxidation by tropospheric OH of 12.4±0.3 a, which is ~~–~~15% longer than the prior estimate (10.7±1.1 a) and is at the higher end of the inference from the methyl chloroform proxy (11.2±1.3 years) (Prather et al., 2012). We find that the downward correction for OH concentrations is mainly in the northern hemisphere. The north-to-south inter-hemispheric OH ratio is 1.02±0.05 in the posterior estimate, as compared to 1.16 in the prior estimate and 1.28±0.10 in the ACCMIP model ensemble (Naik et al., 2013). It is more consistent with the observation-based estimate of 0.97~~ ± ±~~0.12 (Patra et al., 2014). No significant 2010–2018 trend is seen in the methane lifetime (Figure ~~11~~13). The OH

concentration in 2014 is 5% lower than average ~~in 2014~~, which ~~had~~may relate to particularly large peatland fires ~~in~~over Indonesia in 2014 that would be very large sources of carbon monoxide (CO) as a sink for OH (Pandey et al., 2017b).

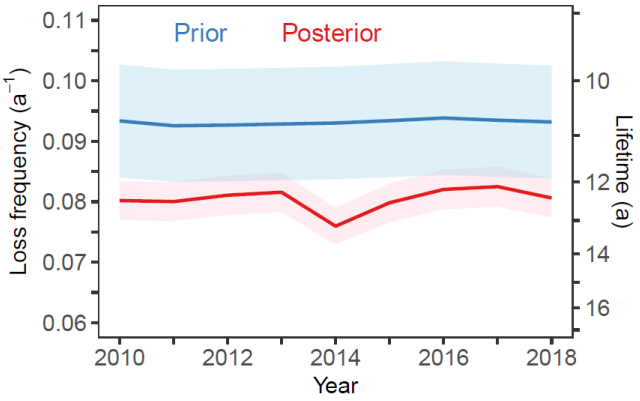

Figure 13. Methane loss frequency and lifetime against oxidation by tropospheric OH, 2010-2018. Values are annual means with error standard deviations. The loss frequency (k) is as calculated by Eq. 1 and the lifetime ($\boldsymbol{\tau}$) is the inverse. The prior estimate from Wecht et al. (2014) assumes no 2010–2018 trend in OH concentrations; the slight variability seen in the Figure is due to temperature.

~~3~~4.5 Attribution of the 2010–2018 methane trend

Figure ~~12~~14 shows the 2010–2018 annual methane growth rates inferred from NOAA background surface measurements (Dlugokencky, 2020) and from our inversion of GOSAT data. There is general consistency between the two, with both showing highest growth rates in 2014–2015 and a general acceleration after 2014. Our inversion achieves a much better match to the interannual variability ~~in~~of the NOAA record than the previous work of Maasakkers et al. (2019), in large part because of our optimization of the interannual variability of wetland emissions.

The bottom panel of Figure ~~12~~14 attributes the interannual variability in the methane growth rate to individual processes as determined by the inversion. The growth rate $G_j = [dm/dt]_j$ in year j~~,~~ (where m is the global methane mass~~,~~) is determined by the balance between sources and sinks:

$$G_j = E_j - k_j m_j - L_j \tag{9}$$

Here E_j denotes the global emission in year j, for which the inversion provides further sectoral breakdown, k_j is the loss frequency against oxidation by tropospheric OH (Eq. 1), m_j is the total methane mass, and L_j represents the minor sinks not optimized by the inversion. Let $\Delta E_j = E_j - E_o$, $\Delta k_j = k_j - k_o$, and $\Delta m_j = m_j - m_o$ represent the changes relative to 2010 conditions (E_o, k_o, m_o) taken as reference. We can then write

$$G_j = (E_o + \Delta E_j) - (k_o + \Delta k_j)(m_o + \Delta m_j) - (L_o + \Delta L_j)$$
$$\approx (E_o - k_o m_o - L_o - k_o \Delta m_j) + \Delta E_j - m_o \Delta k_j \quad (10)$$

where we have neglected the minor terms $\Delta k_j \Delta m_j$ and ΔL_j. Here the growth rate G_j in year j is decomposed into three terms: (1) a relaxation to steady state based on 2010 conditions ($E_o - k_o m_o - L_o - k_o \Delta m_j$), (2) a perturbation to emissions (ΔE_j) that can be further disaggregated by sectors, and (3) a perturbation to OH concentrations ($m_o \Delta k_j$).

We see ~~that~~ from the bottom panel of ~~Figure 12~~Figure 14 that the legacy of 2010 imbalance sustains a positive growth rate throughout the 2010–2018 period but this influence diminishes towards the end of the record. The 2010–2018 trend in anthropogenic emissions is linear by design of the inversion and sustains a steady growth rate over the 2010–2018 period as the legacy of the 2010 imbalance declines. ~~The~~Figure 15 shows the sectoral breakdown of the anthropogenic trend. The increase of global anthropogenic emissions totalling 1.4±0.8 Tg a^{-1} a^{-1} is driven by livestock (0.63±0.36 Tg a^{-1} a^{-1}; South Asia, tropical Africa, Brazil), rice (0.36±0.18 Tg a^{-1} a^{-1}; East Asia), and wastewater treatment (0.28±0.13 Tg a^{-1} a^{-1}; Asia). Our best estimate finds zero global trend in emissions from fuel exploitation (oil, gas, and coal) (0.0±0.4 Tg a^{-1} a^{-1}); but small trends cannot be ruled out given the uncertainty (Figure 15).

The bottom panel of Figure 14 also shows that the spike in the methane growth rate in 2014–2015 is attributed to an anomalously low OH concentration in 2014 (5% lower than 2010–2018 average; Figure ~~11~~13), partly offset by low wetland emissions, and anomalously high fire emissions in 2015, mostly from Indonesia peatlands (Worden et al., 2017). Smoldering peatland fires are particularly large sources of methane (Liu et al., 2020). The large fire emissions are informed by the GFED inventory because the inter-annual variability of fire emissions is not optimized in our inversion. Despite their small magnitude relative to wetland and anthropogenic emissions globally, anomalous fire emissions can be an important contributor to methane interannual variability (Worden et al., 2017;Pandey et al., 2017b), both directly by releasing methane and indirectly by decreasing OH concentrations through CO emissions. ~~Error correlations in our methane trend attributions (see discussion below) suggest that the high growth rates in both 2014 and 2015 could be due to Indonesian fires including effects on OH.~~

In addition to the 2014–2015 extremum, the NOAA surface observations show an acceleration of methane growth during the latter part of the 2010–2018 record (Nisbet et al., 2019) and this is reproduced in our inversion (Figure ~~12~~14). ~~We find that the rapid~~This accelerating growth ~~in 2016–2018~~ is ~~mostly~~ driven by ~~wetlands, including contributions from both the~~strong wetland emissions, particularly in 2016–2018, on top of increasing anthropogenic emissions (Figure 14). Our inversion infers a relatively steady 2010–2018 increase ~~in~~from tropical wetlands (in particular the Amazon and tropical Africa) and ~~the~~a 2016–2018 surge ~~in Eurasian~~ from extratropical wetlands (in particular boreal ~~wetlands (Figure 10).~~Eurasia) (Figure 12). More work is needed to understand drivers for changes in wetland emissions.

~~Figure 13 shows the mean 2010–2018 emission trends attributed by the inversion to individual sectors. The 2010–2018 growth in emissions is two-thirds from wetlands (3.0 Tg a^{-1} a^{-1}) and one third anthropogenic (1.5 Tg a^{-1} a^{-1}). Wetland emissions increase in both tropical regions (1.8±0.6 Tg a^{-1} a^{-1}; Amazon and tropical Africa) and the extra-tropics (1.2±0.3 Tg a^{-1} a^{-1}; Russia and West Europe) (Figure 13 and Figure 10). The increase of anthropogenic emissions is driven by livestock (South Asia, tropical Africa, Brazil), rice (East Asia), and wastewater treatment (Asia) sectors (Figure 13). The best estimate for global trends in emissions from fuel exploitation (oil, gas, and coal) (0.0±0.4 Tg a^{-1} a^{-1}) is almost zero; but small trends cannot be ruled out given the uncertainty (Figure 13).~~

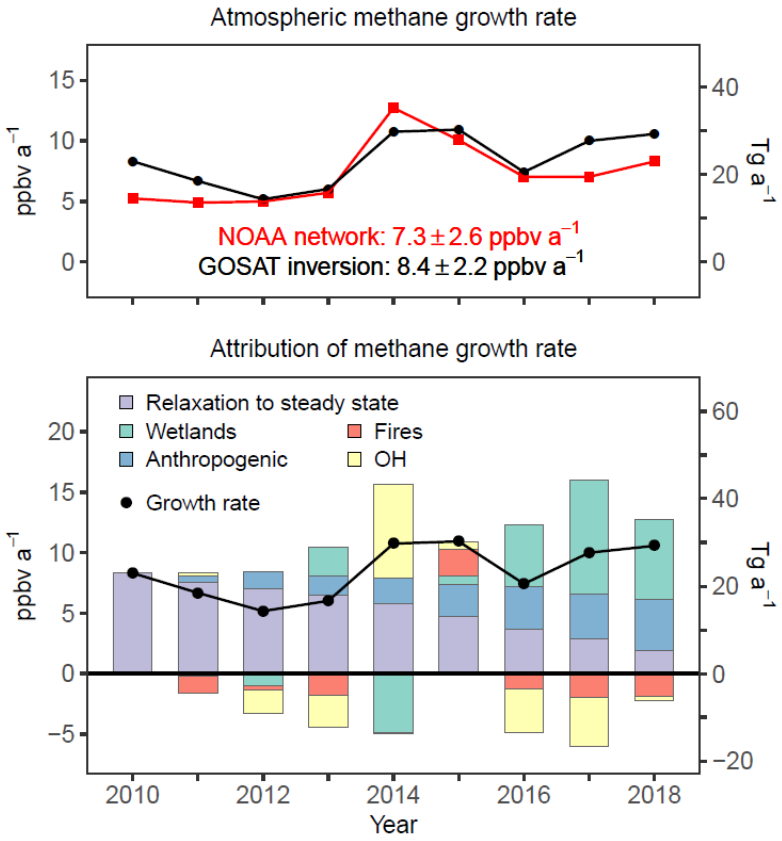

Figure 14. 2010–2018 annual growth rates in global atmospheric methane. (Top) Comparison of annual growth rates inferred from our inversion of GOSAT data and from the NOAA surface network (Dlugokencky, 2020). Average methane growth rates for the period are inset. (Bottom) Attribution of annual growth rates in the GOSAT inversion to perturbations to emissions (anthropogenic, wetlands, fires) and OH concentrations relative to 2010 conditions. The purple bar shows the relaxation of 2010 budget imbalance to steady state. See text for details explaining the breakdown.

We estimate from the inversion a global mean methane emission for 2010–2018 of 510±4 Tg a^{-1} (wetlands: 139 Tg a^{-1}; anthropogenic: 341 Tg a^{-1}) and a sink of 488±4 Tg a^{-1}. This posterior global emission is lower than the prior estimate (538 Tg a^{-1}) and the 538–593 Tg a^{-1} range reported ~~recently~~ by the Global Carbon Project for 2008–2017 (Saunois et al., 2020). Compared to prior emissions, we estimate lower emissions for wetlands and fossil fuel, and higher emissions for livestock and rice (~~Figure 13).~~Figure 12 and Figure 15). Meanwhile, we estimate a methane lifetime against tropospheric OH oxidation of 12.4±0.3 years, at the high end of 11.2±1.3 years based on the methyl chloroform proxy (Prather et al., ~~2012).~~2012), though strong error correlations between wetland emissions and methane lifetime suggests that our inversion has limited ability to constrain both independently (Figure 5).

~~Figure 14 plots the posterior joint probability density functions (PDFs) for pairs of global budget terms and their trends. There is a strong negative error correlation in the inversion results between anthropogenic emissions and methane lifetime (r= 0.8), reflecting limited ability of the inversion to separate the two. In contrast, error correlations between wetland emissions and methane lifetime (r= 0.4), and between wetland and anthropogenic emissions (r= 0.2) are much smaller. We find moderate error correlations between the OH trend and either wetland or anthropogenic emission trends (r= 0.6). We cannot exclude at the 90% confidence level the possibility that the 2010–2018 anthropogenic emission trend could be zero (compensated by a decrease in OH concentrations), but we can exclude the possibility that the 2010–2018 wetland emission trend could be zero. Improved separation of global budget terms and their trends may be achieved by including additional information from surface observation (Lu et al.,~~

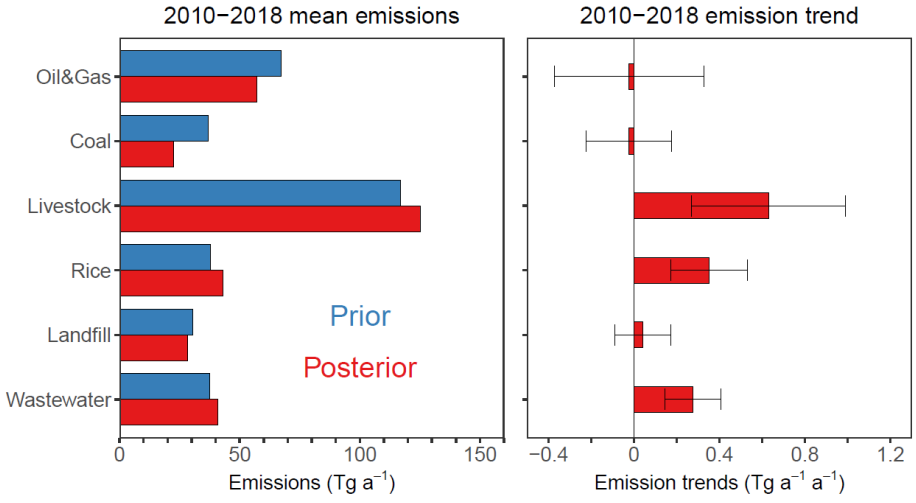

~~2020) and from thermal infrared satellite observations (Y. Zhang et al., 2018).~~

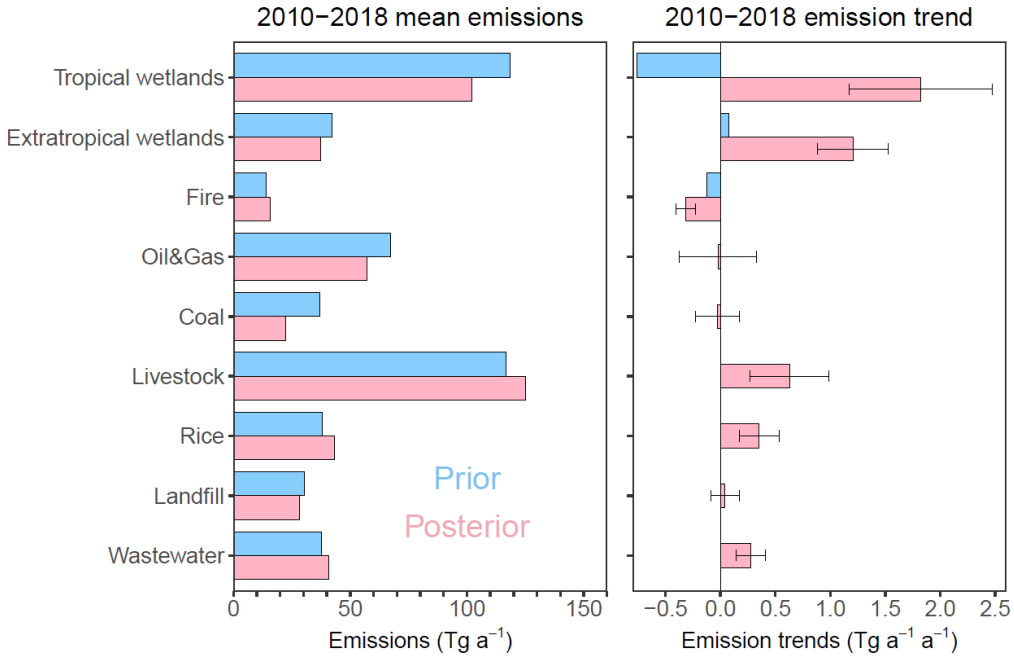

Figure 15. 2010–2018 global methane anthropogenic emissions and emission trends partitioned by individual sectors. Posterior estimates are from our inversion of GOSAT data. Prior estimates for anthropogenic emission trends are zero. Error bars in the right panel ~~shows~~show posterior error standard deviations for emission trends. Posterior error standard deviations ~~are too small to show~~ for mean emissions ~~of~~are small and are thus not shown in the left panel. ~~Posterior errors computed from Eq. 4 and 7 tend to be overoptimistic because of ideal inversion assumptions (Maasakkers et al., 2019).~~

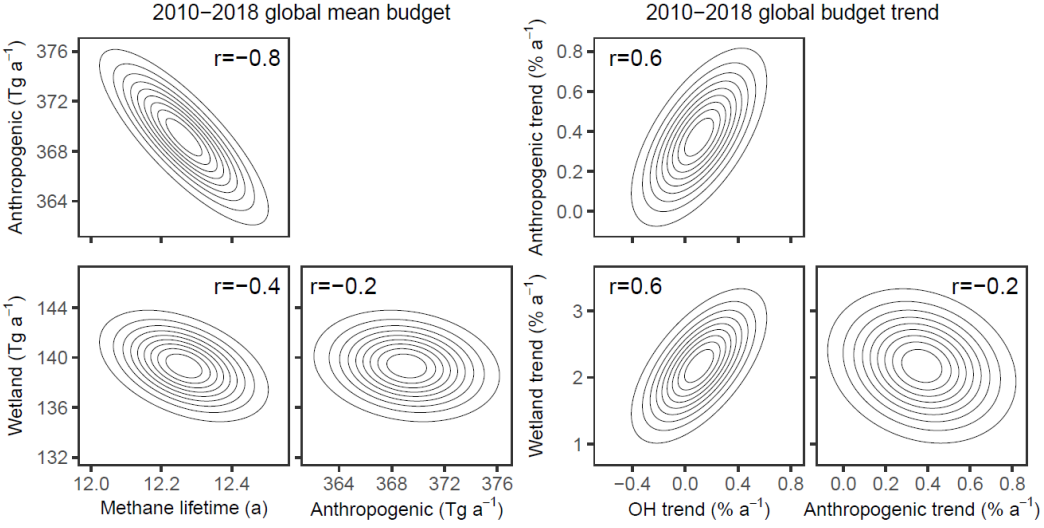

~~**Figure 14.5** Error correlations between global anthropogenic emissions, wetland emissions, and tropospheric OH concentrations (methane lifetime against oxidation by tropospheric OH; τ) in the inverse solution. Results are shown both for 2010–2018 mean values and for 2010–~~

2018 trends. The error correlations are presented as joint probability density functions for pairs of reduced global state vector elements. Confidence ellipses represent probability of 0.1 (innermost) to 0.9 (outermost) at intervals of 0.1. The error correlation coefficients are shown inset.

4 Conclusions

We quantified the regional and sectoral contributions to global atmospheric methane and its 2010–2018 trend by inversion of GOSAT satellite observations. The inversion jointly optimizes (1) 2010–2018 anthropogenic emissions and their linear trends on a 4º×5 º grid; (2) monthly wetland emissions in 14 subcontinental regions for individual yearsmonths; and (3) annual mean hemispheric OH concentrations for individual years. Analytical solution to the optimization problem provides closed-form estimates of posterior error covariances and information content, allowing us in particular to diagnose error correlations in our solution. Separate optimization of wetland and anthropogenic emissions allows us to resolve interannual and seasonal variations in posterior wetland emissions. Our inversion introduces additional innovations including the correction of stratospheric model biases using ACE-FTS satellite data, and a new bottom-up inventory for emissions from fossil fuel exploitation based on national reports to the UNFCCC (Scarpelli et al., 2020).

Our optimization of 2010–2018 mean anthropogenic emissions on the 4º×5 º grid provides strong information in source regions as measured by averaging kernel sensitivities. We find that estimates of anthropogenic emissions reported by individual countries to the UNFCCC are too high for China (coal emissions) and Russia (oil/gas emissions) and too low for Venezuela (oil/gas) and the U.S. (oil/gas). We also find that tropical livestock emissions are larger than previous estimates particularly in South Asia, Africa, and Brazil. Our posterior estimate of anthropogenic emissions in India (33 Tg a^{-1}) is much higher than its most recent (2010) report to the UNFCCC (20 Tg a^{-1}), mostly because of livestock emissions.

2010–2018 trends in methane emissions on the 4º×5 º grid are successfully quantified in source regions. We find that the largest growth in anthropogenic emissions is fromoccurs in tropical livestock inregions including South Asia, tropical Africa, and Brazil, and can be attributed to the livestock sector. This finding is consistent with trends in livestock populations. There has been little discussion in the literature about increasing agricultural methane emissions in these developing countries (Jackson et al., 2020). TheOur results also show that the 2010–2018 increase in Chinese emissions is smaller than previously reported in inversions focused on earlier periods, likely caused by leveling of coal emissions in China. The 2010–2018 emission trend in the USU.S. is insignificant on the national scale.

We find that global wetland emissions are lower than the prior estimate from mean WetCHARTs emissions used as prior estimate, mostly because of the Amazon. Wetland emissions over North America are also lower, consistent with previous studies. In both cases, we note that posterior estimates are all well within the full WetCHARTs uncertainty range (Bloom et

al., 2017). The seasonality of wetland emissions inferred by the inversion is in general consistent with WetCHARTs. An exception is in boreal wetlands where we find negative fluxes in April-May, possibly reflecting methane uptake as the soil thaws. The inversion infers increasing wetland emissions over the 2010–2018 period, superimposed on large inter-annual variability, in both the tropics (Amazon, tropical Africa) and extra-tropics (~~Russia, western~~Siberia, northern Europe).

Our optimization of annual hemispheric OH concentrations yields a global methane lifetime of 12.4±0.3 years against oxidation by tropospheric OH, with an inter-hemispheric OH ratio of 1.02. Our best estimate is that the global OH concentration has no significant trend over 2010–2018 except for a 5% dip in 2014.

Taking all these methane budget terms together, our inversion of GOSAT satellite data estimates global mean methane emissions for 2010–2018 of 510 Tg a^{-1}, with 341 Tg a^{-1} from anthropogenic sources, 139 Tg a^{-1} from wetland sources, and 30 Tg a^{-1} from other natural sources. Our inferred growth rate of methane over that period matches that observed at NOAA background sites, including peak growth rates in 2014–2015 and an overall acceleration over the 2010–2018 period. We attribute the 2014–2015 peaks in methane growth rates to low OH concentrations (2014) and high fire emissions (2015), and the overall ~~trend~~ acceleration to a sustained increase in anthropogenic emissions~~.~~ over the period and strong wetland emissions in the latter part of the period. Most of ~~this~~the increase in anthropogenic emissions is attributed to ~~wetlands (tropics: 1.8 Tg a^{-1} a^{-1}; extra-tropics: 1.2 Tg a^{-1} a^{-1}) and tropical~~ livestock (~~0.8 Tg a^{-1} a^{-1}).~~in tropics), with minor contributions from increases in rice and wastewater emissions (Asia). Our best estimate indicates ~~no~~insignificant contribution of the ~~oil/gas~~fuel exploitation sector to increasing global emissions~~, but small oil/gas trends cannot be ruled out given relatively large uncertainties~~. Our finding is in general consistent with a previous 2010–2015 inversion of GOSAT data (Maasakkers et al., 2019) although here we use a longer record and we capture the interannual variability better. Our results also agree with isotopic data indicating that the rise in methane is driven by biogenic sources (Schaefer et al., 2016;Nisbet et al., 2016). The increase in tropical livestock emissions is quantitatively consistent with bottom-up estimates. More work is needed to understand ~~the increase~~interannual variations in wetland emissions.

Data availability

The dataset for the 2010–2018 global inversion results is accessible through doi.org/10.5281/zenodo.4052518. The GOSAT proxy satellite methane observations are available at the CEDA archive (Parker and Boesch, 2020). The ACE-FTS satellite observations can be requested through http://www.ace.uwaterloo.ca/data.php (last access: July 20, 2020). TCCON data were obtained from the TCCON Data Archive hosted by CaltechDATA (https://tccondata.org) (Deutscher et al., 2017; Dubey et al., 2017; Feist et al., 2017; Goo et al., 2017; Griffith et al., 2017a, b; Hase et al., 2017; Iraci et al., 2017a, b; Kivi et al., 2017; Liu et al., 2017; de Maziere et al., 2017; Morino et al., 2017a, b, c; Notholt et al., 2019a, b; Sherlock et al., 2017a, b; Shiomi et al., 2017; Strong et al., 2017; Sussmann et al., 2017; Te et al., 2017; Warneke et al., 2017; Wennberg et al., 2017a, b, c, d; Wunch

et al., 2017). NOAA surface observations are accessed through NOAA ESRL/GMD CCGG Group (doi.org/10.15138/VNCZ-M766) (Dlugokencky et al., 2020). National reports to UNFCCC are available through UNFCCC's Greenhouse Gas Inventory Data Interface (di.unfccc.int/detailed_data_by_party, last access: July 20, 2020). EDGAR anthropogenic emission inventories (v4.3.2 and v5) are available at https://data.europa.eu/doi/10.2904/JRC_DATASET_EDGAR (last access: July 20, 2020).

Author contributions

YZ and DJJ designed the study. YZ conducted the modeling and data analyses with contributions from XL, JDM, TRS, MPS, JXS, LS, ZQ. RJP and HB provided the GOSAT satellite methane retrievals. AAB and SM contributed to the WetCHARTs wetland emission inventory and its interpretation. JFC contributed to analyses and interpretation of bottom-up livestock emission inventories. YZ and DJJ wrote the paper with inputs from all authors.

Competing interests

The authors declare that they have no conflict of interest.

Acknowledgments

Work at Harvard was supported by the NASA Carbon Monitoring System (CMS), Interdisciplinary Science (IDS), and Advanced Information Systems Technology (AIST) programs. YZ was supported by ~~the foundation of Westlake~~Harvard University, the Kravis Fellowship through the Environmental Defense Fund (EDF), the National Natural Science Foundation of China (Project: 42007198), and ~~Harvard~~the foundation of Westlake University. YZ thanks Peter Bernath and Chris Boone for discussion on the ACE-FTS data and Benjamin Poulter for discussion on attribution of the atmospheric methane trend. Part of this research was carried out at the Jet Propulsion Laboratory, California Institute of Technology, under a contract with NASA. RJP and HB are funded via the UK National Centre for Earth Observation (NE/R016518/1 and NE/N018079/1). RJP and HB also acknowledge funding from the ESA GHG-CCI and Copernicus C3S projects. We thank the Japanese Aerospace Exploration Agency, National Institute for Environmental Studies, and the Ministry of Environment for the GOSAT data and their continuous support as part of the Joint Research Agreement. GOSAT retrievals were performed with the ALICE High Performance Computing Facility at the University of Leicester.

References

Alexe, M., Bergamaschi, P., Segers, A., Detmers, R., Butz, A., Hasekamp, O., Guerlet, S., Parker, R., Boesch, H., Frankenberg, C., Scheepmaker, R. A., Dlugokencky, E., Sweeney, C., Wofsy, S. C., and Kort, E. A.: Inverse modelling of CH_4 emissions

for 2010–2011 using different satellite retrieval products from GOSAT and SCIAMACHY, Atmos. Chem. Phys., 15, 113-133, 10.5194/acp-15-113-2015, 2015.

Alvarez, R. A., Zavala-Araiza, D., Lyon, D. R., Allen, D. T., Barkley, Z. R., Brandt, A. R., Davis, K. J., Herndon, S. C., Jacob, D. J., Karion, A., Kort, E. A., Lamb, B. K., Lauvaux, T., Maasakkers, J. D., Marchese, A. J., Omara, M., Pacala, S. W., Peischl, J., Robinson, A. L., Shepson, P. B., Sweeney, C., Townsend-Small, A., Wofsy, S. C., and Hamburg, S. P.: Assessment of methane emissions from the U.S. oil and gas supply chain, Science, 361, 186-188, 10.1126/science.aar7204, 2018.

Baray, S., Maasakkers, J. D., Sulprizio, M. P., Sheng, J.-X., Jacob, D., Jones, D. B. A., Worthy, D., and McLaren, R.: Estimating Anthropogenic and Natural Methane Emissions in Canada using Surface and GOSAT Satellite Observations, AGU Fall Meeting San Franscisco, 2019.

Barichivich, J., Gloor, E., Peylin, P., Brienen, R. J. W., Schöngart, J., Espinoza, J. C., and Pattnayak, K. C.: Recent intensification of Amazon flooding extremes driven by strengthened Walker circulation, Science Advances, 4, eaat8785, 10.1126/sciadv.aat8785, 2018.

Bergamaschi, P., Houweling, S., Segers, A., Krol, M., Frankenberg, C., Scheepmaker, R. A., Dlugokencky, E., Wofsy, S. C., Kort, E. A., Sweeney, C., Schuck, T., Brenninkmeijer, C., Chen, H., Beck, V., and Gerbig, C.: Atmospheric CH_4 in the first decade of the 21st century: Inverse modeling analysis using SCIAMACHY satellite retrievals and NOAA surface measurements, Journal of Geophysical Research: Atmospheres, 118, 7350-7369, 10.1002/jgrd.50480, 2013.

Bernath, P. F., McElroy, C. T., Abrams, M. C., Boone, C. D., Butler, M., Camy-Peyret, C., Carleer, M., Clerbaux, C., Coheur, P.-F., Colin, R., DeCola, P., DeMazière, M., Drummond, J. R., Dufour, D., Evans, W. F. J., Fast, H., Fussen, D., Gilbert, K., Jennings, D. E., Llewellyn, E. J., Lowe, R. P., Mahieu, E., McConnell, J. C., McHugh, M., McLeod, S. D., Michaud, R., Midwinter, C., Nassar, R., Nichitiu, F., Nowlan, C., Rinsland, C. P., Rochon, Y. J., Rowlands, N., Semeniuk, K., Simon, P., Skelton, R., Sloan, J. J., Soucy, M.-A., Strong, K., Tremblay, P., Turnbull, D., Walker, K. A., Walkty, I., Wardle, D. A., Wehrle, V., Zander, R., and Zou, J.: Atmospheric Chemistry Experiment (ACE): Mission overview, Geophysical Research Letters, 32, 10.1029/2005gl022386, 2005.

Bloom, A. A., Bowman, K. W., Lee, M., Turner, A. J., Schroeder, R., Worden, J. R., Weidner, R., McDonald, K. C., and Jacob, D. J.: A global wetland methane emissions and uncertainty dataset for atmospheric chemical transport models (WetCHARTs version 1.0), Geosci. Model Dev., 10, 2141-2156, 10.5194/gmd-10-2141-2017, 2017.

Bousquet, P., Hauglustaine, D. A., Peylin, P., Carouge, C., and Ciais, P.: Two decades of OH variability as inferred by an inversion of atmospheric transport and chemistry of methyl chloroform, Atmos. Chem. Phys., 5, 2635-2656, 10.5194/acp-5-2635-2005, 2005.

Brasseur, G. P., and Jacob, D. J.: Modeling of Atmospheric Chemistry, Cambridge University Press, Cambridge, 2017.

Bruhwiler, L. M., Basu, S., Bergamaschi, P., Bousquet, P., Dlugokencky, E., Houweling, S., Ishizawa, M., Kim, H.-S., Locatelli, R., Maksyutov, S., Montzka, S., Pandey, S., Patra, P. K., Petron, G., Saunois, M., Sweeney, C., Schwietzke, S.,

Tans, P., and Weatherhead, E. C.: U.S. CH_4 emissions from oil and gas production: Have recent large increases been detected?, Journal of Geophysical Research: Atmospheres, 122, 4070-4083, 10.1002/2016jd026157, 2017.

Buchwitz, M., Reuter, M., Schneising, O., Boesch, H., Guerlet, S., Dils, B., Aben, I., Armante, R., Bergamaschi, P., Blumenstock, T., Bovensmann, H., Brunner, D., Buchmann, B., Burrows, J. P., Butz, A., Chédin, A., Chevallier, F., Crevoisier, C. D., Deutscher, N. M., Frankenberg, C., Hase, F., Hasekamp, O. P., Heymann, J., Kaminski, T., Laeng, A., Lichtenberg, G., De Mazière, M., Noël, S., Notholt, J., Orphal, J., Popp, C., Parker, R., Scholze, M., Sussmann, R., Stiller, G. P., Warneke, T., Zehner, C., Bril, A., Crisp, D., Griffith, D. W. T., Kuze, A., O'Dell, C., Oshchepkov, S., Sherlock, V., Suto, H., Wennberg, P., Wunch, D., Yokota, T., and Yoshida, Y.: The Greenhouse Gas Climate Change Initiative (GHG-CCI): Comparison and quality assessment of near-surface-sensitive satellite-derived CO_2 and CH_4 global data sets, Remote Sensing of Environment, 162, 344-362, https://doi.org/10.1016/j.rse.2013.04.024, 2015.

Buchwitz, M., Schneising, O., Reuter, M., Heymann, J., Krautwurst, S., Bovensmann, H., Burrows, J. P., Boesch, H., Parker, R. J., Somkuti, P., Detmers, R. G., Hasekamp, O. P., Aben, I., Butz, A., Frankenberg, C., and Turner, A. J.: Satellite-derived methane hotspot emission estimates using a fast data-driven method, Atmos. Chem. Phys., 17, 5751-5774, 10.5194/acp-17-5751-2017, 2017.

Burkholder, J. B., Sander, S. P., Abbatt, J., Barker, J. R., Huie, R. E., Kolb, C. E., Kurylo, M. J., Orkin, V. L., Wilmouth, D. M., and Wine, P. H.: Chemical Kinetics and Photochemical Data for Use in Atmospheric Studies, Evaluation No. 18, Jet Propulsion Laboratory, Pasadena, 2015.

Butchart, N., and Remsberg, E. E.: The Area of the Stratospheric Polar Vortex as a Diagnostic for Tracer Transport on an Isentropic Surface, Journal of the Atmospheric Sciences, 43, 1319-1339, 10.1175/1520-0469(1986)043<1319:Taotsp>2.0.Co;2, 1986.

Chang, J., Peng, S., Ciais, P., Saunois, M., Dangal, S. R. S., Herrero, M., Havlík, P., Tian, H., and Bousquet, P.: Revisiting enteric methane emissions from domestic ruminants and their $\delta^{13}C_{CH4}$ source signature, Nature Communications, 10, 3420, 10.1038/s41467-019-11066-3, 2019.

Cressot, C., Chevallier, F., Bousquet, P., Crevoisier, C., Dlugokencky, E. J., Fortems-Cheiney, A., Frankenberg, C., Parker, R., Pison, I., Scheepmaker, R. A., Montzka, S. A., Krummel, P. B., Steele, L. P., and Langenfelds, R. L.: On the consistency between global and regional methane emissions inferred from SCIAMACHY, TANSO-FTS, IASI and surface measurements, Atmos. Chem. Phys., 14, 577-592, 10.5194/acp-14-577-2014, 2014.

Crippa, M., Oreggioni, G., Guizzardi, D., Muntean, M., Schaaf, E., Lo Vullo, E., Solazzo, E., Monforti-Ferrario, F., Olivier, J.G.J., Vignati, E.: Fossil CO_2 and GHG emissions of all world countries - 2019 Report, EUR 29849 EN, Publications Office of the European Union, Luxembourg, ISBN 978-92-76-11100-9, 10.2760/687800, 2019.

~~Cui, Y. Y., Henze, D. K., Brioude, J., Angevine, W. M., Liu, Z., Bousserez, N., Guerrette, J., McKeen, S. A., Peischl, J., Yuan, B., Ryerson, T., Frost, G., and Trainer, M.: Inversion Estimates of Lognormally Distributed Methane Emission Rates From the Haynesville-Bossier Oil and Gas Production Region Using Airborne Measurements, Journal of Geophysical Research: Atmospheres, 124, 3520-3531, 10.1029/2018jd029489, 2019.~~

Deutscher, N. M., Notholt, J., Messerschmidt, J., Weinzierl, C., Warneke, T., Petri, C., Grupe, P., and Katrynski, K.: TCCON data from Bialystok, Poland, Release GGG2014R2. TCCON data archive, hosted by CaltechDATA, http://doi.org/10.14291/tccon.ggg2014.bialystok01.R2, 2017.

Dlugokencky, E. J., NOAA/GML: Trends in Atmospheric Methane: https://www.esrl.noaa.gov/gmd/ccgg/trends_ch4/, access: June 22, 2020.

Dlugokencky, E. J., Crotwell, A. M., Mund, J. W., Crotwell, M. J., and Thoning, K. W.: Atmospheric Methane Dry Air Mole Fractions from the NOAA GML Carbon Cycle Cooperative Global Air Sampling Network, Version: 2020-07, https://doi.org/10.15138/VNCZ-M766, 2020.

Dubey, M., Henderson, B., Green, D., Butterfield, Z., Keppel-Aleks, G., Allen, N., Blavier, J. F., Roehl, C., Wunch, D., and Lindenmaier, R.: TCCON data from Manaus, Brazil, Release GGG2014R0. TCCON data archive, hosted by CaltechDATA, https://doi.org/10.14291/tccon.ggg2014.manaus01.R0/1149274, 2017.

Engel, A., Bönisch, H., Brunner, D., Fischer, H., Franke, H., Günther, G., Gurk, C., Hegglin, M., Hoor, P., Königstedt, R., Krebsbach, M., Maser, R., Parchatka, U., Peter, T., Schell, D., Schiller, C., Schmidt, U., Spelten, N., Szabo, T., Weers, U., Wernli, H., Wetter, T., and Wirth, V.: Highly resolved observations of trace gases in the lowermost stratosphere and upper troposphere from the Spurt project: an overview, Atmos. Chem. Phys., 6, 283-301, 10.5194/acp-6-283-2006, 2006.

Etiope, G., Ciotoli, G., Schwietzke, S., and Schoell, M.: Gridded maps of geological methane emissions and their isotopic signature, Earth Syst. Sci. Data, 11, 1-22, 10.5194/essd-11-1-2019, 2019.

FAOSTAT Online Statistical Service (Food and Agriculture Organization; FAO): http://faostat3.fao.org, access: Jan 20, 2020.

Feist, D. G., Arnold, S. G., John, N., and Geibel, M. C.: TCCON data from Ascension Island, Saint Helena, Ascension and Tristan da Cunha, Release GGG2014R0. TCCON data archive, hosted by CaltechDATA, http://doi.org/10.14291/tccon.ggg2014.ascension01.R0/1149285, 2017.

Franco, B., Mahieu, E., Emmons, L. K., Tzompa-Sosa, Z. A., Fischer, E. V., Sudo, K., Bovy, B., Conway, S., Griffin, D., Hannigan, J. W., Strong, K., and Walker, K. A.: Evaluating ethane and methane emissions associated with the development of oil and natural gas extraction in North America, Environmental Research Letters, 11, 044010, 10.1088/1748-9326/11/4/044010, 2016.

Fraser, A., Palmer, P. I., Feng, L., Boesch, H., Cogan, A., Parker, R., Dlugokencky, E. J., Fraser, P. J., Krummel, P. B., Langenfelds, R. L., O'Doherty, S., Prinn, R. G., Steele, L. P., van der Schoot, M., and Weiss, R. F.: Estimating regional methane surface fluxes: the relative importance of surface and GOSAT mole fraction measurements, Atmos. Chem. Phys., 13, 5697-5713, 10.5194/acp-13-5697-2013, 2013.

Fung, I., John, J., Lerner, J., Matthews, E., Prather, M., Steele, L. P., and Fraser, P. J.: Three-dimensional model synthesis of the global methane cycle, Journal of Geophysical Research: Atmospheres, 96, 13033-13065, 10.1029/91jd01247, 1991.

Ganesan, A. L., Rigby, M., Lunt, M. F., Parker, R. J., Boesch, H., Goulding, N., Umezawa, T., Zahn, A., Chatterjee, A., Prinn, R. G., Tiwari, Y. K., van der Schoot, M., and Krummel, P. B.: Atmospheric observations show accurate reporting and little growth in India's methane emissions, Nature Communications, 8, 836, 10.1038/s41467-017-00994-7, 2017.

Gelaro, R., McCarty, W., Suárez, M. J., Todling, R., Molod, A., Takacs, L., Randles, C. A., Darmenov, A., Bosilovich, M. G., Reichle, R., Wargan, K., Coy, L., Cullather, R., Draper, C., Akella, S., Buchard, V., Conaty, A., Silva, A. M. d., Gu, W., Kim, G.-K., Koster, R., Lucchesi, R., Merkova, D., Nielsen, J. E., Partyka, G., Pawson, S., Putman, W., Rienecker, M., Schubert, S. D., Sienkiewicz, M., and Zhao, B.: The Modern-Era Retrospective Analysis for Research and Applications, Version 2 (MERRA-2), Journal of Climate, 30, 5419-5454, 10.1175/jcli-d-16-0758.1, 2017.

Goo, T. Y., Oh, Y. S., and Velazco, V. A.: TCCON data from Anmyeondo, South Korea, Release GGG2014R0. TCCON data archive, hosted by CaltechDATA, https://doi.org/10.14291/tccon.ggg2014.anmeyondo01.R0/1149284, 2017.

Gorchov Negron, A. M., Kort, E. A., Conley, S. A., and Smith, M. L.: Airborne Assessment of Methane Emissions from Offshore Platforms in the U.S. Gulf of Mexico, Environmental Science & Technology, 54, 5112-5120, 10.1021/acs.est.0c00179, 2020.

Griffith, D. W. T., Deutscher, N. M., Velazco, V. A., Wennberg, P. O., Yavin, Y., Keppel-Aleks, G., Washenfelder, R. a., Toon, G. C., Blavier, J. F., Murphy, C., Jones, N., Kettlewell, G., Connor, B. J., Macatangay, R., Roehl, C., Ryczek, M., Glowacki, J., Culgan, T., and Bryant, G.: TCCON data from Darwin, Australia, Release GGG2014R0. TCCON data archive, hosted by CaltechDATA, http://doi.org/10.14291/tccon.ggg2014.darwin01.R0/1149290, 2017a.

Griffith, D. W. T., Velazco, V. A., Deutscher, N. M., Murphy, C., Jones, N., Wilson, S., Macatangay, R., Kettlewell, G., Buchholz, R. R., and Riggenbach, M.: TCCON data from Wollongong, Australia, Release GGG2014R0. TCCON data archive, hosted by CaltechDATA, https://doi.org/10.14291/tccon.ggg2014.wollongong01.R0/1149291, 2017b.

Gromov, S., Brenninkmeijer, C. A. M., and Jöckel, P.: A very limited role of tropospheric chlorine as a sink of the greenhouse gas methane, Atmos. Chem. Phys., 18, 9831-9843, 10.5194/acp-18-9831-2018, 2018.

Hase, F., Blumenstock, T., Dohe, S., Gross, J., and Kiel, M.: TCCON data from Karlsruhe, Germany, Release GGG2014R1. TCCON data archive, hosted by CaltechDATA, https://doi.org/10.14291/tccon.ggg2014.karlsruhe01.R1/1182416, 2017.

Hausmann, P., Sussmann, R., and Smale, D.: Contribution of oil and natural gas production to renewed increase in atmospheric methane (2007–2014): top–down estimate from ethane and methane column observations, Atmos. Chem. Phys., 16, 3227-3244, 10.5194/acp-16-3227-2016, 2016.

Heald, C. L., Jacob, D. J., Jones, D. B. A., Palmer, P. I., Logan, J. A., Streets, D. G., Sachse, G. W., Gille, J. C., Hoffman, R. N., and Nehrkorn, T.: Comparative inverse analysis of satellite (MOPITT) and aircraft (TRACE-P) observations to estimate Asian sources of carbon monoxide, Journal of Geophysical Research: Atmospheres, 109, D23306, 10.1029/2004JD005185, 2004.

Hegglin, M. I., Brunner, D., Peter, T., Hoor, P., Fischer, H., Staehelin, J., Krebsbach, M., Schiller, C., Parchatka, U., and Weers, U.: Measurements of NO, NO_y, N_2O, and O_3 during SPURT: implications for transport and chemistry in the lowermost stratosphere, Atmos. Chem. Phys., 6, 1331-1350, 10.5194/acp-6-1331-2006, 2006.

Helmig, D., Rossabi, S., Hueber, J., Tans, P., Montzka, S. A., Masarie, K., Thoning, K., Plass-Duelmer, C., Claude, A., Carpenter, L. J., Lewis, A. C., Punjabi, S., Reimann, S., Vollmer, M. K., Steinbrecher, R., Hannigan, J. W., Emmons, L.

K., Mahieu, E., Franco, B., Smale, D., and Pozzer, A.: Reversal of global atmospheric ethane and propane trends largely due to US oil and natural gas production, Nature Geoscience, 9, 490-495, 10.1038/ngeo2721, 2016.

Herrero, M., Havlík, P., Valin, H., Notenbaert, A., Rufino, M. C., Thornton, P. K., Blümmel, M., Weiss, F., Grace, D., and Obersteiner, M.: Biomass use, production, feed efficiencies, and greenhouse gas emissions from global livestock systems, Proceedings of the National Academy of Sciences, 110, 20888-20893, 10.1073/pnas.1308149110, 2013.

Hmiel, B., Petrenko, V. V., Dyonisius, M. N., Buizert, C., Smith, A. M., Place, P. F., Harth, C., Beaudette, R., Hua, Q., Yang, B., Vimont, I., Michel, S. E., Severinghaus, J. P., Etheridge, D., Bromley, T., Schmitt, J., Faïn, X., Weiss, R. F., and Dlugokencky, E.: Preindustrial 14CH4 indicates greater anthropogenic fossil CH_4 emissions, Nature, 578, 409-412, 10.1038/s41586-020-1991-8, 2020.

Iraci, L. T., Podolske, J., Hillyard, P. W., Roehl, C., Wennberg, P. O., Blavier, J. F., Landeros, J., Allen, N., Wunch, D., Zavaleta, J., Quigley, E., Osterman, G. B., Albertson, R., Dunwoody, K., and Boyden, H.: TCCON data from Armstrong Flight Research Center, Edwards, CA, USA, Release GGG2014R1. TCCON data archive, hosted by CaltechDATA, https://doi.org/10.14291/tccon.ggg2014.edwards01.R1/1255068, 2017a.

Iraci, L., Podolske, J., Hillyard, P., Roehl, C., Wennberg, P. O., Blavier, J. F., Landeros, J., Allen, N., Wunch, D., Zavaleta, J., Quigley, E., Osterman, G. B., Barrow, E., and Barney, J.: TCCON data from Indianapolis, Indiana, USA, Release GGG2014R1. TCCON data archive, hosted by CaltechDATA, https://doi.org/10.14291/tccon.ggg2014.indianapolis01.R1/1330094, 2017b.

Jackson, R. B., Saunois, M., Bousquet, P., Canadell, J. G., Poulter, B., Stavert, A. R., Bergamaschi, P., Niwa, Y., Segers, A., and Tsuruta, A.: Increasing anthropogenic methane emissions arise equally from agricultural and fossil fuel sources, Environmental Research Letters, 15, 071002, 10.1088/1748-9326/ab9ed2, 2020.

Janardanan, R., Maksyutov, S., Tsuruta, A., Wang, F., Tiwari, Y. K., Valsala, V., Ito, A., Yoshida, Y., Kaiser, J. W., Janssens-Maenhout, G., Arshinov, M., Sasakawa, M., Tohjima, Y., Worthy, D. E. J., Dlugokencky, E. J., Ramonet, M., Arduini, J., Lavric, J. V., Piacentino, S., Krummel, P. B., Langenfelds, R. L., Mammarella, I., and Matsunaga, T.: Country-Scale Analysis of Methane Emissions with a High-Resolution Inverse Model Using GOSAT and Surface Observations, Remote Sensing, 12, 375, 2020.

Janssens-Maenhout, G., Crippa, M., Guizzardi, D., Muntean, M., Schaaf, E., Dentener, F., Bergamaschi, P., Pagliari, V., Olivier, J. G. J., Peters, J. A. H. W., van Aardenne, J. A., Monni, S., Doering, U., and Petrescu, A. M. R.: EDGAR v4.3.2 Global Atlas of the three major Greenhouse Gas Emissions for the period 1970-2012, Earth Syst. Sci. Data Discuss., 2017, 1-55, 10.5194/essd-2017-79, 2017.

Juncher Jørgensen, C., Lund Johansen, K. M., Westergaard-Nielsen, A., and Elberling, B.: Net regional methane sink in High Arctic soils of northeast Greenland, Nature Geoscience, 8, 20-23, 10.1038/ngeo2305, 2015.

Kirschke, S., Bousquet, P., Ciais, P., Saunois, M., Canadell, J. G., Dlugokencky, E. J., Bergamaschi, P., Bergmann, D., Blake, D. R., Bruhwiler, L., Cameron-Smith, P., Castaldi, S., Chevallier, F., Feng, L., Fraser, A., Heimann, M., Hodson, E. L., Houweling, S., Josse, B., Fraser, P. J., Krummel, P. B., Lamarque, J.-F., Langenfelds, R. L., Le Quéré, C., Naik, V.,

O'Doherty, S., Palmer, P. I., Pison, I., Plummer, D., Poulter, B., Prinn, R. G., Rigby, M., Ringeval, B., Santini, M., Schmidt, M., Shindell, D. T., Simpson, I. J., Spahni, R., Steele, L. P., Strode, S. A., ~~Karion, A., Sweeney, C., Kort, E. A., Shepson, P.~~Sudo, K., Szopa, S., van der Werf, G. R., Voulgarakis, A., van Weele, M., Weiss, R. F., Williams, J. E., and Zeng, G.: Three decades of global methane sources and sinks, Nature Geoscience, 6, 813, 10.1038/ngeo1955, 2013.

~~B., Brewer, A., Cambaliza, M., Conley, S. A., Davis, K., Deng, A., Hardesty, M., Herndon, S. C., Lauvaux, T., Lavoie, T., Lyon, D., Newberger, T., Pétron, G., Rella, C., Smith, M., Wolter, S., Yacovitch, T. I., and Tans, P.: Aircraft-Based Estimate of Total Methane Emissions from the Barnett Shale Region, Environmental Science & Technology, 49, 8124-8131, 10.1021/acs.est.5b00217, 2015.~~

Kivi, R., Heikkinen, P., and Kyr, E.: TCCON data from Sodankyla, Finland, Release GGG2014R0. TCCON data archive, hosted by CaltechDATA, https://doi.org/10.14291/tccon.ggg2014.sodankyla01.R0/1149280, 2017.

Koo, J.-H., Walker, K. A., Jones, A., Sheese, P. E., Boone, C. D., Bernath, P. F., and Manney, G. L.: Global climatology based on the ACE-FTS version 3.5 dataset: Addition of mesospheric levels and carbon-containing species in the UTLS, Journal of Quantitative Spectroscopy and Radiative Transfer, 186, 52-62, 10.1016/j.jqsrt.2016.07.003, 2017.

Kort, E. A., Frankenberg, C., Costigan, K. R., Lindenmaier, R., Dubey, M. K., and Wunch, D.: Four corners: The largest US methane anomaly viewed from space, Geophysical Research Letters, 41, 6898-6903, doi:10.1002/2014GL061503, 2014.

Krol, M., and Lelieveld, J.: Can the variability in tropospheric OH be deduced from measurements of 1,1,1-trichloroethane (methyl chloroform)?, Journal of Geophysical Research: Atmospheres, 108, 4125, 10.1029/2002JD002423, 2003.

Kuze, A., Suto, H., Nakajima, M., and Hamazaki, T.: Thermal and near infrared sensor for carbon observation Fourier-transform spectrometer on the Greenhouse Gases Observing Satellite for greenhouse gases monitoring, Appl. Opt., 48, 6716-6733, 10.1364/AO.48.006716, 2009.

Kuze, A., Suto, H., Shiomi, K., Kawakami, S., Tanaka, M., Ueda, Y., Deguchi, A., Yoshida, J., Yamamoto, Y., Kataoka, F., Taylor, T. E., and Buijs, H. L.: Update on GOSAT TANSO-FTS performance, operations, and data products after more than 6 years in space, Atmos. Meas. Tech., 9, 2445-2461, 10.5194/amt-9-2445-2016, 2016.

Lan, X., Tans, P., Sweeney, C., Andrews, A., Dlugokencky, E., Schwietzke, S., Kofler, J., McKain, K., Thoning, K., Crotwell, M., Montzka, S., Miller, B. R., and Biraud, S. C.: Long-Term Measurements Show Little Evidence for Large Increases in Total U.S. Methane Emissions Over the Past Decade, Geophysical Research Letters, 46, 4991-4999, 10.1029/2018gl081731, 2019.

Lehner, B., and Döll, P.: Development and validation of a global database of lakes, reservoirs and wetlands, Journal of Hydrology, 296, 1-22, https://doi.org/10.1016/j.jhydrol.2004.03.028, 2004.

Liu C., Wang, W., and Sun, Y: TCCON data from Hefei, China, Release GGG2014R0. TCCON data archive, hosted by CaltechDATA, http://dx.doi.org/10.14291/tccon.ggg2014.hefei01.R0, 2018.

Liu, T., Mickley, L. J., Marlier, M. E., DeFries, R. S., Khan, M. F., Latif, M. T., and Karambelas, A.: Diagnosing spatial biases and uncertainties in global fire emissions inventories: Indonesia as regional case study, Remote Sensing of Environment, 237, 111557, https://doi.org/10.1016/j.rse.2019.111557, 2020.

Lu, X., Jacob, D.J., Zhang, Y., Maasakkers, J.D., Shen, L., Qu, Z., Scarpelli, T.R., Nesser, H., Yantosca, R.M., Sheng, J., Andrews, A., Parker, R.J., Boech, H., Bloom, A.A., Ma, S.: Global methane budget and trend, 2010-2017: complementarity of inverse analyses using in situ (GLOBALVIEWplus CH4 ObsPack) and satellite (GOSAT) observations, Atmos. Chem. Phys. Discuss., 2020.

Lunt, M. F., Palmer, P. I., Feng, L., Taylor, C. M., Boesch, H., and Parker, R. J.: An increase in methane emissions from tropical Africa between 2010 and 2016 inferred from satellite data, Atmos. Chem. Phys., 19, 14721-14740, 10.5194/acp-19-14721-2019, 2019.

Maasakkers, J. D., Jacob, D. J., Sulprizio, M. P., Turner, A. J., Weitz, M., Wirth, T., Hight, C., DeFigueiredo, M., Desai, M., Schmeltz, R., Hockstad, L., Bloom, A. A., Bowman, K. W., Jeong, S., and Fischer, M. L.: Gridded National Inventory of U.S. Methane Emissions, Environmental Science & Technology, 50, 13123-13133, 10.1021/acs.est.6b02878, 2016.

Maasakkers, J. D., Jacob, D. J., Sulprizio, M. P., Scarpelli, T. R., Nesser, H., Sheng, J. X., Zhang, Y., Hersher, M., Bloom, A. A., Bowman, K. W., Worden, J. R., Janssens-Maenhout, G., and Parker, R. J.: Global distribution of methane emissions, emission trends, and OH concentrations and trends inferred from an inversion of GOSAT satellite data for 2010–2015, Atmos. Chem. Phys., 19, 7859-7881, 10.5194/acp-19-7859-2019, 2019.

Maasakkers, J. D., Jacob, D. J., Sulprizio, M. P., Scarpelli, T. R., Nesser, H., Sheng, J., Zhang, Y., Lu, X., Bloom, A. A., Bowman, K. W., et al.: 2010 Worden, J. R., and Parker, R. J.: 2010–2015 North American methane emissions, sectoral contributions, and trends: a high-resolution inversion of GOSAT satellite observations of atmospheric methane, Atmos. Chem. Phys2020., Discuss., 2020, 1-28, 10.5194/acp-2020-915, 2020.

de Maziere, M., Sha, M. K., Desmet, F., Hermans, C., Scolas, F., Kumps, N., Metzger, J.-M., Duflot, V., and Cammas, J.-P.: TCCON data from Reunion Island (La Reunion), France, Release GGG2014R0. TCCON data archive, hosted by CaltechDATA, https://doi.org/10.14291/tccon.ggg2014.reunion01.R1, 2017.

Miller, S. M., Miller, C. E., Commane, R., Chang, R. Y.-W., Dinardo, S. J., Henderson, J. M., Karion, A., Lindaas, J., Melton, J. R., Miller, J. B., Sweeney, C., Wofsy, S. C., and Michalak, A. M.: A multiyear estimate of methane fluxes in Alaska from CARVE atmospheric observations, Global Biogeochemical Cycles, 30, 1441-1453, 10.1002/2016gb005419, 2016.

Miller, S. M., Michalak, A. M., Detmers, R. G., Hasekamp, O. P., Bruhwiler, L. M. P., and Schwietzke, S.: China's coal mine methane regulations have not curbed growing emissions, Nature Communications, 10, 303, 10.1038/s41467-018-07891-7, 2019.

Monteil, G., Houweling, S., Butz, A., Guerlet, S., Schepers, D., Hasekamp, O., Frankenberg, C., Scheepmaker, R., Aben, I., and Röckmann, T.: Comparison of CH_4 inversions based on 15 months of GOSAT and SCIAMACHY observations, Journal of Geophysical Research: Atmospheres, 118, 11,807-811,823, 10.1002/2013JD019760, 2013.

Montzka, S. A., Spivakovsky, C. M., Butler, J. H., Elkins, J. W., Lock, L. T., and Mondeel, D. J.: New Observational Constraints for Atmospheric Hydroxyl on Global and Hemispheric Scales, Science, 288, 500-503, 10.1126/science.288.5465.500, 2000.

Morino, I., Yokozeki, N., Matzuzaki, T., and Shishime, A.: TCCON data from Rikubetsu, Hokkaido, Japan, Release GGG2014R2. TCCON data archive, hosted by CaltechDATA, https://doi.org/10.14291/tccon.ggg2014.rikubetsu01.R2, 2017a.

Morino, I., Velazco, V. A., Akihiro, H., Osamu, U., and Griffith, D. W. T.: TCCON data from Burgos, Philippines, Release GGG2014R0. TCCON data archive, hosted by CaltechDATA, http://dx.doi.org/10.14291/tccon.ggg2014.burgos01.R0/1368175, 2017b.

Morino, I., Matsuzaki, T., and Shishime, A.: TCCON data from Tsukuba, Ibaraki, Japan, 125HR, Release GGG2014R2. TCCON data archive, hosted by CaltechDATA, http://doi.org/10.14291/tccon.ggg2014.tsukuba02.R2, 2017c.

Murguia-Flores, F., Arndt, S., Ganesan, A. L., Murray-Tortarolo, G., and Hornibrook, E. R. C.: Soil Methanotrophy Model (MeMo v1.0): a process-based model to quantify global uptake of atmospheric methane by soil, Geosci. Model Dev., 11, 2009-2032, 10.5194/gmd-11-2009-2018, 2018.

Murray, L. T., Jacob, D. J., Logan, J. A., Hudman, R. C., and Koshak, W. J.: Optimized regional and interannual variability of lightning in a global chemical transport model constrained by LIS/OTD satellite data, Journal of Geophysical Research: Atmospheres, 117, 10.1029/2012jd017934, 2012.

Myhre, G., Shindell, D., Bréon, F. M., Collins, W., Fuglestvedt, J., Huang, J., Koch, D., Lamarque, J. F., Lee, D., Mendoza, B., Nakajima, T., Robock, A., Stephens, G., Takemura, T., and Zhang, H.: Anthropogenic and natural radiative forcing, in: Climate Change 2013: The Physical Science Basis. Contribution of Working Group I to the Fifth Assessment Report of the Intergovernmental Panel on Climate Change, edited by: Stocker, T. F., Qin, D., Plattner, G. K., Tignor, M., Allen, S. K., Doschung, J., Nauels, A., Xia, Y., Bex, V., and Midgley, P. M., Cambridge University Press, Cambridge, UK, 659-740, 2013.

Naik, V., Voulgarakis, A., Fiore, A. M., Horowitz, L. W., Lamarque, J. F., Lin, M., Prather, M. J., Young, P. J., Bergmann, D., Cameron-Smith, P. J., Cionni, I., Collins, W. J., Dalsøren, S. B., Doherty, R., Eyring, V., Faluvegi, G., Folberth, G. A., Josse, B., Lee, Y. H., MacKenzie, I. A., Nagashima, T., van Noije, T. P. C., Plummer, D. A., Righi, M., Rumbold, S. T., Skeie, R., Shindell, D. T., Stevenson, D. S., Strode, S., Sudo, K., Szopa, S., and Zeng, G.: Preindustrial to present-day changes in tropospheric hydroxyl radical and methane lifetime from the Atmospheric Chemistry and Climate Model Intercomparison Project (ACCMIP), Atmos. Chem. Phys., 13, 5277-5298, 10.5194/acp-13-5277-2013, 2013.

~~Nepstad, L. S., Gerber, J. S., Hill, J. D., Dias, L. C. P., Costa, M. H., and West, P. C.: Pathways for recent Cerrado soybean expansion: extending the soy moratorium and implementing integrated crop livestock systems with soybeans, Environmental Research Letters, 14, 044029, 10.1088/1748-9326/aafb85, 2019.~~

Nisbet, E. G., Dlugokencky, E. J., Manning, M. R., Lowry, D., Fisher, R. E., France, J. L., Michel, S. E., Miller, J. B., White, J. W. C., Vaughn, B., Bousquet, P., Pyle, J. A., Warwick, N. J., Cain, M., Brownlow, R., Zazzeri, G., Lanoisellé, M., Manning, A. C., Gloor, E., Worthy, D. E. J., Brunke, E. G., Labuschagne, C., Wolff, E. W., and Ganesan, A. L.: Rising atmospheric methane: 2007–2014 growth and isotopic shift, Global Biogeochemical Cycles, 30, 1356-1370, 10.1002/2016GB005406, 2016.

Nisbet, E. G., Manning, M. R., Dlugokencky, E. J., Fisher, R. E., Lowry, D., Michel, S. E., Myhre, C. L., Platt, S. M., Allen, G., Bousquet, P., Brownlow, R., Cain, M., France, J. L., Hermansen, O., Hossaini, R., Jones, A. E., Levin, I., Manning, A. C., Myhre, G., Pyle, J. A., Vaughn, B. H., Warwick, N. J., and White, J. W. C.: Very Strong Atmospheric Methane Growth in the 4 Years 2014–2017: Implications for the Paris Agreement, Global Biogeochemical Cycles, 33, 318-342, 10.1029/2018gb006009, 2019.

Notholt, J., Schrems, O., Warneke, T., Deutscher, N. M., Weinzierl, C., Palm, M., Buschmann, M., and AWI-PEV Station Engineers: TCCON data from Ny Alesund, Spitzbergen, Norway, Release GGG2014R1. TCCON data archive, hosted by CaltechDATA, https://doi.org/10.14291/tccon.ggg2014.nyalesund01.R1, 2019a.

Notholt, J., Petri, C., Warneke, T., Deutscher, N. M., Buschmann, M., Weinzierl, C., Macatangay, R., and Grupe, P.: TCCON data from Bremen, Germany, Release GGG2014R1. TCCON data archive, hosted by CaltechDATA, https://doi.org/10.14291/tccon.ggg2014.bremen01.R1, 2019b.

Pandey, S., Houweling, S., Krol, M., Aben, I., Chevallier, F., Dlugokencky, E. J., Gatti, L. V., Gloor, E., Miller, J. B., Detmers, R., Machida, T., and Röckmann, T.: Inverse modeling of GOSAT-retrieved ratios of total column CH_4 and CO_2 for 2009 and 2010, Atmos. Chem. Phys., 16, 5043-5062, 10.5194/acp-16-5043-2016, 2016.

Pandey, S., Houweling, S., Krol, M., Aben, I., Monteil, G., Nechita-Banda, N., Dlugokencky, E. J., Detmers, R., Hasekamp, O., Xu, X., Riley, W. J., Poulter, B., Zhang, Z., McDonald, K. C., White, J. W. C., Bousquet, P., and Röckmann, T.: Enhanced methane emissions from tropical wetlands during the 2011 La Niña, Scientific Reports, 7, 45759, 10.1038/srep45759, 2017a.

Pandey, S., Houweling, S., Nechita-Banda, N., Krol, M., Röckmann, T., and Aben, I.: What caused the abrupt increase in the methane growth rate during 2014?, EGU General Assembly Conference Abstracts, April 01, 2017, 2017b.

Pandey, S., Houweling, S., Lorente, A., Borsdorff, T., Tsivlidou, M., Bloom, A. A., Poulter, B., Zhang, Z., and Aben, I.: Using satellite data to identify the methane emission controls of South Sudan's wetlands, Biogeosciences Discuss., 2020, 1-31, 10.5194/bg-2020-251, 2020.

Parker, R. J., Boesch, H., Byckling, K., Webb, A. J., Palmer, P. I., Feng, L., Bergamaschi, P., Chevallier, F., Notholt, J., Deutscher, N., Warneke, T., Hase, F., Sussmann, R., Kawakami, S., Kivi, R., Griffith, D. W. T., and Velazco, V.: Assessing 5 years of GOSAT Proxy XCH_4 data and associated uncertainties, Atmos. Meas. Tech., 8, 4785-4801, 10.5194/amt-8-4785-2015, 2015.

Parker, R. J., Webb, A., Boesch, H., Somkuti, P., Barrio Guillo, R., Di Noia, A., Kalaitzi, N., Anand, J. S., Bergamaschi, P., Chevallier, F., Palmer, P. I., Feng, L., Deutscher, N. M., Feist, D. G., Griffith, D. W. T., Hase, F., Kivi, R., Morino, I., Notholt, J., Oh, Y. S., Ohyama, H., Petri, C., Pollard, D. F., Roehl, C., Sha, M. K., Shiomi, K., Strong, K., Sussmann, R., ~~Te~~Té, Y., Velazco, V. A., Warneke, T., Wennberg, P. O., and Wunch, D.: A ~~Decade~~decade of GOSAT Proxy ~~Satellite~~satellite CH4 ~~Observations~~observations, Earth Syst. Sci. Data ~~Discuss., 2020, 1-36~~, 12, 3383-3412, 10.5194/essd-12-3383-2020 ~~114~~, 2020a.

Parker, R. J., Wilson, C., Bloom, A. A., Comyn-Platt, E., Hayman, G., McNorton, J., Boesch, H., and Chipperfield, M. P.: Exploring ~~Constraints~~constraints on a ~~Wetland Methane Emission Ensemble~~wetland methane emission ensemble (WetCHARTs) using GOSAT ~~Satellite Observations~~observations, Biogeosciences ~~Discuss., 2020, 1-33~~, 17, 5669-5691, 10.5194/bg-17-5669-2020~~-284~~, 2020b.

Parker, R.; Boesch, H.: University of Leicester GOSAT Proxy XCH4 v9.0, Centre for Environmental Data Analysis, 07 May 2020, 10.5285/18ef8247f52a4cb6a14013f8235cc1eb, 2020.

Patra, P. K., Houweling, S., Krol, M., Bousquet, P., Belikov, D., Bergmann, D., Bian, H., Cameron-Smith, P., Chipperfield, M. P., Corbin, K., Fortems-Cheiney, A., Fraser, A., Gloor, E., Hess, P., Ito, A., Kawa, S. R., Law, R. M., Loh, Z., Maksyutov, S., Meng, L., Palmer, P. I., Prinn, R. G., Rigby, M., Saito, R., and Wilson, C.: TransCom model simulations of CH_4 and related species: linking transport, surface flux and chemical loss with CH_4 variability in the troposphere and lower stratosphere, Atmos. Chem. Phys., 11, 12813-12837, 10.5194/acp-11-12813-2011, 2011.

Patra, P. K., Krol, M. C., Montzka, S. A., Arnold, T., Atlas, E. L., Lintner, B. R., Stephens, B. B., Xiang, B., Elkins, J. W., Fraser, P. J., Ghosh, A., Hintsa, E. J., Hurst, D. F., Ishijima, K., Krummel, P. B., Miller, B. R., Miyazaki, K., Moore, F. L., Muhle, J., O/'Doherty, S., Prinn, R. G., Steele, L. P., Takigawa, M., Wang, H. J., Weiss, R. F., Wofsy, S. C., and Young, D.: Observational evidence for interhemispheric hydroxyl-radical parity, Nature, 513, 219-223, 10.1038/nature13721, 2014.

Patra, P. K., Saeki, T., Dlugokencky, E. J., Ishijima, K., Umezawa, T., Ito, A., Aoki, S., Morimoto, S., Kort, E. A., Crotwell, A., Ravi Kumar, K., and Nakazawa, T.: Regional Methane Emission Estimation Based on Observed Atmospheric Concentrations (2002-2012), Journal of the Meteorological Society of Japan. Ser. II, 94, 91-113, 10.2151/jmsj.2016-006, 2016.

Peischl, J., Eilerman, S. J., Neuman, J. A., Aikin, K. C., de Gouw, J., Gilman, J. B., Herndon, S. C., Nadkarni, R., Trainer, M., Warneke, C., and Ryerson, T. B.: Quantifying Methane and Ethane Emissions to the Atmosphere From Central and Western U.S. Oil and Natural Gas Production Regions, Journal of Geophysical Research: Atmospheres, 123, 7725-7740, 10.1029/2018jd028622, 2018.

Pickett-Heaps, C. A., Jacob, D. J., Wecht, K. J., Kort, E. A., Wofsy, S. C., Diskin, G. S., Worthy, D. E. J., Kaplan, J. O., Bey, I., and Drevet, J.: Magnitude and seasonality of wetland methane emissions from the Hudson Bay Lowlands (Canada), Atmos. Chem. Phys., 11, 3773-3779, 10.5194/acp-11-3773-2011, 2011.

Prather, M. J., Holmes, C. D., and Hsu, J.: Reactive greenhouse gas scenarios: Systematic exploration of uncertainties and the role of atmospheric chemistry, Geophysical Research Letters, 39, n/a-n/a, 10.1029/2012GL051440, 2012.

Prinn, R. G., Huang, J., Weiss, R. F., Cunnold, D. M., Fraser, P. J., Simmonds, P. G., McCulloch, A., Harth, C., Salameh, P., Doherty, S., Wang, R. H. J., Porter, L., and Miller, B. R.: Evidence for Substantial Variations of Atmospheric Hydroxyl Radicals in the Past Two Decades, Science, 292, 1882, 2001.

Rigby, M., Montzka, S. A., Prinn, R. G., White, J. W. C., Young, D., O'Doherty, S., Lunt, M. F., Ganesan, A. L., Manning, A. J., Simmonds, P. G., Salameh, P. K., Harth, C. M., Mühle, J., Weiss, R. F., Fraser, P. J., Steele, L. P., Krummel, P. B.,

McCulloch, A., and Park, S.: Role of atmospheric oxidation in recent methane growth, Proceedings of the National Academy of Sciences, 114, 5373-5377, 10.1073/pnas.1616426114, 2017.

Rodgers, C. D.: Inverse Methods for Atmospheric Sounding: Theory and Practice, World Scientific, River Edge, NJ, 2000.

Saad, K. M., Wunch, D., Deutscher, N. M., Griffith, D. W. T., Hase, F., De Mazière, M., Notholt, J., Pollard, D. F., Roehl, C. M., Schneider, M., Sussmann, R., Warneke, T., and Wennberg, P. O.: Seasonal variability of stratospheric methane: implications for constraining tropospheric methane budgets using total column observations, Atmos. Chem. Phys., 16, 14003-14024, 10.5194/acp-16-14003-2016, 2016.

Saunois, M., Bousquet, P., Poulter, B., Peregon, A., Ciais, P., Canadell, J. G., Dlugokencky, E. J., Etiope, G., Bastviken, D., Houweling, S., Janssens-Maenhout, G., Tubiello, F. N., Castaldi, S., Jackson, R. B., Alexe, M., Arora, V. K., Beerling, D. J., Bergamaschi, P., Blake, D. R., Brailsford, G., Bruhwiler, L., Crevoisier, C., Crill, P., Covey, K., Frankenberg, C., Gedney, N., Höglund-Isaksson, L., Ishizawa, M., Ito, A., Joos, F., Kim, H. S., Kleinen, T., Krummel, P., Lamarque, J. F., Langenfelds, R., Locatelli, R., Machida, T., Maksyutov, S., Melton, J. R., Morino, I., Naik, V., O'Doherty, S., Parmentier, F. J. W., Patra, P. K., Peng, C., Peng, S., Peters, G. P., Pison, I., Prinn, R., Ramonet, M., Riley, W. J., Saito, M., Santini, M., Schroeder, R., Simpson, I. J., Spahni, R., Takizawa, A., Thornton, B. F., Tian, H., Tohjima, Y., Viovy, N., Voulgarakis, A., Weiss, R., Wilton, D. J., Wiltshire, A., Worthy, D., Wunch, D., Xu, X., Yoshida, Y., Zhang, B., Zhang, Z., and Zhu, Q.: Variability and quasi-decadal changes in the methane budget over the period 2000–2012, Atmos. Chem. Phys., 17, 11135-11161, 10.5194/acp-17-11135-2017, 2017.

Saunois, M., Stavert, A. R., Poulter, B., Bousquet, P., Canadell, J. G., Jackson, R. B., Raymond, P. A., Dlugokencky, E. J., Houweling, S., Patra, P. K., Ciais, P., Arora, V. K., Bastviken, D., Bergamaschi, P., Blake, D. R., Brailsford, G., Bruhwiler, L., Carlson, K. M., Carrol, M., Castaldi, S., Chandra, N., Crevoisier, C., Crill, P. M., Covey, K., Curry, C. L., Etiope, G., Frankenberg, C., Gedney, N., Hegglin, M. I., Höglund-Isaksson, L., Hugelius, G., Ishizawa, M., Ito, A., Janssens-Maenhout, G., Jensen, K. M., Joos, F., Kleinen, T., Krummel, P. B., Langenfelds, R. L., Laruelle, G. G., Liu, L., Machida, T., Maksyutov, S., McDonald, K. C., McNorton, J., Miller, P. A., Melton, J. R., Morino, I., Müller, J., Murguia-Flores, F., Naik, V., Niwa, Y., Noce, S., O'Doherty, S., Parker, R. J., Peng, C., Peng, S., Peters, G. P., Prigent, C., Prinn, R., Ramonet, M., Regnier, P., Riley, W. J., Rosentreter, J. A., Segers, A., Simpson, I. J., Shi, H., Smith, S. J., Steele, L. P., Thornton, B. F., Tian, H., Tohjima, Y., Tubiello, F. N., Tsuruta, A., Viovy, N., Voulgarakis, A., Weber, T. S., van Weele, M., van der Werf, G. R., Weiss, R. F., Worthy, D., Wunch, D., Yin, Y., Yoshida, Y., Zhang, W., Zhang, Z., Zhao, Y., Zheng, B., Zhu, Q., Zhu, Q., and Zhuang, Q.: The Global Methane Budget 2000–2017, Earth Syst. Sci. Data, 12, 1561-1623, 10.5194/essd-12-1561-2020, 2020.

Scarpelli, T. R., Jacob, D. J., Maasakkers, J. D., Sulprizio, M. P., Sheng, J. X., Rose, K., Romeo, L., Worden, J. R., and Janssens-Maenhout, G.: A global gridded (0.1° × 0.1°) inventory of methane emissions from oil, gas, and coal exploitation based on national reports to the United Nations Framework Convention on Climate Change, Earth Syst. Sci. Data, 12, 563-575, 10.5194/essd-12-563-2020, 2020.

Schaefer, H., Fletcher, S. E. M., Veidt, C., Lassey, K. R., Brailsford, G. W., Bromley, T. M., Dlugokencky, E. J., Michel, S. E., Miller, J. B., Levin, I., Lowe, D. C., Martin, R. J., Vaughn, B. H., and White, J. W. C.: A 21st century shift from fossil-fuel to biogenic methane emissions indicated by $^{13}CH_4$, Science, 10.1126/science.aad2705, 2016.

Schneising, O., Buchwitz, M., Reuter, M., Vanselow, S., Bovensmann, H., and Burrows, J. P.: Remote sensing of methane leakage from natural gas and petroleum systems revisited, Atmos. Chem. Phys., 20, 9169-9182, 10.5194/acp-20-9169-2020, 2020.

Schwietzke, S., Pétron, G., Conley, S., Pickering, C., Mielke-Maday, I., Dlugokencky, E. J., Tans, P. P., Vaughn, T., Bell, C., Zimmerle, D., Wolter, S., King, C. W., White, A. B., Coleman, T., Bianco, L., and Schnell, R. C.: Improved Mechanistic Understanding of Natural Gas Methane Emissions from Spatially Resolved Aircraft Measurements, Environmental Science & Technology, 51, 7286-7294, 10.1021/acs.est.7b01810, 2017.

Sheng, J., Song, S., Zhang, Y., Prinn, R. G., and Janssens-Maenhout, G.: Bottom-Up Estimates of Coal Mine Methane Emissions in China: A Gridded Inventory, Emission Factors, and Trends, Environmental Science & Technology Letters, 6, 473-478, 10.1021/acs.estlett.9b00294, 2019.

Sheng, J. X., Jacob, D. J., Turner, A. J., Maasakkers, J. D., Benmergui, J., Bloom, A. A., Arndt, C., Gautam, R., Zavala-Araiza, D., Boesch, H., and Parker, R. J.: 2010–2016 methane trends over Canada, the United States, and Mexico observed by the GOSAT satellite: contributions from different source sectors, Atmos. Chem. Phys., 18, 12257-12267, 10.5194/acp-18-12257-2018, 2018a.

Sheng, J. X., Jacob, D. J., Turner, A. J., Maasakkers, J. D., Sulprizio, M. P., Bloom, A. A., Andrews, A. E., and Wunch, D.: High-resolution inversion of methane emissions in the Southeast US using SEAC4RS aircraft observations of atmospheric methane: anthropogenic and wetland sources, Atmos. Chem. Phys., 18, 6483-6491, 10.5194/acp-18-6483-2018, 2018b.

Sheng, J. X., Jacob, D. J., Maasakkers, J. D., Zhang, Y., and Sulprizio, M. P.: Comparative analysis of low-Earth orbit (TROPOMI) and geostationary (GeoCARB, GEO-CAPE) satellite instruments for constraining methane emissions on fine regional scales: application to the Southeast US, Atmos. Meas. Tech., 11, 6379-6388, 10.5194/amt-11-6379-2018, 2018c.

Sherlock, V., Connor, B. J., Robinson, J., Shiona, H., Smale, D., and Pollard, D.: TCCON data from Lauder, New Zealand, 120HR, Release GGG2014R0. TCCON data archive, hosted by CaltechDATA, https://doi.org/10.14291/tccon.ggg2014.lauder01.R0/1149293, 2017a.

Sherlock, V., Connor, B. J., Robinson, J., Shiona, H., Smale, D., and Pollard, D.: TCCON data from Lauder, New Zealand, 125HR, Release GGG2014R0. TCCON data archive, hosted by CaltechDATA, https://doi.org/10.14291/tccon.ggg2014.lauder02.R0/1149298, 2017b.

Sherwen, T., Schmidt, J. A., Evans, M. J., Carpenter, L. J., Großmann, K., Eastham, S. D., Jacob, D. J., Dix, B., Koenig, T. K., Sinreich, R., Ortega, I., Volkamer, R., Saiz-Lopez, A., Prados-Roman, C., Mahajan, A. S., and Ordóñez, C.: Global impacts of tropospheric halogens (Cl, Br, I) on oxidants and composition in GEOS-Chem, Atmos. Chem. Phys., 16, 12239-12271, 10.5194/acp-16-12239-2016, 2016.

Shiomi, K., Kawakami, S., Ohyama, H., Arai, K., Okumura, H., Taura, C., Fukamachi, T., and Sakashita, M.: TCCON data from Saga, Japan, Release GGG2014R0. TCCON data archive, hosted by CaltechDATA, https://doi.org/10.14291/tccon.ggg2014.saga01.R0/1149283, 2017.

Smith, M. L., Gvakharia, A., Kort, E. A., Sweeney, C., Conley, S. A., Faloona, I., Newberger, T., Schnell, R., Schwietzke, S., and Wolter, S.: Airborne Quantification of Methane Emissions over the Four Corners Region, Environmental Science & Technology, 51, 5832-5837, 10.1021/acs.est.6b06107, 2017.

Stanevich, I., Jones, D. B. A., Strong, K., Parker, R. J., Boesch, H., Wunch, D., Notholt, J., Petri, C., Warneke, T., Sussmann, R., Schneider, M., Hase, F., Kivi, R., Deutscher, N. M., Velazco, V. A., Walker, K. A., and Deng, F.: Characterizing model errors in chemical transport modeling of methane: ~~Impact~~impact of model resolution in versions v9-02 of GEOS-Chem and v35j of its adjoint model, Geosci. Model Dev~~. Discuss., 2019, 1-42~~., 13, 3839-3862, 10.5194/gmd-~~2019-248, 2019~~13-3839-2020, 2020.

Strahan, S. E., Duncan, B. N., and Hoor, P.: Observationally derived transport diagnostics for the lowermost stratosphere and their application to the GMI chemistry and transport model, Atmos. Chem. Phys., 7, 2435-2445, 10.5194/acp-7-2435-2007, 2007.

Strong, K., Roche, S., Franklin, J.E., Mendonca, J., Lutsch, E., Weaver, D., Fogal, P.F., Drummond, J.R., Batchelor, R., and Lindenmaier, R.: TCCON data from Eureka, Canada, Release GGG2014R3. TCCON data archive, hosted by CaltechDATA, http://doi.org/10.14291/tccon.ggg2014.eureka01.R3, 2017.

Sussmann, R., and Rettinger, M.: TCCON data from Garmisch, Germany, Release GGG2014R2. TCCON data archive, hosted by CaltechDATA, https://doi.org/10.14291/tccon.ggg2014.garmisch01.R2, 2017.

Te, Y., Jeseck, P., and Janssen, C.: TCCON data from Paris, France, Release GGG2014R0. TCCON data archive, hosted by CaltechDATA, https://doi.org/10.14291/tccon.ggg2014.paris01.R0/1149279, 2017.

Thompson, R. L., Stohl, A., Zhou, L. X., Dlugokencky, E., Fukuyama, Y., Tohjima, Y., Kim, S.-Y., Lee, H., Nisbet, E. G., Fisher, R. E., Lowry, D., Weiss, R. F., Prinn, R. G., O'Doherty, S., Young, D., and White, J. W. C.: Methane emissions in East Asia for 2000–2011 estimated using an atmospheric Bayesian inversion, Journal of Geophysical Research: Atmospheres, 120, 4352-4369, 10.1002/2014jd022394, 2015.

Tunnicliffe, R. L., Ganesan, A. L., Parker, R. J., Boesch, H., Gedney, N., Poulter, B., Zhang, Z., Lavrič, J. V., Walter, D., Rigby, M., Henne, S., Young, D., and O'Doherty, S.: Quantifying sources of Brazil's CH_4 emissions between 2010 and 2018 from satellite data, Atmos. Chem. Phys~~. Discuss., 2020, 1-40~~., 20, 13041-13067, 10.5194/acp-20-13041-2020~~-438~~, 2020.

Turner, A. J., Jacob, D. J., Wecht, K. J., Maasakkers, J. D., Lundgren, E., Andrews, A. E., Biraud, S. C., Boesch, H., Bowman, K. W., Deutscher, N. M., Dubey, M. K., Griffith, D. W. T., Hase, F., Kuze, A., Notholt, J., Ohyama, H., Parker, R., Payne, V. H., Sussmann, R., Sweeney, C., Velazco, V. A., Warneke, T., Wennberg, P. O., and Wunch, D.: Estimating global and North American methane emissions with high spatial resolution using GOSAT satellite data, Atmos. Chem. Phys., 15, 7049-7069, 10.5194/acp-15-7049-2015, 2015.

Turner, A. J., Frankenberg, C., Wennberg, P. O., and Jacob, D. J.: Ambiguity in the causes for decadal trends in atmospheric methane and hydroxyl, Proceedings of the National Academy of Sciences, 114, 5367-5372, 10.1073/pnas.1616020114, 2017.

van der Werf, G. R., Randerson, J. T., Giglio, L., van Leeuwen, T. T., Chen, Y., Rogers, B. M., Mu, M., van Marle, M. J. E., Morton, D. C., Collatz, G. J., Yokelson, R. J., and Kasibhatla, P. S.: Global fire emissions estimates during 1997–2016, Earth Syst. Sci. Data, 9, 697-720, 10.5194/essd-9-697-2017, 2017.

Varon, D. J., McKeever, J., Jervis, D., Maasakkers, J. D., Pandey, S., Houweling, S., Aben, I., Scarpelli, T., and Jacob, D. J.: Satellite Discovery of Anomalously Large Methane Point Sources From Oil/Gas Production, Geophysical Research Letters, 46, 13507-13516, 10.1029/2019gl083798, 2019.

Wang, Z., Warneke, T., Deutscher, N. M., Notholt, J., Karstens, U., Saunois, M., Schneider, M., Sussmann, R., Sembhi, H., Griffith, D. W. T., Pollard, D. F., Kivi, R., Petri, C., Velazco, V. A., Ramonet, M., and Chen, H.: Contributions of the troposphere and stratosphere to CH4 model biases, Atmos. Chem. Phys., 17, 13283-13295, 10.5194/acp-17-13283-2017, 2017.

Wang, F., Maksyutov, S., Tsuruta, A., Janardanan, R., Ito, A., Sasakawa, M., Machida, T., Morino, I., Yoshida, Y., Kaiser, J. W., Janssens-Maenhout, G., Dlugokencky, E. J., Mammarella, I., Lavric, J. V., and Matsunaga, T.: Methane Emission Estimates by the Global High-Resolution Inverse Model Using National Inventories, Remote Sensing, 11, 2489, 2019a.

Wang, X., Jacob, D. J., Eastham, S. D., Sulprizio, M. P., Zhu, L., Chen, Q., Alexander, B., Sherwen, T., Evans, M. J., Lee, B. H., Haskins, J. D., Lopez-Hilfiker, F. D., Thornton, J. A., Huey, G. L., and Liao, H.: The role of chlorine in global tropospheric chemistry, Atmos. Chem. Phys., 19, 3981-4003, 10.5194/acp-19-3981-2019, 2019b.

Warneke, T., Messerschmidt, J., Notholt, J., Weinzierl, C., Deutscher, N. M., Petri, C., Grupe, P., Vuillemin, C., Truong, F., Schmidt, M., Ramonet, M., and Parmentier, E.: TCCON data from Orleans, France, Release GGG2014R1. TCCON data archive, hosted by CaltechDATA, https://doi.org/10.14291/tccon.ggg2014.orleans01.R1, 2017.

Waymark, C., Walker, K., Boone, C. D., and Bernath, P. F.: ACE-FTS version 3.0 data set: validation and data processing update, 2014, 56, 10.4401/ag-6339, 2014.

Webb, A. J., Bösch, H., Parker, R. J., Gatti, L. V., Gloor, E., Palmer, P. I., Basso, L. S., Chipperfield, M. P., Correia, C. S. C., Domingues, L. G., Feng, L., Gonzi, S., Miller, J. B., Warneke, T., and Wilson, C.: CH4 concentrations over the Amazon from GOSAT consistent with in situ vertical profile data, Journal of Geophysical Research: Atmospheres, 121, 11,006-011,020, https://doi.org/10.1002/2016JD025263, 2016.

Wecht, K. J., Jacob, D. J., Frankenberg, C., Jiang, Z., and Blake, D. R.: Mapping of North American methane emissions with high spatial resolution by inversion of SCIAMACHY satellite data, Journal of Geophysical Research: Atmospheres, 119, 7741-7756, 10.1002/2014JD021551, 2014.

Wennberg, P. O., Wunch, D., Roehl, C., Blavier, J. F., Toon, G. C., and Allen, N.: TCCON data from California Institute of Technology, Pasadena, California, USA, Release GGG2014R1. TCCON data archive, hosted by CaltechDATA, https://doi.org/10.14291/tccon.ggg2014.pasadena01.R1/1182415, 2017a.

Wennberg, P. O., Roehl, C., Blavier, J. F., Wunch, D., Landeros, J., and Allen, N.: TCCON data from Jet Propulsion Laboratory, Pasadena, California, USA, Release GGG2014R1. TCCON data archive, hosted by CaltechDATA, https://doi.org/10.14291/tccon.ggg2014.jpl02.R1/1330096, 2017b.

Wennberg, P. O., Wunch, D., Roehl, C., Blavier, J. F., Toon, G. C., Allen, N., Dowell, P., Teske, K., Martin, C., and Martin, J.: TCCON data from Lamont, Oklahoma, USA, Release GGG2014R1. TCCON data archive, hosted by CaltechDATA, https://doi.org/10.14291/tccon.ggg2014.lamont01.R1/1255070, 2017c.

Wennberg, P. O., Roehl, C., Wunch, D., Toon, G. C., Blavier, J. F., Washenfelder, R. a., Keppel-Aleks, G., Allen, N., and Ayers, J.: TCCON data from Park Falls, Wisconsin, USA, Release GGG2014R1. TCCON data archive, hosted by CaltechDATA, http://doi.org/10.14291/tccon.ggg2014.parkfalls01.R1, 2017d.

Worden, J. R., Bloom, A. A., Pandey, S., Jiang, Z., Worden, H. M., Walker, T. W., Houweling, S., and Röckmann, T.: Reduced biomass burning emissions reconcile conflicting estimates of the post-2006 atmospheric methane budget, Nature Communications, 8, 2227, 10.1038/s41467-017-02246-0, 2017.

Wunch, D., Toon, G. C., Blavier, J.-F. L., Washenfelder, R. A., Notholt, J., Connor, B. J., Griffith, D. W. T., Sherlock, V., and Wennberg, P. O.: The Total Carbon Column Observing Network, Philosophical Transactions of the Royal Society A: Mathematical, Physical and Engineering Sciences, 369, 2087-2112, doi:10.1098/rsta.2010.0240, 2011.

Wunch, D., Mendonca, J., Colebatch, O., Allen, N., Blavier, J.-F. L., Roche, S., Hedelius, J. K., Neufeld, G., Springett, S., Worthy, D. E. J., Kessler, R., and Strong, K.: TCCON data from East Trout Lake, Canada, Release GGG2014R1. TCCON data archive, hosted by CaltechDATA, https://doi.org/10.14291/tccon.ggg2014.easttroutlake01.R1, 2017.

Yin, Y., Chevallier, F., Ciais, P., Bousquet, P., Saunois, M., Zheng, B., Worden, J., Bloom, A. A., Parker, R., Jacob, D., Dlugokencky, E. J., and Frankenberg, C.: Accelerating methane growth rate from 2010 to 2017: leading contributions from the tropics and East Asia, Atmos. Chem. Phys. Discuss., 2020, 1-27, 10.5194/acp-2020-649, 2020.

Zhang, B., Tian, H., Ren, W., Tao, B., Lu, C., Yang, J., Banger, K., and Pan, S.: Methane emissions from global rice fields: Magnitude, spatiotemporal patterns, and environmental controls, Global Biogeochemical Cycles, 30, 1246-1263, 10.1002/2016gb005381, 2016.

Zhang, Y., Jacob, D. J., Maasakkers, J. D., Sulprizio, M. P., Sheng, J. X., Gautam, R., and Worden, J.: Monitoring global tropospheric OH concentrations using satellite observations of atmospheric methane, Atmos. Chem. Phys., 18, 15959-15973, 10.5194/acp-18-15959-2018, 2018.

Zhang, Y., Gautam, R., Pandey, S., Omara, M., Maasakkers, J. D., Sadavarte, P., Lyon, D., Nesser, H., Sulprizio, M. P., Varon, D. J., Zhang, R., Houweling, S., Zavala-Araiza, D., Alvarez, R. A., Lorente, A., Hamburg, S. P., Aben, I., and Jacob, D. J.: Quantifying methane emissions from the largest oil-producing basin in the United States from space, Science Advances, 6, eaaz5120, 10.1126/sciadv.aaz5120, 2020.

Zona, D., Gioli, B., Commane, R., Lindaas, J., Wofsy, S. C., Miller, C. E., Dinardo, S. J., Dengel, S., Sweeney, C., Karion, A., Chang, R. Y.-W., Henderson, J. M., Murphy, P. C., Goodrich, J. P., Moreaux, V., Liljedahl, A., Watts, J. D., Kimball, J.

S., Lipson, D. A., and Oechel, W. C.: Cold season emissions dominate the Arctic tundra methane budget, Proceedings of the National Academy of Sciences, 201516017, 10.1073/pnas.1516017113, 2015.